UNIVERSITY OF SOUTHAMPTON

Faculty of Engineering and Physical Sciences
Optoelectronics Research Centre

Computational Modelling of High Harmonic Generation in Gas-Filled Hollow Capillaries

by

Samuel Martin Senior
MPhys

A thesis for the degree of
Doctor of Philosophy

June 2022

University of Southampton

Abstract

Faculty of Engineering and Physical Sciences
Optoelectronics Research Centre

Doctor of Philosophy

Computational Modelling of High Harmonic Generation in Gas-Filled Hollow Capillaries

by Samuel Martin Senior

High harmonic generation uses ultrashort intense laser pulses to generate extreme ultraviolet and soft x-ray radiation. This provides a table-top source of this radiation with uses within imaging and spectroscopy that is an alternative to large and costly facilities. This process is highly complex and difficult to simulate in detail. Here, for the first time, we developed a full, three-dimensional, a priori computer model that runs on a high performance computing cluster and describes all aspects of the physics involved: the ultrashort nonlinear laser pulse propagation, the medium response including ionisation and high harmonic generation, and the propagation of these high harmonics. This model was then validated against experimental and simulation results from the literature.

This model was then used to investigate two experimentally important questions. The first being which pump laser wavelength should be used, and the second being which state of the art short-pulse laser system should be used, where powers, pulse lengths, wavelengths, and repetition rates are varied. On the wavelength question, we investigated three different geometries, a single atom, a sheet of atoms, and a gas-filled hollow capillary. When accounting for full three-dimensional effects of quantum diffusion we found the harmonic generation for the single atom to scale with wavelength as λ^{-5} and for the sheet of atoms and capillary we found it to scale as λ^{-6} instead. For the choice of laser system, we investigated six different systems, testing capillary lengths of up to 7 cm. We found laser pulse mode beating, capillary length, and capillary gas pressure profile to all greatly affect the harmonic generation, with reductions in capillary length from 7 cm significantly increasing the resulting high harmonic generation.

Contents

List of Figures

List of Tables

Declaration of Authorship

I declare that this thesis and the work presented in it is my own and has been generated by me as the result of my own original research.

I confirm that:

1. This work was done wholly or mainly while in candidature for a research degree at this University;
2. Where any part of this thesis has previously been submitted for a degree or any other qualification at this University or any other institution, this has been clearly stated;
3. Where I have consulted the published work of others, this is always clearly attributed;
4. Where I have quoted from the work of others, the source is always given. With the exception of such quotations, this thesis is entirely my own work;
5. I have acknowledged all main sources of help;
6. Where the thesis is based on work done by myself jointly with others, I have made clear exactly what was done by others and what I have contributed myself;
7. None of this work has been published before submission

Signed:..... Date:.....

Acknowledgements

I would like to acknowledge Peter Horak and William Brocklesby for their excellent supervision, support, and encouragement throughout all the years of this PhD.

Additionally, I would like to express my gratitude to all those involved in the EPSRC Centre for Doctoral Training in Next Generation Computational Modelling for their invaluable training in various computational modelling techniques.

Finally, I would like to thank my family and my friends for their much-appreciated encouragement and support throughout.

Definitions and Abbreviations

1D	One-Dimensional
3D	Three-Dimensional
ASM	Anuglar Spectrum Method
CFD	Computational Fluid Dynamics
CPA	Chirped Pulse Amplification
CPU	Central Processing Unit
CXDI	Coherent X-Ray Diffractive Imaging
FEL	Free Electron Laser
FWHM	Full Width Half Maximum
GCC	GNU Compiler Collection
GNU	GNU's Not Unix
HHG	High Harmonic Generation
HPC	High Performance Cluster
IR	Infrared
MKL	Maths Kernal Library
MPI	Message Passing Interface
OO	Object Orientation
RKF	Runge-Kutta-Fehlberg
RR	Repetition Rate
SAE	Single Active Electron
SXR	Soft X-Ray
TDSE	Time Dependent Scrödinger Equation
UPPE	Unidirectional Pulse Propagation Equation
UV	Ultraviolet
XUV	Extreme Ultraviolet

Chapter 1

Introduction

1.1 High Harmonic Generation

High harmonic generation (HHG) is a nonlinear optical process in which a high intensity laser pulse interacts with a medium such as solid, liquid, gas, or plasma. In this interaction, extreme ultraviolet, XUV, (10 nm - 120 nm) and soft x-ray, SXR, (0.1 nm - 10 nm) radiation is generated. This generated radiation has applications in many scientific disciplines, such as in spectroscopy or microscopy imaging via techniques including coherent x-ray diffractive imaging [76, 95].

There are a number of methods that can be used to generate electromagnetic radiation within the XUV and SXR regimes, such as free electron lasers (FELs), synchrotrons, and tabletop HHG sources that use ultrafast lasers and either gas cells, jets, or capillaries. All these methods present their own advantages and disadvantages. For instance, the European XFEL is a new free electron facility that was inaugurated in September 2017 [8]. This facility can produce coherent x-ray beams of wavelengths $0.05 - 4.7$ nm, with peak brilliances a billion times higher than the best conventional sources, such as x-ray tubes, and average brilliances $10,000$ times higher than the best conventional sources [7]. For such a specification, this is a costly multi-national project, with the construction costs of 1.22 billion euros and an annual budget of 122 million euros [7]. Additionally, the Diamond Light Source is the UK's national synchrotron facility. As a 3 GeV, medium sized synchrotron, which was first opened in October 2007, Diamond can produce x-ray beams $10,000$ times brighter than its predecessor, 100 billion times brighter than a standard hospital machine, and 10 billion times brighter than the sun [4, 3]. This again is a costly facility, with the first two stages of development costing a total of £383 million and with the third stage expected to cost £111.2 million. Alongside this operational costs are also high, with its first year totalling £23 million, which then increased to £40 million for the year 2012/13, and with running costs expected to increase further as more beamlines become operational [3]. Both of these types of

x-ray and XUV sources are also multi-user and so time has to be booked on them in advance. High harmonic generation tabletop setups, on the other hand, are far smaller in size and considerably less expensive, costing around £3 million, and also being able to generate both coherent XUV and SXR radiation. As such, individual research groups can afford to house their own tabletop sources, allowing them to be a single-user HHG source that can be tailored specifically to the needs of that research group. Extreme ultraviolet radiation generated through HHG tabletop techniques has even been shown to have fluxes comparable to spatially filtered synchrotron light [24], demonstrating that it is a viable alternative to both synchrotrons and FELs.

High harmonic generation in rare gases was first observed by McPherson et al. in 1987 using ultraviolet driving laser pulses [74] and was then later observed by Ferray et al. in 1988 using mid-infrared driving laser pulses [39]. This in itself was only made possible by the development of the laser by Maiman in 1960 [71] and the development of lasers able to reach intensities greater than 10^{13} Wcm^{-2}, such as the chirped pulse amplification (CPA) scheme developed by Strickland and Mourou in 1985 [110]. The CPA has proved such an important development in its ability to provide high-intensity, ultra-short pulses that it earned Strickland and Mourou the 2018 Nobel Prize in Physics, joint with Ashkin for his work in inventing optical tweezers [6].

Before the discovery of high harmonic generation, lasers had been used to demonstrate other nonlinear optical effects. The first such effect was second harmonic generation, demonstrated by Franken et al. in 1961 [40], who used a ruby laser to produce ultraviolet second harmonic radiation at an efficiency of around 10^{-8}. This efficiency was quickly surpassed by Giordmaine, and Maker et al. in 1962 [50, 72]. Since then, other nonlinear effects have been observed, such as sum and difference frequency generation [20, 18, 52], spontaneous parametric down-conversion [64, 23], stimulated Raman scattering [87], and self focusing [30], amongst others [22].

Prior to the invention of the laser and the discovery of nonlinear optical effects, the main focus in optics was that of linear optics. In this, an electric field passing through a material causes the electrons of that material to oscillate. These oscillations then produce a new electric field that is linearly dependent on the incident field. This in turn causes a linear response, which is seen as the refractive index and the absorption of that material.

This response is due to the electrons being bound to nuclei of the atoms in that material, which can be modelled as a harmonic potential.

Starting with a Taylor expansion of the potential, given as

$$V(x) = V(0) + x\frac{d}{dx}V(0) + \frac{x^2}{2!}\frac{d^2}{dx^2}V(0) + \frac{x^3}{3!}\frac{d^3}{dx^3}V(0) + ..., \tag{1.1}$$

and defining $x = 0$ to be the position at which the potential is at a minimum of zero, both $V(0)$ and $\frac{dV(0)}{dx}$ are equal to zero and so the potential of the system can be approximated as

$$V(x) \approx \frac{x^2}{2}\frac{d^2}{dx^2}V(0). \tag{1.2}$$

This is also provided that the electric field causing the electron oscillations is sufficiently small so as to enable the terms past the second order derivative to be discarded due to them being negligible.

The restoring force of this system is then

$$F = -\frac{d}{dx}V = -x\frac{d^2}{dx^2}V(0), \tag{1.3}$$

leading to the result that the displacement of the electron, known as the polarisation, is

$$P = \varepsilon_0 \chi E, \tag{1.4}$$

where P is the polarisation of the material, ε_0 is the permittivity of free space, χ is the medium susceptibility, and E is the electric field.

It is then seen that for the case of a driving field $E = \frac{1}{2}|E_0|e^{i\omega t} + c.c$ where $c.c.$ is the complex conjugate, the electron oscillates at the frequency ω and therefore generates a new field at that frequency, showing that for weak fields there is only a linear response.

For larger driving electric fields, but still substantially below the atomic field strength, the electrons oscillate over larger distances anharmonically. The higher order terms of the potential can no longer be ignored, leading to the result that the polarisation is no longer linearly related to the driving field. Instead, the polarisation is now related to the electric field by [22]

$$P = \varepsilon_0 \left(\chi^{(1)}E + \chi^{(2)}E^2 + \chi^{(3)}E^3 + ...\right), \tag{1.5}$$

where $\chi^{(2)}$ and $\chi^{(3)}$, etc, are higher order nonlinear susceptibilities.

For processes such as second harmonic generation and sum frequency generation the second order nonlinearity is non-zero, and therefore is the cause of these effects. This can be seen by having a driving field comprised of two electric fields, each of a different frequency, $E = \frac{1}{2}|E_1|e^{i\omega_1 t} + \frac{1}{2}|E_2|e^{i\omega_2 t} + c.c.$. Substituting this driving field into the second order term of the polarisation gives a resulting field that contains a number of combinations of these two fields, due to the second order term being quadratic. One such component of this resulting field has twice the frequency of one of the driving fields (second harmonic generation), and another component has a frequency of the combined frequencies of the two driving fields (sum frequency generation). As such, these two effects, being due to the second order term, are nonlinear effects of optics.

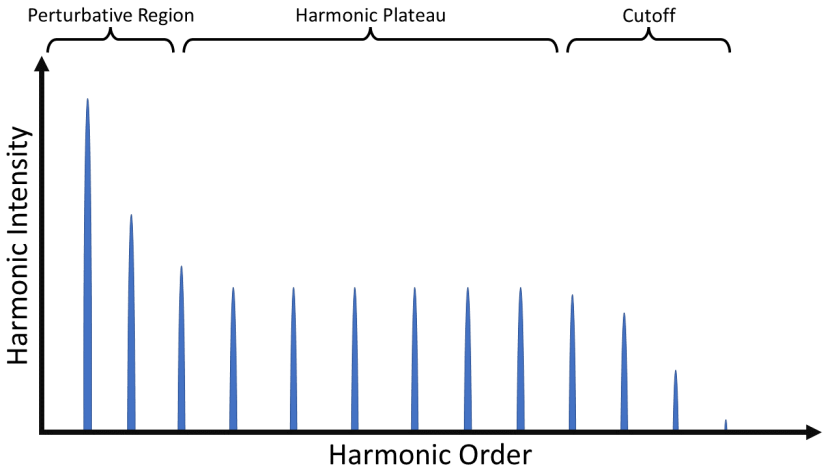

FIGURE 1.1: Example of a typical high harmonic spectrum.

Expanding this quadratic term alone gives rise to 16 terms, 10 of which are unique. Therefore, still higher order non-zero susceptibilities give rise to vast sums of unique terms and a whole range of possible generated wavelengths.

For high harmonic generation, the driving field is so strong that the electron is no longer confined to small oscillations around the nucleus of its parent atom and instead it becomes an ionised free electron in the process of its oscillations, before recombining and producing a high energy photon. Hence perturbative theory does not describe this process and so is inappropriate. For high harmonic generation, a full quantum description of the motion of the sometimes-free electron must be considered to accurately model the process and the resulting generated high harmonics.

Spectra resulting from high harmonic generation, the theory of which is discussed in detail later in Chapter 2, share common features [15]. A typical high harmonic spectrum is given in Figure 1.1. As shown, at the lowest harmonic orders there is a perturbative region, followed by a harmonic plateau, and finally a cutoff. For the perturbative region the electron behaves perturbatively and so the resulting generated low order harmonics quickly decrease in their intensity. The harmonic plateau is a region in which the intensities of the harmonics generated remain relatively constant over that region, and finally the cutoff is where the harmonic intensities rapidly decrease and past it harmonic generation ceases.

When considering systems for HHG that involve multiple atoms, an important effect is that of phase-matching. In phase-matching multiple sources of harmonic radiation can combine together efficiently such that they interfere and build-up coherently, leading to significant increases in the resulting harmonic intensity. This is provided that a fixed phase relationship is maintained between the driving laser field and the harmonic field along the propagation direction. If this fixed phase relationship is either

not present or not maintained then the resulting harmonic intensity can instead be significantly degraded due to destructive interference between the harmonics generated by the different sources.

Phase-matching is achieved when the mismatch between the wave vector of a given harmonic and the driving laser is zero. This is expressed as [26]

$$\Delta k = k_q - qk_l, \tag{1.6}$$

where Δk is the phase mismatch, k_q is the wavevector of the qth harmonic,and k_l is the wave vector of the driving laser.

Perfect phase-matching is rare to achieve, with the phase mismatch typically causing oscillations in the harmonic intensity. The length at which the two fields shift from interfering constructively to destructively is known as the coherence length [26] and occurs when the phase shift between the two fields is π radians. This is given as

$$L_c = \frac{\pi}{\Delta k}. \tag{1.7}$$

Knowledge of the coherence length for a particular system and set up can be used to improve the resulting intensity of the generated harmonics. For example, if the interaction length of a generation medium can be chosen to be either the coherence length or less, then the harmonics generated within it will build up coherently and the result will be a larger harmonic intensity.

Eq. (1.6) relates phase-matching to chromatic dispersion. Within HHG experiments different geometries can be used, with each having its own properties that affect the dispersion and the phase-matching. Common geometries include gas jets, gas cells, and gas-filled hollow capillaries.

The gas-filled hollow capillary allows for much longer interaction lengths than gas jets and cells, and due to properties that can be used to affect the dispersion within them, they can be used to achieve improved phase-matching and efficient build-up of harmonics over much longer interaction lengths than is possible with gas jets or cells. To demonstrate this, the propagation constant for the laser travelling in the lowest mode of the gas-filled hollow capillary is given by [94]

$$k \approx \frac{2\pi}{\lambda} + \frac{2\pi N_a \delta(\lambda)}{\lambda} - N_e r_e \lambda - \frac{u_{11}^2 \lambda}{4\pi a^2}, \tag{1.8}$$

where λ is the wavelength, N_a is the atom density, N_e the electron density, r_e the classical electron radius, u_{11} the first root of the zero order Bessel function, a the radius of the hollow capillary, and δ being related to the refractive index of the gas by $\delta = \mathbb{R}(n) - 1$. Here the first term corresponds to the contributions from the vacuum propagation, the

second term the contributions from the neutral gas dispersion, the third term the contributions from the dispersion of the ionisation-induced plasma, and the final term the contributions from the waveguide dispersion. The nonlinear refractive index of the gas has also been neglected here as it is small compared to the other terms [57].

From this, the phase mismatch between the driving laser and a given harmonic is [57]

$$\Delta k \approx q\frac{u_{11}^2\lambda_0}{4\pi a^2} + N_e r_e(q\lambda_0 - \lambda_q) - q\frac{2\pi N_a(\delta(\lambda_0) - \delta(\lambda_q))}{\lambda_q}. \tag{1.9}$$

The first term here corresponds to the capillary dispersion, the second term the plasma dispersion, and the third term the neutral gas dispersion.

For the harmonic radiation, the phase velocity is slightly greater than the speed of light due to the interactions of the harmonic radiation and the capillary being minimal while the phase velocity of the laser depends on the waveguide, plasma, and neutral gas dispersion. Here the first two dispersion terms increase the phase velocity whilst the last decreases it, due to the differences in their signs. The phase velocity of the laser can therefore be controlled through changing these. This can be done, for instance, by changing the gas pressure within the capillary or the laser intensity. This is since the number of neutral atoms and number of free electrons both depend on the gas pressure as well as the ionisation fraction, which is dictated by the laser intensity. The result of this is that with the decreased phase mismatch the coherence length is increased, allowing for longer interaction lengths within gas-filled hollow capillaries. Therefore, the controllable phase mismatch between a given harmonic and the driving laser allows the capillary to potentially have much more significant coherent build-up of generated harmonics compared to the two other geometries mentioned.

1.2 Applications of High Harmonic Generation

As mentioned, extreme ultraviolet and soft x-ray radiation generated from HHG processes is useful for many different applications, including in spectroscopy and microscopy imaging techniques. For example, within spectroscopy x-rays can be used to probe molecules and atoms to gain insights into their electronic structure [10, 32] and high harmonic generation can provide the x-rays that are used for this.

In microscopy there is a lower limit to the possible attainable resolution, this is known as the diffraction limit [9, 21] and due to this two objects cannot be distinguished and imaged as separate objects if they are separated by less than half the wavelength of the light being used to image them. By using light of shorter wavelengths it is possible to image smaller objects, and so by using light within the XUV or SXR regimes objects on the nanometer scale can be imaged.

Within the work present here, the tabletop HHG process modelled is that of a hollow capillary filled with a rare gas, as first demonstrated by Rundquist et al in 1998 [94]. This hollow capillary has an intense laser pulse propagating through it along its optical axis which interacts with the gas present to produce high harmonics. Other similar set ups include the use of gas jets and gas cells rather than a hollow capillary [68, 102].

The Ultrafast X-ray Group of the Southampton University Optoelectronics Research Centre use extreme ultraviolet and soft x-ray radiation for imaging, through a technique know as coherent x-ray diffractive imaging (CXDI) [75, 77, 78, 95], which can be used for imaging in biological and physical applications.

In CXDI a sample is illuminated with a coherent extreme ultraviolet or soft x-ray beam. The diffraction pattern due to this illumination is then collected and from it an image of the sample is reconstructed using an iterative algorithm. This technique has advantages over the more traditional x-ray microscopes, such as tuning of the beam wavelength being used to give high contrast images of the sample, as well as the lack of need for imaging optics. For the experimental set up using this technique, typically there is a high-power ultrafast laser, either a gas cell, jet, or capillary, the sample, and the detector. Currently, the Ultrafast X-ray Group use a gas cell, though previously a gas-filled hollow capillary has been used with much success [24, 43, 86, 107, 93].

A gas-filled hollow capillary has the advantage over a gas cell of longer interaction lengths, and also the potential for better coherent build up [93]. The gas cell, on the other hand, has the advantage of shorter distances in the gas for the laser pulse to propagate through, thus meaning the laser pulse will be less distorted by its interaction with the gas, allowing for better understood laser pulses to drive the high harmonic generation.

Improving the flux and coherence of the XUV and SXR source in CDXI experiments improves the quality of the image. In terms of the flux, this increases the number of photons that are present illuminating the sample, and thus means more detail can be captured. In terms of coherence, if more of the radiation being used is coherent then the diffraction patterns produced become clearer and so better quality images can be reconstructed from them. Previous improvements to HHG have included using different length hollow capillaries [24], structured laser beams [54], laser beams of different waists [119], different gas pressures within the generation geometry [24], and two-colour driving pulses [47].

1.3 Motivations

The motivation of this work is to test and investigate parameters to improve the flux and coherence of XUV and SXR radiation generated within gas-filled hollow capillaries.

This will then allow for optimisations of the generation of high harmonics as well as give a better understanding of the mechanisms involved. This is to be done through use of a bespoke computer simulation code developed specifically for this task.

Computational simulations can prove extremely useful as they can test parameters that would be hard to test experimentally or require changes to the experimental set up. Simulations can also observe and investigate regions of interest that cannot be observed or investigated easily experimentally, such as regions of HHG inside the capillary itself. Also, they can produce detailed results in a faster time than the experiment may be able to do so, depending on the exact set ups being used.

The computer simulation used and developed in this PhD project has three key parts. The first is its ability to accurately propagate a laser pulse through a gas-filled hollow capillary. The second is its ability to calculate the response of single atoms to interacting laser pulses, giving the resulting high harmonics. The third is its ability to propagate these generated high harmonics through the gas-filled capillary from the locations of their generation up until the end of the capillary. These three key parts of the code are then combined together to give a full simulation code capable of modelling this capillary-based HHG experimental set up.

Whilst a gas-filled hollow capillary has been used throughout this research, and the simulation code has been specifically developed for this generation geometry, gas cells and jets can also be modelled to a reasonable extent using this developed computer code. Gas cells can be modelled as a very short hollow capillary with a constant gas pressure across them and a width much wider than the laser pulse waist, and gas jets can be modelled in much the same way, except for possibly a gas pressure profile that increases and then decreases along the axis of laser propagation.

Different models of high harmonic generation have been developed by various groups. The most common models developed are for a single atom, though others for gas jets and cells, and gas-filled hollow capillaries have also been developed. There are limitations to these models though. The single atom models do not model macroscopic effects, others include a multi-atom geometry though have limited geometry lengths or limit positions at which the harmonic generation is calculated. For instance, Patchovskii et al. [83] developed a single atom model, and whilst this model is effective it cannot calculate the HHG resulting from macroscopic media. L'Hullier et al. [69] present a model that can calculate the HHG for macroscopic media on the other hand, though only for short lengths, which is typically the case for media such as gas jets. Gaarde et al. [47] present a HHG model that includes the harmonic generation for a short gas medium. Here this was also only for short medium lengths of 0.5 - 5 mm, and in order to reduce computational complexity the time-dependent dipole moment was not calculated at each step along the propagation direction. Tosa et al. [112] also developed a HHG model for gas jets, though for long gas jets up to 15 mm in length,

Group/Author	Single Atom Response	Gas Jet or Cell	Hollow Capillary (Limited)	HHG Simulated Throughout Entire Multi-cm Capillary
Patchovskii et al. [83]	✓			
L'Hullier et al. [69]	✓	✓		
Gaarde et al. [47]	✓	✓		
Tosa et al. [112]	✓	✓		
Jin et al. [61]	✓		✓	
Stein et al. [109]	✓	✓	✓	
Anderson [13]	✓	✓	✓	
This Work	✓	✓	✓	✓

TABLE 1.1: A table presenting various models for high harmonic generation and the scopes to what they simulate.

and also included approximations such as the string field approximation, which has been shown to result in inconsistencies in the harmonic plateau region [45]. Jin et al. [61] calculated the HHG for capillary waveguides. However, the harmonics were only calculated on the exit plane of the hollow waveguide rather than throughout the capillary itself, with just the laser propagation being determined throughout the capillary. Waveguide lengths were up to 12.8 mm, though with the HHG only being calculated at the end of the capillary, longer capillary lengths are also possible too. Stein et al. [109] developed a model that calculates the HHG for a semi-infinite gas cell of 6 mm in length, where the laser was again propagated throughout the cell though the HHG calculated at just the end. Due to the similarities in their modelling of the semi-infinite gas cell, gas-filled hollow capillaries should also be able to be modelled too using this approach. Anderson [13] modelled the HHG resulting from gas-filled hollow capillaries. This was limited to capillaries several mm in length due to the computational complexities involved, and whilst not explicitly included, it would be possible to model gas jets and certain cells using this model, provided certain approximations are included. The work presented here is a model for full HHG capillary simulations that follows on from the work on Anderson. Here HHG is calculated at many positions, both radial and longitudinal, throughout a multi-cm gas-filled capillary, giving both the HHG as seen at the end of the capillary and also as generated throughout the capillary. Again, the geometry modelled is not explicitly for gas jets or cells, though using approximations these can be included too. These different models of high harmonic generation are shown in Table 1.1, where the ticks indicate what each is able to model.

1.4 Thesis Outline

The outline of the thesis is given below. Here a brief discussion of each chapter is given in turn, providing a short overview of the purposes of each chapter.

1.4.1 Introduction

In this chapter an overview of high harmonic generation and its applications is given, as is the motivations of this work and this thesis outline.

1.4.2 Theory

The theory of laser pulse propagation in gas-filled capillaries is given in Chapter 2, as is the theory of high harmonic generation via the response of an atom to an intense laser pulse and the propagation of generated high harmonic. The theory presented in this chapter forms the theoretical description of the capillary-based HHG model used throughout the rest of the work.

1.4.3 Computational Implementation

The computational implementation of the theory discussed is given in Chapter 3. The pulse propagation model implementation is first given, then the single atom response implementation, the high harmonic propagation model, and finally the combined model. Schematic diagrams of each of these components are also presented which give an algorithmic overview of these computational models.

1.4.4 Validation

In Chapter 4 results are gained from the capillary-based laser pulse propagation model, the single atom high harmonic generation model, and the full capillary-based HHG model. These are each compared in turn to results from the literature to give insights into the validity of our model.

1.4.5 High Harmonic Generation Pump-Wavelength Efficiency

In Chapter 5 the driving wavelength dependence on high harmonic generation efficiency is investigated. A background to this is given first, then a discussion on the geometries used, key expected differences between numerical models, and the set up used when running simulations for this investigation. This is then followed by a presentation of the results for three geometries: a single atom, a sheet of atoms, and a gas-filled hollow capillary.

1.4.6 High Harmonic Generation Comparisons for Different Laser Systems

In Chapter 6 the high harmonic generation of different laser systems are compared against each other, with each system using the same gas-filled hollow capillary geometry. The generated harmonic spectra as seen at the end of the capillary are first compared, then are the laser profiles throughout the capillary and the corresponding high harmonic generation throughout the capillary are investigated and compared. Following this the harmonic generation for different length capillaries is investigated, and finally the gain in harmonic generation for different length capillaries is investigated too.

1.4.7 Conclusions

In this final chapter the conclusions of the work presented in this thesis are given and discussed, as is possible future work too.

Chapter 2

Theory

This chapter describes an advanced numerical model of high harmonic generation and propagation in a gas-filled hollow capillary. This is a complex system for modelling numerically as it involves laser pulse propagation within a multi-cm length gas-filled capillary, laser-gas interactions that result in high harmonic generation, and the propagation of those generated high harmonics along the remaining length of the capillary. In addition, the high harmonic generation and propagation need to also occur on the sub-nm scale along the length of the capillary for the overall resulting high harmonic generation to be accurately modelled.

The model presented here was originally described by P. Anderson [13] and has been expanded and completed. Here three separate models are presented, one for the laser pulse propagation, one for the high harmonic generation, and one for the propagation of the generated high harmonics. These models then combine together to give the full capillary-based HHG model.

2.1 Pulse Propagation Model

A high intensity laser pulse propagating through a gas-filled hollow capillary undergoes various nonlinear effects due to interactions with the gas, such as self-compression and spectral broadening. By accurately modelling the evolution of a laser pulse as it propagates through a gas-filled hollow capillary, a better understanding of its evolution can be obtained and HHG can be improved to give greater yields of desired wavelengths. To do this, a propagation evolution equation needs to be derived that provides a description of the processes involved.

2.1.1 Unidirectional Pulse Propagation Equation Derivation

A unidirectional pulse propagation equation (UPPE) adapted to a capillary geometry is derived in this section, which is used to propagate the driving laser pulse through the capillary. It was derived following the work of Couairon et al. [28], and Kolesik and Moloney [65] and assumes that the backwards propagating parts of the laser pulse are negligible compared to the forwards propagating parts, allowing for them to be discarded.

For a laser pulse propagating along the z-direction, the electromagnetic fields can be expanded in terms of modal contributions as

$$\boldsymbol{E}(x,y,z,t) = \sum_{m,w} A_m(\omega,z)\boldsymbol{\mathcal{E}}_m(\omega,x,y)e^{i\beta_m(\omega)z-i\omega t}, \tag{2.1}$$

$$\boldsymbol{H}(x,y,z,t) = \sum_{m,w} A_m(\omega,z)\boldsymbol{\mathcal{H}}_m(\omega,x,y)e^{i\beta_m(\omega)z-i\omega t}, \tag{2.2}$$

where A_m is the complex spectral amplitude, ω is frequency, m runs over all transverse modes, $\boldsymbol{\mathcal{E}}_m$ and $\boldsymbol{\mathcal{H}}_m$ are the transverse spatial modes of the electric and magnetic fields respectively, and β_m is the propagation constant of the m^{th} mode.

From here in, the modal fields will be written in the condensed form

$$\boldsymbol{\mathcal{E}}_m \equiv \boldsymbol{\mathcal{E}}_m(\omega,x,y)e^{i\beta_m(\omega)z-i\omega t} \tag{2.3}$$

$$\boldsymbol{\mathcal{H}}_m \equiv \boldsymbol{\mathcal{H}}_m(\omega,x,y)e^{i\beta_m(\omega)z-i\omega t}. \tag{2.4}$$

The Maxwell equations are given as

$$\nabla \times \boldsymbol{E} = -\mu_0 \partial_t \boldsymbol{H} \tag{2.5}$$

$$\nabla \times \boldsymbol{H} = +\varepsilon_0 \partial_t \left[\varepsilon(\tau) * \boldsymbol{E}\right] + \boldsymbol{J} + \partial_t \boldsymbol{P}, \tag{2.6}$$

where $*$ is a convolution, $\varepsilon(\tau)$ is the time domain representation of the frequency-dependent permittivity, $\varepsilon(\omega)$, $\boldsymbol{J}$ is the current density, and $\boldsymbol{P}$ is the nonlinear polarisation.

The Maxwell equations are then multiplied by the complex conjugate modal fields,

$$\boldsymbol{\mathcal{H}}_m^* \cdot \nabla \times \boldsymbol{E} = -\mu_0 \boldsymbol{\mathcal{H}}_m^* \cdot \partial_t \boldsymbol{H} \tag{2.7}$$

$$\boldsymbol{\mathcal{E}}_m^* \cdot \nabla \times \boldsymbol{H} = \boldsymbol{\mathcal{E}}_m^* \cdot (\boldsymbol{J} + \partial_t \boldsymbol{P}) + \varepsilon_0 \boldsymbol{\mathcal{E}}_m^* \cdot \partial_t \left[\varepsilon(\tau) * \boldsymbol{E}\right]. \tag{2.8}$$

By using the relation $\boldsymbol{B}\cdot(\nabla\times\boldsymbol{A}) = \nabla\cdot(\boldsymbol{A}\times\boldsymbol{B}) + \boldsymbol{A}\cdot(\nabla\times\boldsymbol{B})$ and the knowledge that the modal fields also satisfy the Maxwell equations, the two equations can be subtracted from each other to give

$$\nabla\cdot(\boldsymbol{H}\times\boldsymbol{\mathcal{E}}_m^*) - \partial_t(\mu_0\boldsymbol{\mathcal{H}}_m^*\cdot\boldsymbol{H}) - \nabla\cdot(\boldsymbol{E}\times\boldsymbol{\mathcal{H}}_m^*) = \boldsymbol{\mathcal{E}}_m^*\cdot(\boldsymbol{J}+\partial_t\boldsymbol{P}) + \partial_t(\varepsilon_0\boldsymbol{\mathcal{E}}_m^*\cdot\varepsilon(\tau)*\boldsymbol{E}). \tag{2.9}$$

This is then integrated over the xyt domain and provided the fields vanish at very large past and future times, and also far from the optical axis, gives

$$\partial_z\int\hat{z}\cdot(\boldsymbol{H}\times\boldsymbol{\mathcal{E}}_m^*)dxdydt - \partial_z\int\hat{z}\cdot(\boldsymbol{E}\times\boldsymbol{\mathcal{H}}_m^*)dxdydt = \int\boldsymbol{\mathcal{E}}_m^*\cdot(\boldsymbol{J}+\partial_t\boldsymbol{P})dxdydt, \tag{2.10}$$

where $\hat{z}$ is a unit vector.

The modal expansions given in Eqs. (2.1) and (2.2) can be substituted into this result and by applying the orthogonality relation,

$$\int\hat{z}(\boldsymbol{\mathcal{H}}_m\times\boldsymbol{\mathcal{E}}_n^* - \boldsymbol{\mathcal{E}}_m\times\boldsymbol{\mathcal{H}}_n^*)dxdy = 2\delta_{mn}N_m, \tag{2.11}$$

where δ_{mn} is the Kronecker delta and N_m is a frequency dependent normalisation, an equation describing the evolution of the spectral amplitudes is obtained as

$$\partial_z A_m(\omega,z) = -\frac{1}{2N_m(\omega)}\int\boldsymbol{\mathcal{E}}_m^*(x,y,\omega)e^{-i\beta_m(\omega)z+i\omega t}(\partial_t\boldsymbol{P}(\boldsymbol{r},t)+\boldsymbol{J}(\boldsymbol{r},t))dxdydt. \tag{2.12}$$

2.1.2 Spectral Evolution Equation for a Gas-Filled Hollow Capillary

The equation for the evolution of the spectral amplitudes, Eq. (2.12), is a general equation for any waveguide and optical non-linearity and so now needs to be specialised to the case of a hollow capillary filled with a gas. To do so, equations that give the propagation constants need to be introduced, as do equations that give the mode functions supported by the hollow capillary. Such equations were developed by Marcatili and Schmeltzer in 1964 [73] and for the polarisation axis of the electric field being the x-axis the mode functions are given by

$$\mathcal{E}_{m,x} = J_0\left(\frac{u_m}{a}r\right) \tag{2.13}$$

$$\mathcal{H}_{m,y} = -\sqrt{\frac{\varepsilon_0}{\mu_0}}\mathcal{E}_{m,x}, \tag{2.14}$$

where u_m are the roots of the zero order Bessel function of the first kind, J_0, and a is the radius of the hollow capillary. Here the mode functions supported by the capillary have been approximated to being just the linearly polarised and circularly symmetrical HE_{1m} modes. For our investigation we start with a linearly polarised Gaussian beam centred on the optical axis of the capillary and assume circular symmetry. As such we only

include these HE_{1m} modes in our model as this Gaussian beam is preferentially coupled into them and so these are the dominant modes present, as discussed in Section 2.1.5. The modal propagation constants, $\beta_m(\lambda)$, are given as [73]

$$\beta_m(\lambda) = \frac{2\pi n_{\text{gas}}}{\lambda}\left[1 - \frac{1}{2}\left(\frac{u_m\lambda}{2\pi a}\right)^2\right] + i\left(\frac{u_m}{2\pi}\right)^2 \frac{\lambda^2}{a^3}\left[\frac{n_{\text{glass}}^2 + 1}{2\sqrt{n_{\text{glass}}^2 - 1}}\right], \tag{2.15}$$

where λ is the wavelength and n_{glass} is the refractive index of glass. The refractive index of the neutral gas, n_{gas}, is given by a Sellmeier equation using the coefficients from Bideau-Mehu et al. [19]. The real part of the propagation constant describes the waveguide dispersion and the chromatic dispersion of the neutral gas, and the imaginary part describes the loss of the modes.

The mode functions for the hollow capillary are now substituted into the orthogonality relation and transformed into cylindrical coordinates, the integral within is evaluated in the limits between 0 and a to give

$$N_m = \pi\sqrt{\frac{\varepsilon_0}{\mu_0}}a^2 J_1(u_m)^2. \tag{2.16}$$

Here J_1 is the first order Bessel function of the first kind. Inserting this, along with the mode functions for the hollow capillary, into the radially symmetric form of the spectral amplitude evolution equation gives

$$\partial_z A_m(\omega, z) = -\sqrt{\frac{\mu_0}{\varepsilon_0}}\frac{e^{-i\beta_m(\omega z)}}{a^2 J_1(u_m)^2 T}\int_{-T/2}^{T/2}\int_0^a \left(\partial_t P(z,r,t) + J(z,r,t)\right) J_0\left(\frac{u_m}{a}r\right) e^{i\omega t} r dr dt, \tag{2.17}$$

where T is a large window in time. By realising that the second fraction term combined with the double integral is a Hankel transform in space and a Fourier transform in time, giving a discrete spectral transform, the resulting spectral evolution equation describing the linearly polarised EH_{1m} modes of a gas-filled hollow capillary is given as

$$\partial_z A_m(\omega, z) = \sqrt{\frac{\mu_0}{\varepsilon_0}} e^{-i\beta_m(\omega)z}\left[i\omega\tilde{P}\left(z, \frac{u_m}{a}, \omega\right) - \tilde{J}\left(z, \frac{u_m}{a}, \omega\right)\right]. \tag{2.18}$$

The terms $\tilde{P}$ and $\tilde{J}$ in Eq. (2.18) are the Fourier transformed in time and Hankel transformed in radial direction nonlinear polarisation of the gas related to optical Kerr and Raman effects and the current density, respectively.

There are many possible modes supported by the hollow capillary, all of which can be included via Eq. (2.12). For instance, the transverse electric, TE, transverse magnetic, TM, and hybrid, HE and EH, modes [73]. For transverse electric modes the electric field has axial components equal to zero, with the transverse component being non-zero, for transverse magnetic modes the magnetic field has axial components equal to zero, with the transverse component being non-zero, and for hybrid modes all these components

are non-zero. The high harmonic generation model of Section 2.2 argues that HHG only occurs for an atom if the light interacting with it is linearly polarised, limiting the possible modes that can generate high harmonics. However, this does not exclude any of the TE, TM, HE, and EH modes as all of them can be made linearly polarised locally, even though the direction of this linear polarisation will in general depend on the position. In practice, though, the initial laser beam is close to a linearly polarised HE_{11} mode, with the polarisation being in the same direction everywhere and circularly symmetric in space, and so the induced medium polarisation, P, and current density, J, will have the same circular symmetry around the capillary axis and Eq. (2.12) will couple only to the HE_{11} and other HE_{1m} modes. Therefore, the propagation equation derived in Eq. (2.18) for the linearly polarised radially symmetric modes can be used. If other modes than these HE_{1m} modes are desired to be included then spectral evolution equations for either the full set of possible modes, or a subset of modes different to the linearly polarised HE_{1m} modes, would need to be obtained by inserting their hollow capillary electric field modes and propagation constants into Eq. (2.12). However, for these other modes to be included in the model developed within this work, as discussed in Chapter 3, this would break the required circular symmetry approximation and so the model would need to be adapted to facilitate them.

2.1.3 Nonlinear Polarisation

The nonlinear polarisation, P, of an atomic gas can be given as [22]

$$P(t) = \varepsilon_0 \chi^{(3)} E(t)^3, \tag{2.19}$$

where ε_0 is the permittivity of free space, $\chi^{(3)}$ is the third-order nonlinear susceptibility, and $E(t)$ is the electric field at a time t. This equation describes the source of third-order optical nonlinearities, such as self-focussing, self-phase modulation, and third-harmonic generation, though it does not describe HHG.

To obtain a nonlinear polarisation term that models HHG the time-dependent electron acceleration given later in Eq. (2.34) of Section 2.2, though for reference is [46]

$$\tilde{P}(\omega) = \mathcal{F}\left[N_a(t) a(t) D(t)\right], \tag{2.20}$$

where $\tilde{P}(\omega)$ is the nonlinear polarisation in the spectral domain, $\mathcal{F}$ represents a Fourier transform, $N_a(t)$ is the density of neutral atoms, $a(t)$ is the electron acceleration, and $D(t)$ is a window function that brings the combined terms within the Fourier transform to zero at the ends of the time axis so that a correct Fourier transform can be taken.

In terms of computational implementation, including the nonlinear polarisation in the spectral evolution equation means that there is a wide range of frequencies being used and stored in memory due to the nonlinear polarisation containing wavelengths all the

way down to sub-nanometer wavelengths, whilst also containing wavelengths similar to the driving pulse. This makes the arrays holding the nonlinear polarisation and the spectral amplitudes much larger in size and also increases computation times as there are far more elements to do the computations on. To solve this, there can be two sets of arrays and two sets of propagations, one for the wavelengths of similar magnitudes to the driving laser, and another for the smaller wavelengths on the scale of the high harmonics.

Another issue is that the single atom response code that is used to generate the nonlinear polarisation takes a considerable amount of time to run its calculations, relative to the pulse propagation code. As the pulse propagation implementation also uses an adaptive step size, the single atom response calculations would be called multiple times per propagation step, making the pulse propagation code slow and impractical. If the nonlinear polarisation is small compared to the current density however then it has a negligible effect on the pump spectral amplitude evolution and can therefore be ignored. As such, for the laser pulse propagation the nonlinear polarisation is assumed to be small compared to the current density and so it is neglected [13].

2.1.4 Current Density

As the laser fields being used are strong enough to cause ionisation within the gas, the current density is non-zero. Here the current density is governed by three terms, with the general equation describing its evolution being given as [29]

$$\partial_t J(t) = -\frac{e^2 \rho(t) E(t)}{m_e} - \frac{J(t)}{\tau_c} - \varepsilon_0 c \partial_t \left(\frac{\sum_q \left(\rho_q(t) W_q(t) I_q \right) E(t)}{|E(t)|^2} \right). \tag{2.21}$$

Here e is the electron charge, $\rho(t)$ is the total free electron density given as $\rho = \sum_q q\rho_p$, $E(t)$ is the driving electric field causing the ionisation and current density, m_e is the electron mass, τ_c is the collision time, and ρ_q, W_q, and I_q denote the density, ionisation rate, and ionisation potential of the charge state qe respectively.

The first term of this current density equation describes the charge's acceleration and is responsible for the blueshift of a laser pulse in an ionised gas, the second term describes the collisional damping, and the third term accounts for losses due to ionisation induced absorption. By assuming low gas pressures and short laser pulse times, as is typical in HHG, the second term can be neglected as the collision time is then large compared to the duration of the laser electric field. This results in a reduced current density equation that is now governed by two terms [29],

$$\partial_t J(t) = -\frac{e^2 \rho(t) E(t)}{m_e} - \varepsilon_0 c \partial_t \frac{\rho(t) W(t) I_p E(t)}{I(t)}, \tag{2.22}$$

where $I(t)$ is the intensity corresponding to $E(t)$. For simplicity only the effects of a single electron per atom and its corresponding singular charge state are considered. This is the equation describing the evolution of current density that is used within the laser pulse propagation model presented.

A framework for studying strong field ionisation was developed by Keldysh [63, 85]. This framework includes both multiphoton ionisation and tunnel ionisation, the latter being the dominant ionisation mechanism in HHG. In this framework a parameter known as the Keldysh parameter, γ, gives the ratio between the frequency of the pump laser pulse, ω, and the frequency of the electron tunnelling through a potential barrier, ω_t, as [85]

$$\gamma = \frac{\omega}{\omega_t} = \frac{\omega\sqrt{2m_e I_p}}{eA_{peak}}, \tag{2.23}$$

where I_p is the ionisation potential, and A_{peak} is the peak value of the electric field amplitude. The Keldysh parameter shows which ionisation mechanism is dominant. For $\gamma > 1$ multiphoton ionisation is the main ionisation mechanism, and for $\gamma < 1$ tunnel ionisation is the main ionisation mechanism.

The ionisation rate used within the model assumes a linearly polarized electric field and is given as [85]

$$W(t) = \omega_{at}\kappa^2\sqrt{\frac{3}{\pi}}C_{\kappa l}^2 2^{2n*}F(t)^{3/2-2n^*}e^{-\frac{2}{3F(t)}}, \tag{2.24}$$

where ω_{at} is the atomic unit of frequency and $\kappa = \sqrt{I_p/I_h}$ relates the ionization potential I_p of the gas under consideration to that of atomic hydrogen I_h. The coefficient $C_{\kappa l}$ describes the asymptotic behaviour of the atomic wavefunction far from the nucleus, and has a value that can be found in the work of Popov [85]. The effective quantum number is given by $n^* = 1/\kappa$, and $F(t) = E(t)/(\kappa E_{at})$ is the reduced electric field with E_{at} being the electric field atomic unit. The free electron density used in Eq. (2.22) is then given by

$$\rho(t) = N_a\left(1 - e^{-\int_{-\infty}^{t} W(t')dt'}\right) \tag{2.25}$$

where N_a is the initial density of neutral atoms [116].

2.1.5 Laser Coupling into Capillaries

When a laser pulse is launched into a hollow capillary it can be coupled into a vast number of modes supported by that capillary. In this model it is assumed that only the HE_{1n} modes are present. This is as the implementation of this model requires circular symmetry within the capillary, which is provided by the HE_{1n} modes.

Provided the laser pulse is launched centred on the capillaries optical axis, and with an initial circular symmetry, the laser will couple into the capillary with circular symmetry.

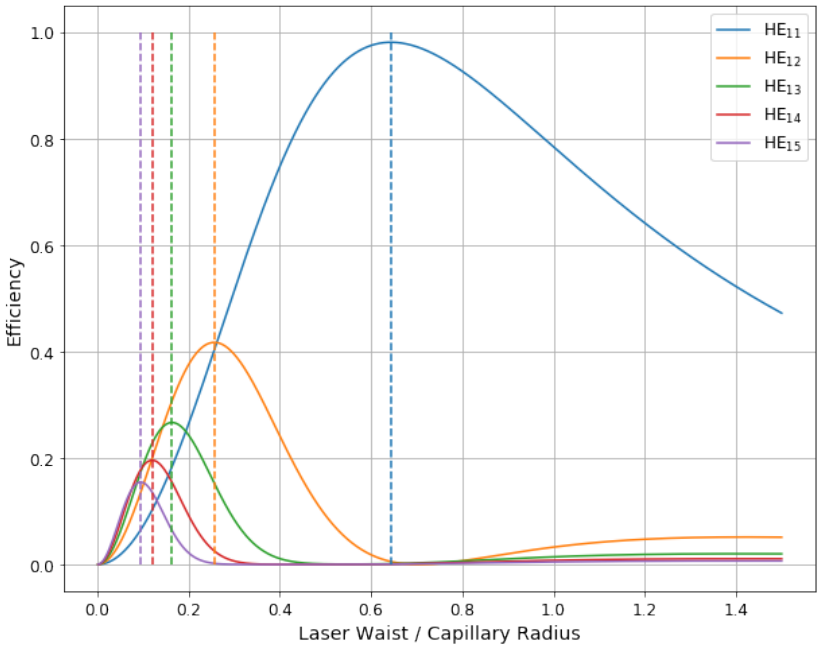

FIGURE 2.1: Coupling efficiency of a laser pulse into a hollow capillary, for different laser pulse waists to capillary radius ratios.

In experiments this is hard to achieve perfectly, though to a good approximation it is possible and so is fair to assume this is the case and that the dominant set of modes present are the HE_{1n} modes, with other modes being negligible.

The mode HE_{11} has the highest transmission through a hollow capillary [81] and it is therefore usually assumed that optimising the coupling into this mode will provide the best results for high harmonic generation as the laser pulse will have a longer interaction length with the gas in the capillary before significant losses take effect. This assumption is made throughout this work as well.

It was shown by Nubling and Harrington that to achieve optimal coupling with a Gaussian beam profile into the HE_{11} mode of a capillary the laser pulse waist should be 64% of the capillary radius [81]. This finding, along with the couplings for the other first four HE_{1n} modes are reproduced in Figure 2.1 using the overlap integral [81],

$$\eta_m = \frac{\left\lfloor \int_0^a \exp\left(-r^2/\omega^2\right) J_0\left(u_m \frac{r}{a}\right) r dr \right\rfloor^2}{\int_0^\infty \exp(-2r^2/\omega^2) r dr \int_0^a J_0^2\left(u_m \frac{r}{a}\right) r dr} \tag{2.26}$$

where ω is the spot size of the Gaussian beam, a is the bore size of the hollow capillary, and $0 \leq r < a$. The dotted lines in the figure show the waist to radius ratios that give the optimal coupling for their respective modes.

2.1.6 Gas Pressure Profile

A gas pressure profile has also been added and was done so that the ionisation of the gas, plasma density, pump pulse propagation, and absorption of harmonics could be more accurately modelled. Here we have assumed the experimental setup of Refs. [24, 25, 43, 44] and thus we model a 7 cm capillary with gas inlets at 2 cm inwards from each end, with the capillary itself placed in a vacuum. This causes the gas pressure between the two inlets to be kept at a constant maximum gas pressure, whilst the gas profiles in the end sections having linear decreases from the maximum gas pressure to around 80% of it over the first 2 mm going from the gas inlet to the capillary end, and then having linear decreases from 80% of the maximum gas pressure to zero gas pressure continuing along the capillary to the ends. The gas pressure profile along the capillary has previously been calculated by computational fluid dynamics (CFD) and can be approximated by a piecewise linear function as shown in Fig. 2.2 [92].

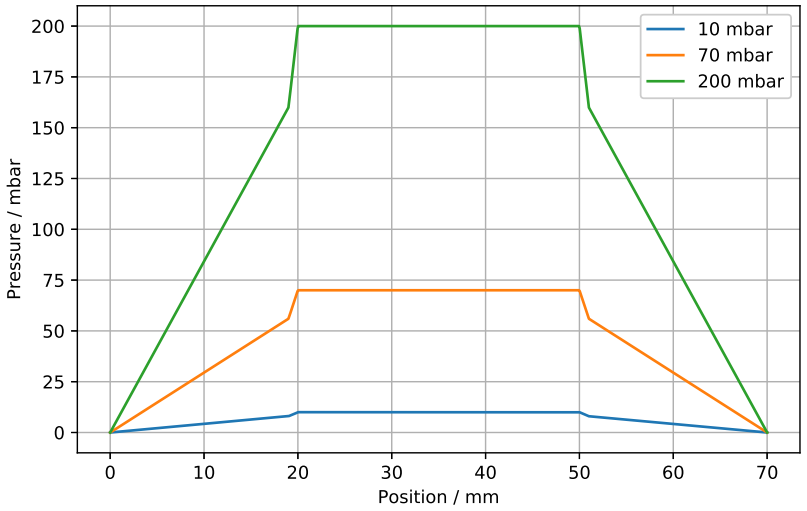

FIGURE 2.2: Pressure profile as a function of position along a capillary with two gas inlets at positions 2 and 5 cm, for gas pressures of 10, 70 and 200 mbar [92].

2.2 High Harmonic Generation Model

High harmonic generation is a nonlinear optical generation process in which a driving laser generates short wavelength radiation within the XUV and SXR regimes. A semi-classical three-step model can be used to describe it, and whilst this model does not provide a full description, it does give a good insight into the process.

This semi-classical three-step model was developed by Corkum in 1993 [27], having since been extended by various groups [99, 67]. In this model, the electric field of an intense laser field distorts the atomic potential of the atom, causing the electron tunnelling probability to increase and resulting in the outer electron tunnelling out of the

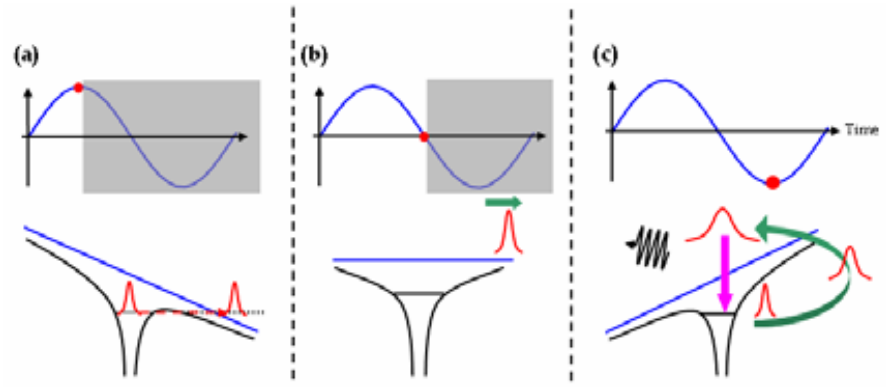

FIGURE 2.3: Semi-classical three step model of high harmonic generation by interaction with a laser pulse, reprinted from S. L. Stebbings et al. [108].

atomic potential and into the continuum, as shown in figure 2.3(a). In the continuum, for a linearly polarized electric field, this electron is accelerated away from the atom by the laser field, figure 2.3(b). When the electric field reverses direction after half an optical cycle the electron accelerates back towards the atom, recombining and resulting in the emission of an energetic photon in the XUV or SXR regime, as shown in figure 2.3(c).

The semi-classical three-step model gives insights into the laser intensities needed for HHG, the maximum photon energy that can be generated, the need for linear polarization of the driving pulse, and the causes of radiation generation at harmonics of the driving pulse.

The maximum photon energy that can be generated, also known as the classical cut-off energy, gives the point at which classically the high harmonic spectrum generated sharply drops off and stops being observed. This classically-calculated cut-off energy, used later within Chapter 5, is given by [66]

$$E_c = I_p + 3.17U_p, \tag{2.27}$$

where I_p is the ionisation potential of the atom and U_p is the pondermotive potential, which is itself given as [22]

$$U_p = \frac{e^2A^2}{4m_e\omega^2}. \tag{2.28}$$

Here e is the electric charge, A is the amplitude of the laser electric field, m_e is the electron mass, and ω is the angular frequency.

As can be seen by Eqs. (2.27) and (2.28), to extend the maximum harmonic energy being generated one either needs to increase the laser field strength or use longer driving wavelengths. This provides two routes to the generation of harmonics at progressively higher energies. The first route results in a linear scaling with the driving laser intensity, with therefore laser intensities very quickly growing. The second route involves

a scaling with the squared wavelength of the driving laser, λ^2. As discussed later in Chapter 5, this in itself can have its drawbacks too.

This three-step model does not show details of the generation process however, nor does it capture or explain the typical high harmonic spectra observed in such systems which exhibit a nearly constant intensity over many orders of high harmonics (called the plateau) followed by rapidly decreasing intensities at harmonic orders beyond the classical cut-off energy. To explain these features a fully quantum model is required, e.g. by solving the time dependent Schrödinger equation (TDSE).

Full three-dimensional quantum models have successfully been employed to simulate HHG in single atoms [83] as well as macroscopic media though these have been limited to gas jets [47] and hollow waveguides of lengths up to 13 mm [61]. The largest limitations to all these models is the computational complexity and times involved, and hence the macroscopic-scale limitations. Other non-TDSE three-dimensional models have also been employed [60] though again with similar limitations. To simulate HHG in media with longer interaction lengths, or with higher resolution, models with reduced computational complexity are needed.

The simplest quantum description that is in agreement with observations is a one-dimensional model of an atom with a single active electron [34, 35, 36, 89, 90, 91, 96, 97, 98]. Such a one-dimensional model predicts larger amounts of ionisation than a full three-dimensional model but generates remarkably similar harmonic spectra, discussed later in Chapter 4, whilst allowing for efficient computer simulation because of the significantly reduced computational complexity [88]. Whilst a one-dimensional model introduces approximations that can lead to inaccuracies, the work of Silaev et al. [106] showed that for driving pulse widths greater than around 4 - 5 fs and for driving intensities less than 4×10^{14} W/cm^2 the one-dimensional soft Coulomb potential can show very close agreement to the three-dimensional model.

A soft Coulomb potential is used in our model and is given as

$$V_{Coulomb} \propto \frac{1}{\sqrt{x^2 + \alpha^2}}, \tag{2.29}$$

where x is the distance from the atom, and α is a parameter used to scale the Coulomb potential to match the ground state energy of the atom. In all the models presented, and in all simulations run, α took the value of 1.45. This value of α gives rise to a ground state energy of -15.77 eV in the HHG model, corresponding to that of argon [114]. The soft Coulomb potential was used to avoid the singularity that is found in the Coulomb potential in one-dimension.

The response of a single atom to the time-dependent electric field of the laser pulse $E(t)$ discussed above is described by a quantum mechanical model for the electron wavefunction ψ. For simplicity and numerical efficiency the single active electron and

one-dimensional approximations are employed [88]. The single-electron Schrödinger equation is thus [88]

$$i\hbar\frac{\partial}{\partial t}\psi(t) = \hat{H}\psi(t) \tag{2.30}$$

with the Hamilton operator

$$\hat{H} = \hat{K} + \hat{V} = -\frac{\hbar^2}{2m_e}\frac{\partial^2}{\partial x^2} - \left(\frac{e^2}{4\pi\epsilon_0\sqrt{\alpha + x^2}} + xeE(t)\right). \tag{2.31}$$

Here $\hbar$ is the reduced Planck constant, m_e is the mass of the electron and x is the position from the centre of the Coulomb potential. The kinetic energy operator is given as $\hat{K}$ and the potential energy operator $\hat{V}$ comprises the soft Coulomb potential and the laser electric field potential, $V = xE(t)$, where $E(t)$ is the electric field of the laser pulse. The initial state of the electron wavefunction is given by the stationary ground state solution of Eq. (2.30) in the absence of the laser field.

The Schrödinger equation can be solved numerically using finite difference methods, such as the Crank-Nicholson method, though throughout the model presented here a pseudo-spectral method known as a symmetrised split-step Fourier method is used [33].

To derive the time propagator of the wavefunction using this method, the formal solution of the Schrödinger wave equation is first given as

$$\psi(x, t_2) = e^{-\hat{H}\Delta t}\psi(x, t_1), \tag{2.32}$$

where $\Delta t = t_2 - t_1$, with t_2 being the time at the next step and t_1 being the time at the current step. From here the Hamiltonian is split into its kinetic and potential energy components, $\hat{K}$ and $\hat{V}$, and through use of the Strang splitting formula, a time propagator is derived,

$$\psi(x, t_2) = e^{\frac{-i\hat{K}\Delta t}{2}} e^{-i\hat{V}\Delta t} e^{\frac{-i\hat{K}\Delta t}{2}} \psi(x, t_1). \tag{2.33}$$

The aim of the splitting is that the separate components in the final time propagator can be calculated either in coordinate space or in the spectral domain, allowing for the direct calculations of partial derivatives to be avoided and also allowing for a better accuracy and computation time than Crank-Nicholson schemes.

For a 5 fs pulse width, 780 nm wavelength laser pulse with a peak intensity of 3.0×10^{18} Wm^{-2} interacting with an argon atom the resulting wavefunction calculated using this model is given in Figure 2.4, plotted on a $\log_{10}$ scale and with the laser pulse superimposed. Figure 2.4 shows that as the laser pulse arrives parts of the electron wavefunction tunnel away from the core and spread out radially from the atom. When the laser field reverses the parts of the electron wavefunction in the continuum return and

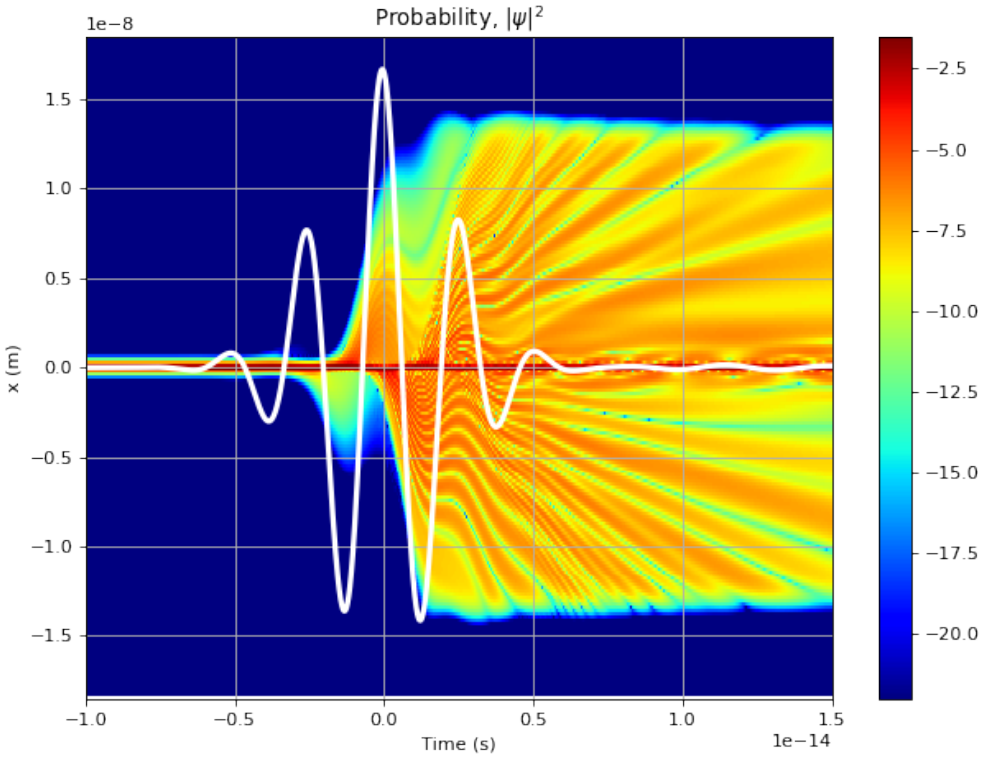

FIGURE 2.4: Probability of the one-dimensional electron wavefunction due to a 5 fs pulse width, 780 nm wavelength laser pulse with a peak intensity of 3.0×10^{18} Wm^{-2} at different positional displacements away from the atom core, varying with time and plotted on a $\log_{10}$ scale.

interfere with the core, causing oscillations of the electron density function. These oscillations produce a dipole moment, which is the source of the high harmonics. In Figure 2.4 the probability quickly diminishes at the edges of the spatial grid, this is due to the absorbing boundary condition $1 - \sin\left(\frac{\pi x}{2x_{max}}\right)^{50}$ being applied. This prevents the parts of the wavefunction that are escaping from interfering non-physically with the remaining wavefunction, which would otherwise be the case due to the periodic boundary condition of the Fourier transform method used in solving Eq. (2.33).

The dipole moment can be gained from the wavefunction and used to calculate the harmonic spectrum. Instead, from the solution of Eq. (2.30) the acceleration of the electron can be found via the Ehrenfest theorem by

$$a(t) = \frac{d^2}{dt^2}\langle x \rangle = -\frac{1}{\hbar^2}\left\langle \left[\hat{H}, \left[\hat{H}, \hat{x}\right]\right]\right\rangle, \tag{2.34}$$

where $\langle \dots \rangle$ is the expectation value with respect to $\psi(t)$. This gives a more accurate result for the harmonic spectra than the dipole moment due to small errors in the wavefunction propagating near the boundary becoming large errors in the time-dependent dipole [46]. Finally, the generated high harmonic spectrum is found through the Fourier

transform $\mathcal{F}$ of the acceleration by

$$\tilde{P}(\omega) = \mathcal{F}\left[N_a(t)a(t)D(t)\right], \tag{2.35}$$

where $N_a(t)$ is the density of neutral atoms, ω the angular frequency of the generated harmonic field, and $D(t)$ a window function to bring the terms of the Fourier transform to zero at both ends of the time axis. The harmonic spectrum as given by Eq. (2.35) gives the harmonic spectrum in the near-field and is used throughout this work.

Both the TDSE model and the three-step model capture useful information; however, there are differences between the information and insights they provide. For instance, as already mentioned, a classical cutoff energy can be determined from the three-step model that gives the maximum possible energy that the harmonics can be generated at, given by Eq. (2.27). Lewenstein et al. instead showed that following a fully quantum theory of HHG the cutoff is instead given by [67]

$$E_c = I_p F(I_p/U_p) + 3.17U_p \tag{2.36}$$

where $F(I_p/U_p)$ is a term that takes account of both the tunnelled electron not originating directly at the core but close to it and also the effects of quantum diffusion on the electron wave packet, and is a function that takes the value of 1.32 for small values of I_p/U_p and decreases towards 1 as I_p/U_p grows. The three-step model does not account for these factors and so predicts maximum harmonic energies less than what would actually be achieved. The TDSE however does include these effects within its modelling and so predicts the more accurate maximum harmonic energies. Despite this difference in calculated cutoff energy, the classical cutoff is commonly used as it typically gives only relatively small differences to the more accurate cutoff value and so is still a good indicator of maximum possible generated harmonic energy.

Additionally, within the three-step model the potential of the atom is ignored for the electron motion and so the electron is treated as freely moving, under only the influence of the laser field. The TDSE model on the other hand includes the atomic potential for the electron wavefunction evolution at all times.

The three-step model gives an easy to conceptualise and understand model whereas for the TDSE model it is harder to conceptualise what is happening within it. This is since within the three-step model electron trajectories are treated classically with very well defined motion, whereas this is not the case with electron wavefunctions of the TDSE model, though the latter gives more accurate results. Additionally, the TDSE model also accounts for the tunnelling process of the electron not being an instantaneous event whereas the three-step model assumes it to be.

Both the three-step and TDSE models also capture the phase of the generated harmonics, show how the harmonics do not arise from a single optical cycle but instead arise

from the interference of multiple optical cycles, and also explain the origin of the presence of only odd harmonics, which is due to the harmonics generated from multiple optical cycles most efficiently constructively interfering for odd harmonics as these are in-phase whereas other harmonic energies are not and so experience either less efficient constructive interference or instead destructive interference. Within the three-step model for all possible harmonic energies except the maximum harmonic energy at the cutoff, there are two emission times for the electron that give rise the same harmonic energy, where one results in a much longer time in the continuum for the electron than the other, with these being known as the long and short electron trajectories respectively, and with the difference in time spent in the continuum giving rise to different phases between these two electron trajectories. Whilst the TDSE model also includes the long and short trajectories, it includes higher order returns still, as well as more complex irregular time-delayed returns, with the harmonic plateau having been shown to be the result of interference between these irregular time-delayed returns and the regular electron returns [113]. This harmonic plateau is a feature that the three-step model is not able to capture, which the TDSE model does, and is an important feature to be able to capture and model accurately as many experiments use harmonics generated from within the plateau rather than at the cutoff.

2.3 High Harmonic Propagation Model

Harmonic radiation can be propagated in both free space and in different media via many different propagation techniques. In the near field the angular spectrum method, ASM, [105, 53] can be used as a suitable technique, and in the far field the Fraunhofer diffraction [21] method can be used. In the final step of HHG simulation in a gas-filled hollow capillary, the high harmonic radiation needs to be propagated from the position of the atom where it is generated to the end of the capillary. Here we perform this propagation through the angular spectrum method due to the harmonic radiation being in the near field.

The ASM decomposes an electric field into cylindrical waves, with each component propagating at a different angle to the capillary's optical axis. In this angular spectrum form a propagator is applied and then the result is transformed back into the spatial field distribution at the final position. Within the confines of radial symmetry a Hankel transform can be used for these transforms, saving computational time and resources compared to a two-dimensional Fourier transform.

The harmonic field propagated to the end of the capillary, $E(Z,r)$, is given below by Eq. (2.39) and integrated over all simulated radiating atoms in the capillary. This is the expected output of the high harmonic source which is then used throughout the rest of this work to give the generated harmonic field as seen at the end of the capillary.

2.3.1 Angular Spectrum Method for Propagating High Harmonics in a Gas-filled Hollow Capillary

The angular spectrum method decomposes an electric field into cylindrical waves, with each component propagating at a different angle to the optical axis of the field. In this angular spectrum form a propagator is applied and then the result is transformed back into the field distribution at the new propagated position.

In one- and two-dimensional Cartesian coordinates this decomposition can be done through use of a Fourier transformation, though in the radially-symmetric case computational resources, requirements and time can be reduced by using a Hankel transform instead. This is a one-dimensional transform as opposed to a two-dimensional transform.

The Hankel transform is defined as

$$\mathcal{H}\{f(r)\} = \tilde{f}(k_r) = 2\pi \int f(r) J_0(2\pi r k_r) r dr, \tag{2.37}$$

where the Hankel transform, $\mathcal{H}$, is identical to its inverse, $\mathcal{H}^{-1}$, and k_r is the radial component of the propagation constant in the transformed domain. For the discrete Hankel transform, where $r < R$, k_r takes the values

$$k_r = \frac{u_m}{R}, \tag{2.38}$$

where u_m are the roots of the zero order Bessel function of Eq. (2.15).

Modifying the method of Guizar-Sicairos and Gutiérrez-Vega [53] to account for the harmonic radiation propagating in a medium rather than free space, our ASM is given by

$$E(Z,r) = \mathcal{H}^{-1}\left\{\mathcal{H}\left\{(E(z,r)\right\} e^{-i\int_z^Z \sqrt{(kn(z'))^2 - k_r^2}dz'}\right\}, \tag{2.39}$$

The position at the end of the capillary is given by Z and the initial position of the generated harmonic is given by z. The position-dependent refractive index of the medium, $n(z)$, is integrated over the distance the harmonic propagates to account for the effects of a non-constant gas pressure and thus non-constant refractive index and absorption. Note that the Hankel transform imposes perfectly reflecting boundary conditions for the capillary walls and so implies perfect reflection of the high harmonics on the capillary walls.

2.3.2 Angles of Propagation for Propagating High Harmonics

As mentioned, the Hankel transform imposes perfectly reflecting boundary conditions on the capillary walls, resulting in perfect reflections of the high harmonics on them.

This is realistic for X-rays that hit the capillary wall with grazing angles [15] and so all harmonics with propagating angles larger than 0.331° were filtered out for the analysis. This limiting angle was chosen in line with the experimental geometry investigated in our group [43, 44, 25, 24]. In this setup the HHG source is 2.2 m away from a 1 inch diameter mirror that reflects the high harmonics through a pinhole and onto the sample to be imaged. Harmonics propagating at large enough angles therefore miss this mirror and so are lost. For this experimental setup the resulting limiting angle is the already mentioned 0.331^o.

The angles the harmonics are propagating at can be calculated by the equation

$$\theta = \arccos\left(\frac{\sqrt{k^2 - k_r^2}}{k}\right). \tag{2.40}$$

From this the angles of the harmonics are determined and then those greater than the given limiting angle are filtered out.

2.3.3 Refractive Index and High Harmonic Absorption

Within the extreme ultraviolet and soft x-ray regimes the Sellmeier equation can no longer be used for calculating the refractive index of the gas. Instead, the complex refractive index is determined from the atomic scattering factors of the gas used, given here by [55, 2]

$$n(z,\lambda) = 1 - \left(\rho_{at}(z)\frac{r_0\lambda^2}{2\pi}(f_1(\lambda) + if_2(\lambda)\right), \tag{2.41}$$

where $\rho_{at}(z)$ is the gas atom density at position z along the capillary, r_0 is the classical electron radius, λ is the harmonic wavelength in question, and f_1 and f_2 are the real and complex parts of the atomic scattering factor, respectively. The scattering factors are gained from experiment and have been downloaded [2] for ease of use. Inside a simulation these are then interpolated so that their spacings in terms of wavelength match those of the high harmonic wavelength spacings. Within our model implementation this interpolation is performed using an Akima cubic spline [11].

High harmonics generated within the capillary undergo significant absorption, with the amount being dependent on their energy. Figure 2.5 shows the proportion of harmonics that are transmitted to the end of a 7 cm length 150 mbar pressure argon-filled hollow capillary with the gas pressure profile of Figure 2.2. Here a harmonic of a particular energy is generated at a given position within the capillary and the corresponding transmission value gives the remaining proportion of that harmonic as seen once it has been propagated to the end of the capillary and experienced absorption by the gas present. For energies between 16 - 40 eV there is significant absorption with only those harmonics generated in the last few mm of the capillary able to reach the end of the

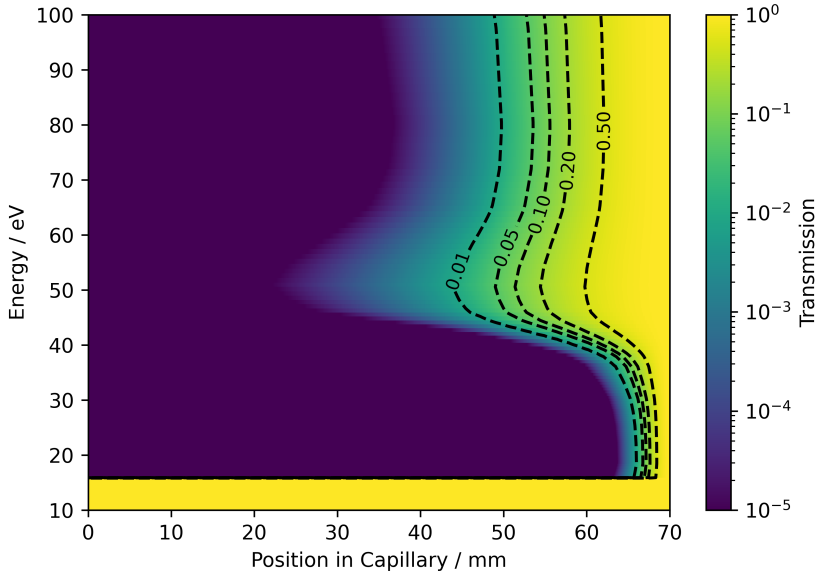

FIGURE 2.5: Transmission of high harmonics generated within a 7 cm length, 150 mbar pressure, argon gas-filled hollow capillary as they propagate from their generation positions to the capillary end. The black dotted lines indicate given transmission levels across different harmonic energies and capillary generation positions.

capillary before they experience too much absorption and become negligible. For harmonic energies of 45 - 100 eV, however, those generated within the final couple of cm of the capillary can still be observed in non-negligible amounts at the end of the capillary.

2.3.4 Atomic Density of the Gas

The gas pressure profile used is the same as that described in Section 2.1.6. This contains five sections of linear pressure. The first section is the increasing pressure from the start of the capillary to just before the first gas inlet. The second section is from just before the gas inlet to the gas inlet itself. The third section is the distance between the first and second inlet. The fourth section is from the second inlet to just after it, and the fifth section is from just after the second gas inlet to the end of the capillary.

To propagate the harmonics from their generated positions to the end of the capillary they can either be propagated along each step, with each step having an instantaneous atomic density equal to the atomic density at that position in the capillary, or they can be propagated straight to the end of the capillary, with the atomic density being the total atomic density from the generation position to the end of the capillary. The first method was the initial method used in this model though it was later changed to the second as each generation position in this method is not dependent on any other, allowing for multiple propagations to take place simultaneously.

The total atomic density can be calculated by integrating the instantaneous densities along the length of the capillary, starting at the generation position. That is,

$$N_{total} = \int_{z}^{Z} \rho(z')dz', \tag{2.42}$$

where, for example, $z = 0$ for a harmonic generation position at the start of the capillary, and $z = Z/2$ for a harmonic generation position halfway along the capillary, etc. The integral of this can be split into five smaller integrals, one for each of the sections mentioned above. That is,

$$\int_{z_1}^{z_6} \rho(z')dz' = \int_{z_1}^{z_2} \rho(z')dz' + \int_{z_2}^{z_3} \rho(z')dz' + \int_{z_3}^{z_4} \rho(z')dz' + \int_{z_4}^{z_5} \rho(z')dz' + \int_{z_5}^{z_6} \rho(z')dz'. \tag{2.43}$$

In these, z_i is the starting position of section i, z_{i+1} is the ending position, and T is the length of the small sections just before/after gas inlet $1/2$, respectively. These integrals can be solved analytically and, for N_{max} being the maximum atomic density in the capillary and Z being the total length of the capillary, are given as

$$N_1 = \frac{0.8N_{max}}{2(I_1 - T)}(z_2^2 - z_1^2) \tag{2.44}$$

$$N_2 = \frac{N_{max}}{T}(0.1z_3^2 - (0.2I_2 - T)z_3 - 0.1z_2^2 + (0.2I_2 - T)z_2 \tag{2.45}$$

$$N_3 = N_{max}(z_4 - z_3) \tag{2.46}$$

$$N_4 = \frac{N_{max}}{T}(0.1z_4^2 - z_4(T + 0.2I_2) - 0.1z_5^2 + z_5(T + 0.2I_2) \tag{2.47}$$

$$N_5 = \frac{0.4N_{max}}{Z - (I_2 + T)}(2Z(z_6 - z_5) - z_6^2 + z_5^2) \tag{2.48}$$

where I_1 is the position of the first gas inlet, and I_2 is the position of the second gas inlet.

To calculate the total atomic density in the capillary from the position of harmonic generation to the capillary end only the length that the harmonic propagates through needs to be included. Therefore, when calculating this, if the harmonic is past a section then that section is not included, if it is part way through a section then that sections starting position, z_i, is replaced with the harmonic generation position. All subsequent sections are still included in full. These relevant section are then summed together to give the total. That is, for example,

$$N_{total} = N_1 + N_2 + N_3 + N_4 + N_5, \tag{2.49}$$

for the whole length of the capillary, and for a harmonic generation position half way along the capillary it is instead

$$N_{total} = N_3(z_3 = Z/2) + N_4 + N_5. \tag{2.50}$$

2.3.5 Interpolation of High Harmonic Sources Between Propagation Steps

High harmonic generation and propagation needs to occur on the nanometer or sub-nanometer scale to correctly capture the phase difference, interference, and coherence between spectra generated by different atoms within the capillary. The laser pulse propagation model used typically propagates the laser on the micrometer scale, and the capillary length is typically on the cm scale. To get the resolution needed in the high harmonic generation and propagation, the number of steps needed to be used in the combined simulation code is of the order 10^8, which then gives a sub-nanometer step size. This large number of steps would require 10^8 single atom response calculations per radial point, which would take a longer time than is practically or feasibly possible. To overcome this, interpolation can be employed to drastically reduce the number of single atom response calculations. This can be done, for example, by having the number of steps being in the order of 10^4 and then calculating 10^4 interpolation points between each step. This dramatically reduces the number of single atom calculations, to the point that it becomes feasible to run the combined simulation code for a complete simulation along the whole length of a capillary.

For a laser pulse that changes very slowly between steps on length scales given by 10^4 total steps in the capillary the high harmonic generation also changes slowly. Within this limit, linear interpolation can be used to approximate the high harmonic generation terms between steps.

Linear interpolation is used as it requires that only the previous and current steps are known for it to be performed. This then helps to minimise the memory and computational requirements of the system running the code, allowing for faster computation times than when more complex interpolations are used.

The linear interpolation used within this model is given by the equation

$$S_l = S_{old} + l dS_l \tag{2.51}$$

where

$$dS_l = \frac{S_{current} - S_{old}}{l_{total}}. \tag{2.52}$$

Here S_l is the generated harmonic spectrum at the lth interpolation point between two steps, S_{old} is the harmonic spectrum at the previous step, dS_l is the approximated linear change in harmonic spectrum from the previous step to the current interpolation point, $S_{current}$ is the generated harmonic spectrum at the current step, and l_{total} is the total number of interpolation points between two steps.

One key advantage of this interpolation technique is that each interpolation point can be independently calculated. This allows for the implementation to take advantage of

multithreading, speeding up the computation time of the interpolations between two steps.

2.4 Combined Full Laser Propagation HHG Model

The implementation of this full capillary-based HHG model used a combination of the previous three models working together, discussed in Sections 2.1, 2.2, and 2.3. This short section briefly describes how these previously discussed models are used together to form the full model.

The spectral evolution of the laser pulse is performed using the technique as Section 2.1. Equation (2.18) is used to calculate the spectral evolution between each step, which gives the spectral amplitudes of the laser pulse at different positions throughout the capillary. These are then fed into the single atom response model to give the high harmonic source term due to the driving laser pulse at given radial and longitudinal positions in the capillary.

The high harmonic generation is calculated in two stages, firstly the electron acceleration due to the driving pulse is calculated using Eq. (2.34) of Section 2.2, then this electron acceleration is used in Eq. (2.35) to give the nonlinear polarisation and thus the high harmonic source term. Here the driving laser pulse can be an arbitrary pulse, and for each step and radial position of the capillary the driving laser pulse at that position is used to generate a high harmonic source term.

Using the angular spectrum method given by Eq. (2.37) of Section 2.3, and taking into account losses due to the complex refractive index of the gas, the high harmonics are then propagated from their generation positions to the end of the capillary. After each high harmonic is propagated to the capillary end they are combined together to give the harmonic spectrum as seen at the end of the capillary.

This then gives the full theoretical implementation of this combined, three-dimensional model, where the laser pulse propagates along the capillary, inducing high harmonic generation within the gas, from which the harmonics generated are propagated to the capillary end.

2.5 Conclusions

In this chapter an advanced model of capillary-based high harmonic generation and propagation has been presented. This model propagates driving laser pulses through gas-filled hollow capillaries, calculates single atom responses to arbitrary laser pulses through TDSE calculations, and propagates the resulting harmonic spectra to the end of

the capillary to give the resulting harmonic spectrum by using a modified ASM. Here the original model presented by P. Anderson has been both expanded and completed to form a complete and full model of capillary-based HHG. Amongst other things, this has transformed the model from only being able to facilitate the modelling of capillary-based HHG media of several mm in length to now being able to model HHG capillary-based media of multiple cm in length, at least an order of magnitude improvement.

This advanced and detail-producing generation model is used successfully throughout the rest of this work to investigate the harmonic generation throughout capillaries, as well as using the model constituent parts to investigate other simpler media too. We envision this advanced model will be used to improve capillary design and give insights into which laser sources to use for which capillary-HHG purposes or aims.

Chapter 3

Computational Implementation

This chapter describes the computational implementation of the numerical models for the capillary laser pulse propagation, laser-driven high harmonic generation, and high harmonic propagation models discussed in Chapter 2, as well as the implementation of combined laser-driven capillary-based high harmonic generation model. For each implementation, key parts are discussed, as are code-based improvements where appropriate, and finally a schematic overview and discussion of the associated algorithm and process is presented. Parts of the code were inherited from P. N. Anderson [12] and improved upon. These were for the capillary-based laser pulse propagation and also the high harmonic generation. Whilst these can be found within the same repository they were independent of each other and unconnected in terms of functionality.

The model-implemented codebase described within this chapter can be found at Ref [103]. Here the codebase is written in C++, with an object-orientated approach. For the results presented in the further chapters here they have been generated from running this code on the Iridis high performance computing (HPC) cluster at the University of Southampton. This codebase can also be compiled and run on personal computers too. Compilation and running using a Linux machine and a Mac laptop have been successfully performed, and whilst compilation and running on Windows is untested it should be possible, particularly with the use of Windows Subsystem for Linux [79].

The laser pulse propagation code on its own can be run on a personal computer efficiently due to its speed, and the harmonic generation code on its own can be ran on a personal computer if only a small number of harmonic-generation atoms are used. Running the combined code on a personal computer, however, quickly becomes impractical due to the computational power needed and so is ideally suited to HPCs.

3.1 Pulse Propagation Model Implementation

The laser pulse propagation as implemented in the codebase is the fastest part of the full capillary simulation, also running on a single thread. This code was inherited and originally could only perform laser pulse propagation in gas-filled hollow capillaries of constant pressure though this has since been improved. Below parts of the model implementation are discussed, as are improvements and an algorithmic overview of the process within the codebase.

3.1.1 Adaptive Step Size Laser Propagation

The laser pulse propagation is broken down into steps with the laser being propagated from the current step to each next step along the capillary successively. The positions of each step are defined by two user-given parameters, the length and the total number of steps within the capillary, with the position of each step being determined from the length over the number of steps.

In each propagation step a Runge-Kutta-Fehlberg 45 (RKF45) [38] ODE solver is used with an adaptive step size to solve for the spectral amplitudes, propagating them from their current position z to their new position $z + dz$, where dz is the size between each step. The RKF45 method is used with the spectral evolution equation, Eq. (2.18), to determine the relative numerical errors involved within the propagation from one step to the next so that the relative error can be kept within a user-specified tolerance. This relative error is determined by solving the spectral evolution equation using a fifth order and fourth order Runge-Kutta method and then comparing the two results to give the relative error of the fourth order method.

If the numerical error is outside the specified tolerance then the step size is reduced and the spectral evolution equation is solved for again, with the spectral amplitudes at position z instead being propagated to $z + h$ where $h < dz$. Once a step size h is found that propagates the spectral amplitudes with the desired tolerance, the propagation is performed. This is then done for next the position, $z + h$ to $z + 2h$, and is repeated until the end of the original step, $z + dz$, is reached with the desired tolerance.

During each of these propagation steps, a propagator is firstly applied to propagate the spectral amplitudes half the step size. Then a backwards spectral transform is applied to transform the amplitudes into the time and spatial domains. These are then used to calculate the spectral current density, which is then propagated the remaining half step to give the solved spectral evolution for that step. This is equivalent to how the time dependent Schrödinger equation is solved for in Equations (2.32) and (2.33). As mentioned previously, the spectral transform consists of a Hankel transform and a Fourier transform.

This whole process is repeated for each step along the capillary, stopping once the end of the capillary has been met.

3.1.2 Laser Pulse

Originally the code only supported starting with an initial Gaussian laser pulse at the beginning of the capillary. This has been improved so that now an arbitrary laser pulse can be read in from file instead, if desired. This results in any user-provided laser pulse now being able to be used as the initial starting pulse.

In conjunction with this, an improvement was made to allow a simulation to be started from any step along the capillary, provided the relevant laser pulse is supplied by the user. As discussed later in Section 3.4, this then gives the ability for the simulation to be split up into multiple concurrent sub-simulations.

3.1.3 Gas Pressure Profile

The initial code did not include a capillary gas pressure profile and instead used a constant gas pressure across the length of the capillary. This has been improved and the gas pressure profile discussed in Chapter 2 has been added into the code. This better represents the true profile encountered experimentally and so provides the simulations with a higher level of agreement to experiment. It is also relatively straight forward to define new pressure profiles inside the code, due to the way in which this improvement was implemented. For a new profile, the corresponding new gas pressure profile function needs to be programmed into the code, and then it can be selected through a configuration file parameter. This particular approach has been taken so that it is easy to switch between the two gas pressure profiles currently supported, and so that there is a reduced effort to add new profiles in the future if needed.

3.1.4 Capillary Modes and Radial Points

Within the laser pulse propagation implementation the number of capillary modes supported is user-specified. Whilst a low number of modes reduces computation time, the modal interactions are an important effect and so a sufficiently high number of modes needs to be included to capture this.

As a result of the Hankel transform implementation, the number of capillary modes also needs to equal the number of points along the radial grid of the capillary. This typically increases the number of modes further, firstly as a high number of radial points are needed to achieve an appropriate radial resolution when analysing results, and secondly as the combined model requires a large enough number of radial points for the

harmonic generation and propagation too. During the work presented within the further chapters here, the number of modes and radial points has been set to 158, which was found to be sufficient when tested.

3.1.5 Radial and Frequency Grids

There are three grids used within the laser pulse propagation, these being a radial grid, a time grid, and a laser frequency grid. The radial grid used has a non-linear spacing based on the zeros of the zero order Bessel function of the first kind.

The time and frequency grids are interconnected, with the time grid being N_t steps in length and linearly spaced between the user-specified minimum and maximum times in increments of dt. The frequency grid is also N_t steps in length however the values of each frequency within it are proportional to the inverse of the time step, dt.

A problem faced with the use of these grids was knowing the number of time steps needed for a frequency grid to be generated that encompassed the full range of laser frequencies included in a simulation. This was as the supported laser frequency range, the minimum and maximum time values, and the number of steps in the grids were independently user specified. The result of a user unknowingly setting one of these parameters to a value that resulted in the full range of frequencies not being contained within the frequency grid was that the simulation would not run and would instead crash during the initialisations stage. To solve this these time and frequency grids were changed so that at initialisation they expanded to fit the user-specified frequency range. This was done through iteratively increasing the steps within each grid, regenerating them, and checking whether the full frequency range was now contained. By increasing the number of steps in each grid, the spacing of the time grid, dt, decreases and the maximum frequency of the frequency grid increases.

3.1.6 General Code Improvements

The data from simulations is output to a collection of custom binary files, with the data being outputted for the real and imaginary parts of the laser pulse spectral amplitudes and the frequency grid of the laser pulse. Originally each of these files lacked any header information and just contained the data on its own. This proved troublesome when trying to read in the simulation data later on to perform postprocessing and analysis as the sizes and shapes of the arrays were unknown. To solve this, an early improvement to the codebase was to create a specific header for these binary files that gave the array shapes as well as some additional information. This then meant that these binary files could now be easily read in by scripts performing postprocessing

and analysis as the shapes and sizes of contained arrays did not now need to be known beforehand.

A configuration file implementation was also introduced into the codebase as prior to that all parameters within a simulation were hardcoded into the codebase. This configuration file approach then meant that parameters could now be set within a given specified file rather than having hardcoded values where code recompilation was needed whenever there was a parameter change. A large number of parameters can be set through the configuration file. These range from parameters such as the number of modes and radial points supported, to the parameters that define the laser pulse, to the gas pressure profile, the relative laser propagation error, the names of the output files, and the names of given input files, amongst other parameters.

The layout of the codebase has also been tidied up and put into a more logical structure, with code being shared between the models where possible. In addition to this, a CMake file has also been introduced to allow for easier compilation of the code and Doxygen [5] has also been employed for automatic documentation generation at compile time. This document generation is done via Doxygen analysing the source code and so helps to make it easier to understand the code layout, structure, and interdependencies.

Additionally, general improvements to the code have also be made. For example, class instances and variables that remain unmodified when passed into functions are now passed in through constant reference. This is firstly good practice and secondly can potentially reduce the code execution time, depending on whether this is already done automatically by compiler optimisations or not.

3.1.7 Libraries Used

Within the codebase for the laser pulse propagation model two external libraries have been used, the Intel Math Kernel Library (MKL) [58] and the Eigen library [51]. The Intel MKL library has been used for the Fourier transforms performed within the simulations and the Eigen library has been used for the arrays and matrices within the code as this library supports various array and matrix operations whilst also allowing for dynamic sizing of arrays and being computationally efficient.

3.1.8 Algorithm

A schematic overview of the laser pulse propagation algorithm is given in Figure 3.1.

In the first stage of a simulation the initialisations taken place. Here the configuration file is read in, class initialisations are performed, the driving laser pulse is defined

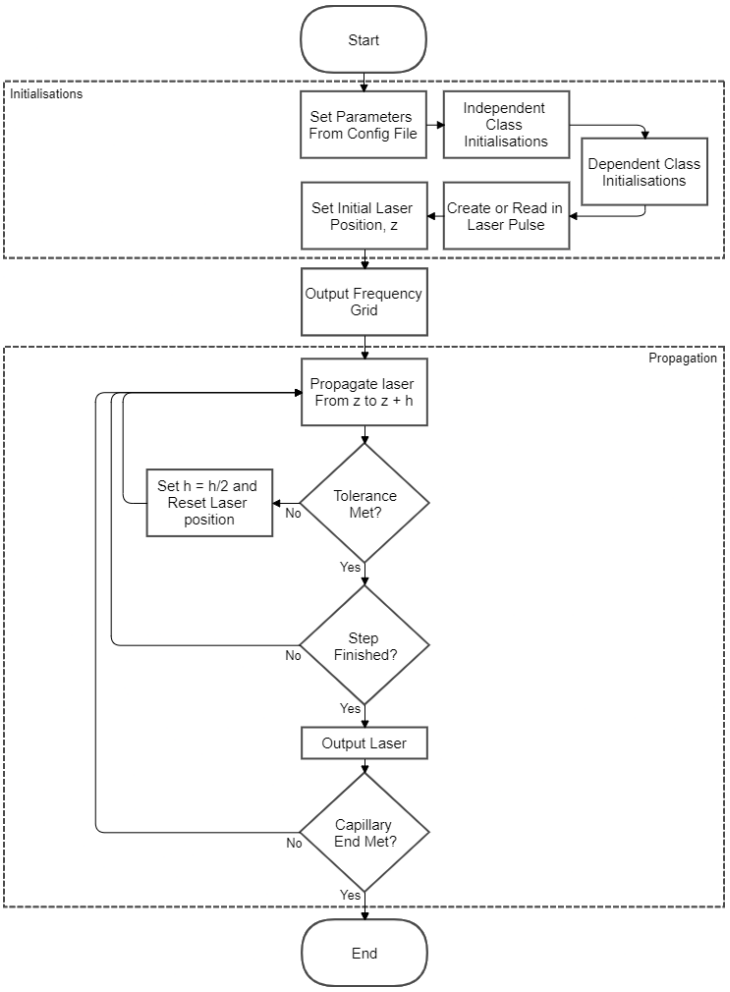

FIGURE 3.1: Schematic overview of the laser pulse propagation algorithm.

through either reading it in from file or using laser parameters given in the configuration file, and the starting position of the laser is set. The class initialisations are split into two parts, the first is for class instances that do not have a dependence on other class instances and the second is for those that do. The initial position of the laser corresponding to either the very start of the capillary if the laser is generated from the configuration file or an arbitrary position within the capillary if the laser pulse is read in. After that the laser frequency grid is outputted to file and then the propagation stage begins.

Within the laser pulse propagation stage of a simulation the laser is advanced to each successive step along the capillary by solving the right hand side of the spectral evolution equation Eq. (2.18) using the RKF45 method described above. Here the laser is propagated from z to $z + h$, where initially $h = \Delta z/5$. If the laser pulse propagation is found to be within the specified tolerance then the position of the laser is changed from z to $z + h$ and this process repeats. However if the pulse propagation is not found to be within the given tolerance then h is decreased to $h/2$ and this process is repeated with this new smaller h-value. This h-step propagation process repeats until the laser

reaches the end of the step $z + \delta z$ with the specified tolerance. At this point the laser pulse is then outputted to file and this whole process repeats until the end of the capillary is met. Once the capillary end is reached the laser pulse propagation has completed and so ends.

3.2 High Harmonic Generation Model Implementation

The high harmonic generation model as implemented in the codebase is the slowest part of the code, though it is highly parallelisable and so can take advantage of available cores and threads when run on high-core systems such as HPCs. This code was also inherited, but has been significantly improved. The model implementation into the code is discussed below, as are the improvements made to it and an algorithmic overview of the process.

3.2.1 Ground State Wavefunction

For the wavefunction at the initial time, the ground state needs to be known. To determine this a wavefunction seed is first made and then propagated in imaginary time with no laser field present [16]. By transforming to imaginary time the Schrödinger equation becomes a diffusion equation,

$$-\frac{\partial}{\partial \tau}\psi(x,\tau) = \hat{H}\psi(x,\tau), \tag{3.1}$$

where $t = -i\tau$. This has the solution

$$\psi(x,\tau) = e^{-\tau\hat{H}}\psi(x,0), \tag{3.2}$$

with

$$\psi(x,0) = \sum_i c_i\phi_i(x), \quad c_i = \langle \phi_i(x)|\psi(x,0)\rangle\,, \tag{3.3}$$

and $\phi(x)$ are the energy eigenstates of $\hat{H}$.

This gives rise to the time evolution equation

$$\psi(x,\tau) = e^{-\tau\hat{H}}\psi(x,0) = \sum_i e^{-\tau E_i}c_i\phi_i(x). \tag{3.4}$$

As time increases the wavefunction converges to the ground state,

$$\psi(x,\tau) \to e^{-\tau E_0}c_0\phi_0, \tag{3.5}$$

as the non-ground state exponentials decay more rapidly than the ground state exponential, and so for a large enough time the ground state can be obtained.

3.2.2 Wavefunction Evolution and Electron Acceleration

With the ground state determined, the laser field is applied and the wavefunction is propagated in real time. For this, at each time step the wavefunction is propagated to the next using the split step method given in Eq. (2.33). Here the kinetic energy terms of the propagator are solved in the spectral domain through fast Fourier transforms and the potential energy term is solved in the spatial domain.

Originally the electron dipole was determined from the wavefunction at each time step and outputted to file. This has since been changed so that the electron acceleration is calculated and outputted instead. For this the wavefunction at each time step is used to determine the electron acceleration using Eq. (2.34).

3.2.3 Driving Laser Pulse

Originally the laser pulse used was a Gaussian. This has been improved so that a user-supplied arbitrary pulse can now be read in from file and used instead if preferred. This then means that the electron acceleration due to an arbitrary laser pulse can be calculated, which is an essential part of the combined code discussed later.

The user-supplied laser pulse is given in terms of the laser modal spectral amplitudes and so within the code a Fourier transform is used convert it into radial temporal amplitudes. The user-supplied laser pulse is also typically on a much coarser grid than what is required for solving the TDSE and so it is also transformed onto a finer grid during the mentioned spectral to temporal Fourier transform by using a scale factor equal to the inverse of the number of time steps.

3.2.4 Radial and Frequency Grids

For each harmonic generation simulation, the HHG is calculated for atoms along the radial slice of the capillary. Multithreading is taken advantage of here to great effect, with each worker thread being given a small subset of the total harmonic-generating atoms to solve the TDSE for. This allows multiple laser-driven electron-atom systems to solved for and simulated at the same time.

The original radial grid used for this was linearly spaced though this has been changed to the nonlinear grid described in Section 3.1.5 so that the radial positions of the atoms within the high harmonic generation model corresponded to the radial positions of the

driving laser pulse within the laser pulse propagation model. This is so that the radial positions from each of these models correspond to the same radial positions for the combined model.

The improvements described in Section 3.1.5 for the frequency grids have also been implemented here in a similar way.

3.2.5 Libraries Used

The model implementation uses Intel MKL and the Eigen library again, with the first being for the fast Fourier transforms and the second for the dynamic arrays with supported linear algebra and vectorised mathematical operations. The Message Passing Interface (MPI) was also used for the multithreading, with OpenMPI [48] being the specific implementation used within the codebase. For multithreading on HPCs MPI has advantages over other multithreading methods such as OpenMP [31] as OpenMP is limited to communicating between threads on the same node, unless being used in conjunction with MPI, which reduces its usefulness when using multiple nodes on a HPC. This is a limitation MPI does not have, allowing it to scale more easily to multiple nodes.

3.2.6 General Code Improvements

The same general improvements described in Section 3.1.6 are also implemented: headers are included in the outputted binary files, a configuration file has been implemented, the codebase has been put in a more logical layout, a CMake file has been introduced, and there is now automatic documentation generation via Doxygen, amongst others.

3.2.7 Algorithm

A schematic overview of the high harmonic generation algorithm as implemented into the codebase is given in Figure 3.2.

In the first stage of a simulation, parameters are read in from the configuration file and the class instances are initialised, with class instances independent of others initialised first. The classes in the code are initialised across all the threads the simulation is using.

After this the work of the master and worker threads diverges. The master thread either reads in a laser pulse from a user-specified file or generates one based on the user-given configuration parameters. For a laser pulse read in from file, it is then transformed from modal and spectral to radial and temporal amplitudes, whilst also going from a coarse

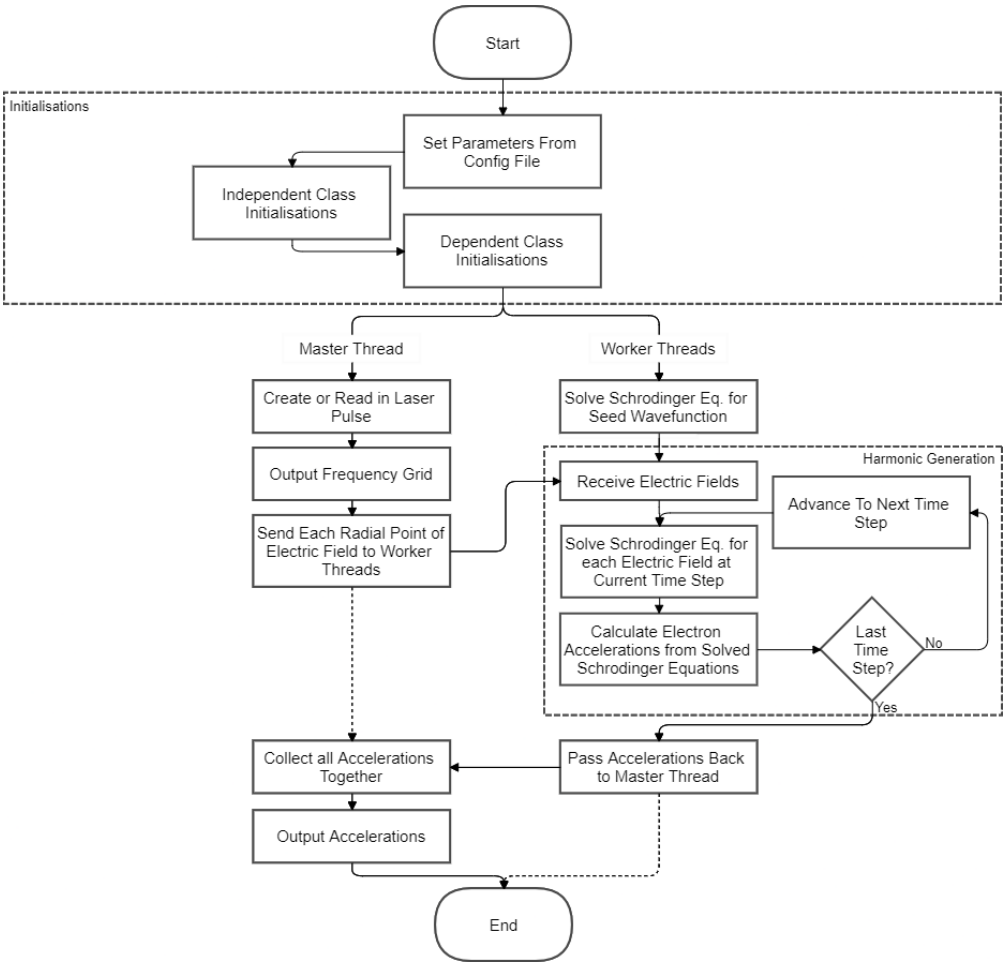

FIGURE 3.2: Schematic overview of the high harmonic generation algorithm.

to fine step size in time too. After this, the master thread then outputs the laser and harmonic frequency grids to file. As this is occurring the worker threads are instead all calculating the initial electron-atom ground state using the method described in Section 3.2.1.

The master thread then sends the laser electric field to the worker threads, with the laser field split up in terms of the time dependent field at each radial position. Here a configuration parameter determines how radial position electric fields are sent to each worker thread, and therefore how many laser-driven single electron-atom systems each worker thread solves for. The time-dependent Schrödinger equation for each of these is solved using Eq. (2.33) of Chapter 2. This is done by beginning at the initial start time with the ground state wavefunction stepping forwards in time with the laser field applied. The electron acceleration at each time step is calculated from Eq. (2.34) and stored. This process of stepping forwards in time continues until the last time step has been completed, at which point the worker threads pass the time-dependent electron accelerations back to the master thread. The master thread then collects these

all together and outputs them to file. After this the simulation has ended and so the program comes to an end.

3.3 High Harmonic Propagation Model Implementation

The computational implementation of the high harmonic propagation model sits between the laser pulse evolution and the harmonic generation models in terms of computational speed. Like the high harmonic generation implementation it can take advantage of multithreading and so becomes much faster when used in conjunction with multiple and threads. This code was a new development, again written in C++ and following the same design principles of the other codes.

Within this implementation of the harmonic propagation model the generated high harmonics are propagated to the end of the capillary and combined together to give the harmonic spectrum as seen at the end of the capillary. Both the generated high harmonics and the resulting end-of-capillary spectrum are given in terms of radial spectral amplitudes.

3.3.1 Refractive Index Interpolation

The real and complex parts of the atomic scattering factors used when calculating the refractive index for the high harmonics are read in from file, with the refractive index being calculated by Eq. (2.41) of Chapter 2.

These atomic scattering factors are given for different harmonic energies ranging from 10 eV to many thousands of eV, with a nonlinear spacing between the energies that does not correspond to the spacings of the harmonic energies as determined from the corresponding frequency grid within the simulation. As such, the real and complex parts of the atomic scattering factors are interpolated from their initial energy grid onto on that matches the energies resulting from the harmonic frequency grid used within the simulations. As mentioned in Chapter 2, this is done using an Akima cubic spline method, specifically from the implementation within Intel MKL.

Other interpolation methods within MKL either resulted in a lack of fine scale detail or discrepancies in the refractive index at energies where the scattering factors had rapid changes in value. Hence the Akima cubic spline method was chosen as it did not present these issues.

3.3.2 Gas and Gas Pressure Profile

The same gas pressure profile as that used in the laser pulse propagation model implementation was used here. As with the pulse propagation model, it was implemented in a way for it to be relatively straight forward to define new further profiles, with a function giving the new profile needing to be programmed in and then it being selected through a configuration parameter. As with the laser pulse propagation implementation, the two profiles currently supported are the capillary gas pressure profile discussed within this work and also the constant gas pressure profile.

When calculating the refractive index of the gas for the high harmonics, the piecewise functions of Eqs.(2.44)-(2.48) are used to calculate the atomic density as used within Eq. (2.41).

3.3.3 Libraries Used

The libraries used within this model implementation are again MKL, MPI, and the eigen library. MKL is used for the Fourier transform and the Akima cubic spline, MPI for the multithreading, and the Eigen library for the arrays and supported array operations.

3.3.4 Algorithm

A schematic overview of the algorithm implemented for the high harmonic propagation model is given in Figure 3.3.

As with the other model implementations, at the beginning of a simulation the configuration parameters are read in and set and then the class instances are initiated. During the class initialisations the atomic scattering factors are read in and interpolated to match the harmonic frequency grid. After these initialisations have been completed the harmonic frequency grid is outputted to file and then the propagation stage begins.

The radially dependent harmonic spectra from the first initial step are received and propagated to the end of the capillary using the ASM method of Eq. (2.37). The simulation then advances to the next step, with the harmonic spectra for this step being received and also propagated to the end of the capillary. An interpolation step now takes place, with the pre-propagated spectra of the current and previous steps being interpolated using Eqs.(2.51) and (2.52). After each interpolation the resulting spectra are also propagated to the end of the capillary. As the harmonic spectra are propagated to the end of the capillary they are combined together with the spectra already there. This process repeats until the final step along the capillary has been reached and completed, and the resulting radially dependent spectra are output to file.

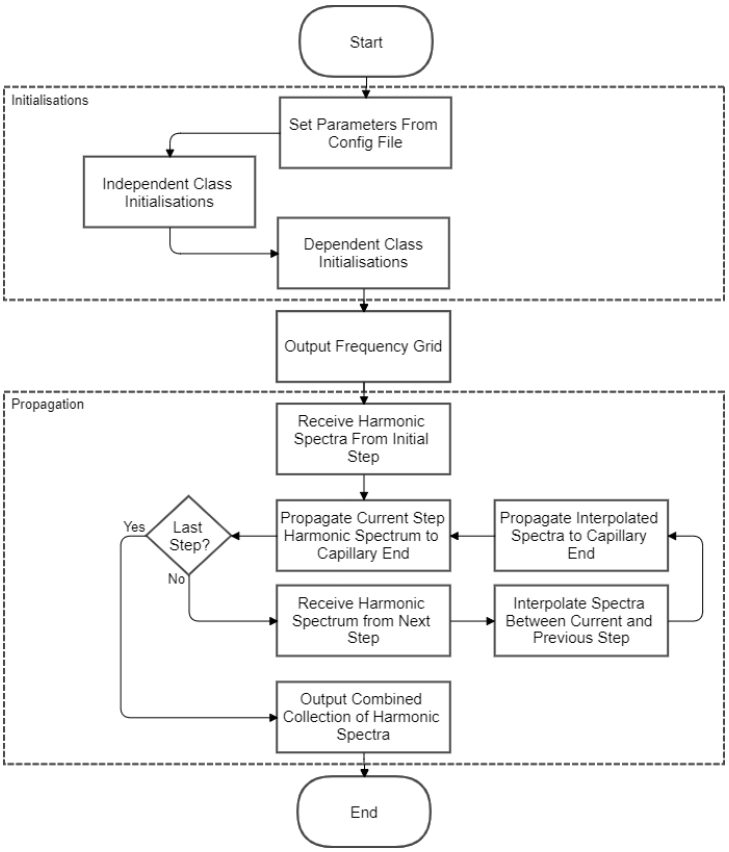

FIGURE 3.3: Schematic overview of the high harmonic propagation algorithm.

For simplicity, a single-threaded approach has been described here however in practice a multithreaded method is used. In the multithreaded approach the master thread receives the harmonic spectra for each step, determines how many interpolation steps are to be performed by each worker thread, sends the current and previous spectra to each of these as well as the information giving which interpolation steps a worker thread is to perform. Each worker thread then computes these interpolations, propagates them to the end of the capillary and passes these back to the master thread. During this, the master thread computes any leftover interpolations and propagates them, receives the spectra from the worker threads, combining them all together to give the complete harmonic spectrum as seen at the end of the capillary.

To determine the number of interpolation steps to be performed by all the threads, the total number of interpolations to be performed are divided by the number of worker threads. This gives the amount per each worker thread and then the remaining amount from this are those to be calculated on the master thread.

3.4 Combined Model Implementation

The combined model includes the previous three model implementations used together to form a state of the art advanced method for simulating laser-driven high harmonic generation and propagation within a gas-filled hollow capillary. Due to combining the previous three models together to form this, the combined model takes the longest time to run and so whilst it can in theory run on personal computers, a HPC is needed to achieve an appropriate level of detail.

3.4.1 Simulation Run Times

As discussed in the laser pulse propagation implementation, the driving pulse propagation implementation has been designed so that it can read in and use an arbitrary laser pulse from any given step along a simulation, enabling laser pulse propagation simulations to be split up into smaller parts that can be run concurrently. This is a crucial feature used within the combined model implementation.

For the full simulations that have been run to generate the results presented within this work, the laser pulse propagation is first run on its own on a coarse grid. This is done to quickly generate seed laser pulses. These seeds are then used within the full combined model as starting points for each of the mentioned concurrent simulations. For the full simulations performed to generate the results within this work, this approach worked to great effect, with a given capillary simulation being split into 30 parts and each being ran on the Iridis 5 HPC at the University of Southampton.

For these simulations a total of 15,000 steps were used along the laser propagation axis, with there also being 158 radial positions at each step. This resulted in 2.37 million laser-driven electron-atoms systems for the TDSE to solve. If the 30 split simulations were run consecutively this would take around 700 hours to complete, or just over 29 days, which is not a practical length of time. Instead, by splitting the simulations into these 30 parts, it took a little over two days to run on Iridis 5, depending on queue waiting times. This was also with a limitation present on the maximum number of computing nodes available to a single user at a given time, resulting in up to 15 of these split simulations being able to be ran simultaneously.

The result of all this is that a full simulation of the combined model becomes feasible with the length of time it takes to run when it is split into concurrent parts using the approach described here.

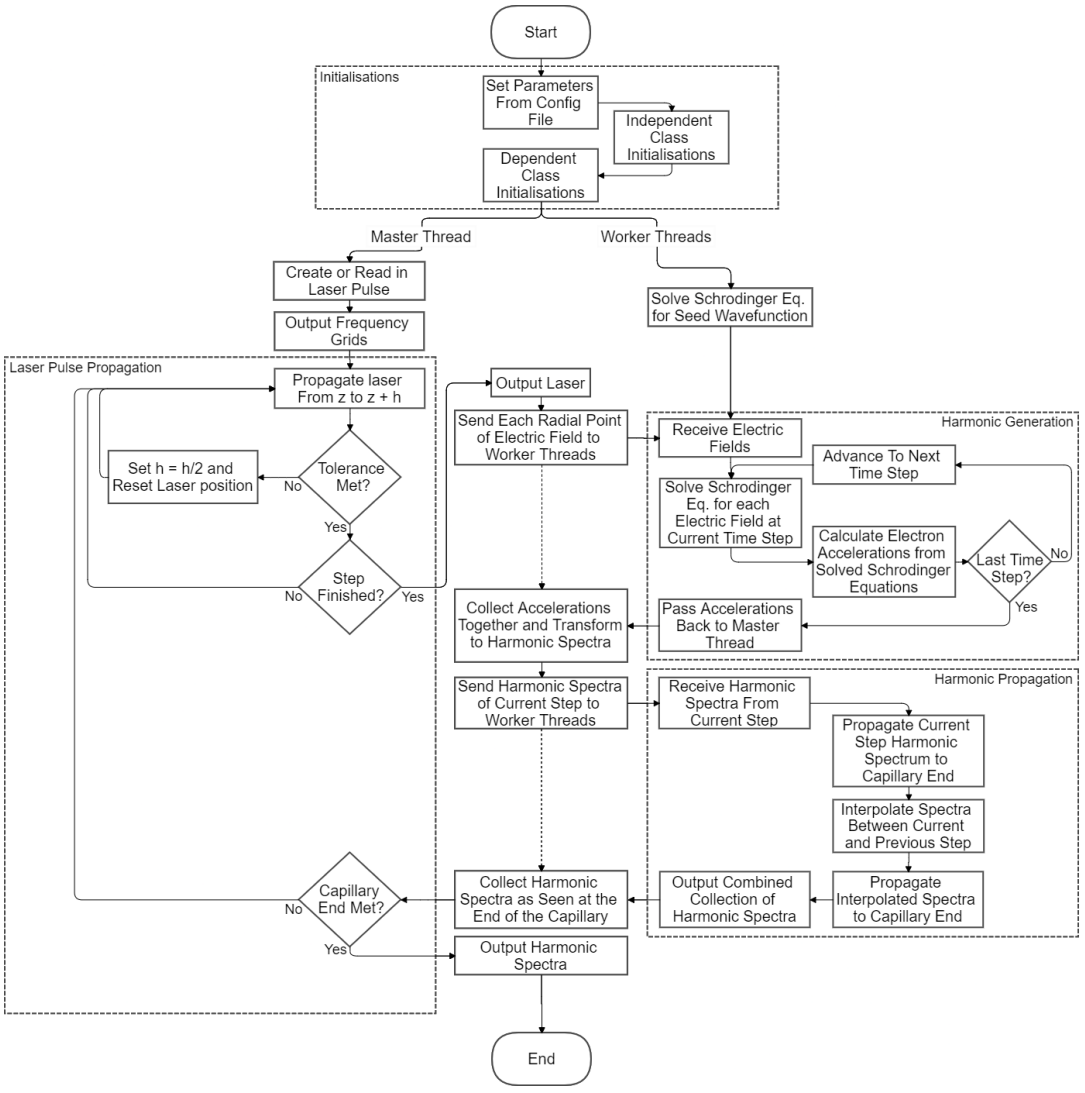

FIGURE 3.4: Schematic overview of the full capillary-based high harmonic generation algorithm.

3.4.2 Algorithm

A schematic overview of the combined capillary laser-drive harmonic generation and propagation algorithm is given in Figure 3.4. Here the algorithm given is for one single part of a simulation, so if a full simulation is split into, e.g., 30 parts then the algorithm here represents the process that occurs for each one of these individually.

Here the process again starts with setting parameters from a user-specified configuration file, followed by initiating class instances. During this stage the number of modes and radial points being supported are set automatically from the number of threads available to the given simulation. These are determined from $N = (N_{threads} - 1) \times N_{atoms\_per\_worker}$, where N is either the number of modes or radial points, $N_{threads}$ is the number of threads available to the simulation, and $N_{atoms\_per\_worker}$ are the number of

electron-atom systems to be solved for by each worker thread at each step along the capillary.

After this, the master and worker threads diverge in their tasks. On the master thread the laser pulse is either read in from file or defined by configuration parameters and then the frequency grids for the laser pulse, generated harmonic, and propagated harmonics are outputted to file. As this is occurring, on the worker threads the ground state of the electron-atom systems are determined.

The laser pulse propagation then begins, with the adaptive step size method being performed until the end of the step along the capillary is reached. At this point the laser spectral amplitudes are outputted to file and then the laser fields at each radial point are sent to the worker threads.

Here each worker thread receives their corresponding laser electric fields and then calculates the resulting time dependent electron wavefunctions and accelerations, with the process continuing until the final time step has been completed. After this the electron accelerations are passed back to the master thread.

On the master thread the time and radially dependent electron accelerations are collected together and the resulting harmonic spectra are gained from them using Eq. (2.35). These are then used within the harmonic propagation and interpolation stage.

Here the harmonic spectra are propagated to the end of the capillary and collected together into a separate internal variable. If the simulation is currently on its first step then the interpolation stage is skipped as there is no previous step or corresponding harmonic spectra to be used within it. For the second step of the simulation onwards, each worker thread is given the current and previous harmonic spectra and also information relating to the interpolations to be calculated. These are then determined whilst the master thread calculates any remainder interpolations. Each interpolation is also propagated to the end of the capillary, and once each worker thread has completed its assigned work the propagated harmonics are passed back to the master thread. These are then collected together and combined with those from previous steps.

The laser pulse propagation then moves onto the next step along the capillary and this whole process repeats. This is done until the end of the capillary is reached. Once at the end of the capillary, the resulting harmonic spectrum, as it would be seen at the capillary end, is outputted to file and the simulation ends.

3.5 Conclusions

An overview and description of the algorithm and implementation of the state of the art laser-driven capillary harmonic generation and propagation model used within this

work is given. This algorithm and implementation has been employed successively throughout the rest of this work to generate various harmonic spectra. It is envisioned that this model and implementation will be used to better understand effects within capillary-based high harmonic generation and to improve or optimise various harmonic generation properties such as increases to the generated energies or the clarity of resulting harmonics.

Chapter 4

Validation

4.1 Introduction

In this chapter three different components of the capillary-based high harmonic generation model as discussed in Chapters 2 and 3 are investigated to gain results that are then compared to those from the literature or other developed models. We first compare three laser spectra from our laser propagation model to results from Chapman et al. [25]. Then we compare single atom harmonic spectra from our 1D harmonic generation model to those gained from using the 3D model of Patchkovskii et al. [83]. Finally we compare a harmonic spectrum generated from our full capillary-based HHG model to an experimentally gained spectrum from Butcher et al. [24].

4.2 Laser Pulse Propagation

The capillary laser pulse propagation model presented and implemented in Chapters 2 and 3 is used to propagate an initial spatially and temporally Gaussian laser pulse optimally coupled into a hollow capillary filled with argon of 200 mbar gas pressure. Here three laser pulses have been simulated with average powers of 0.5 W, 0.6 W, and 0.8 W. Each is centred at 790 nm wavelength, with a full width at half maximum of 40 fs, a repetition rate of 1000 Hz, and a 48 μm waist for optimal coupling into the EH_{11} mode of the capillary with a 75 μm radius. The laser spectra as seen at the end of the capillary are given in Figure 4.1.

Here it is seen that as the laser power is increased the pulse experiences an increased amount of blueshift and nonlinear distortion. We see comparable behaviour between these spectra and the experimental and numerical laser spectra results found within the work of Chapman et al. [25], with both sets of laser spectra having increased blueshift for increased laser power, and with peaks occurring at the same wavelengths. For the

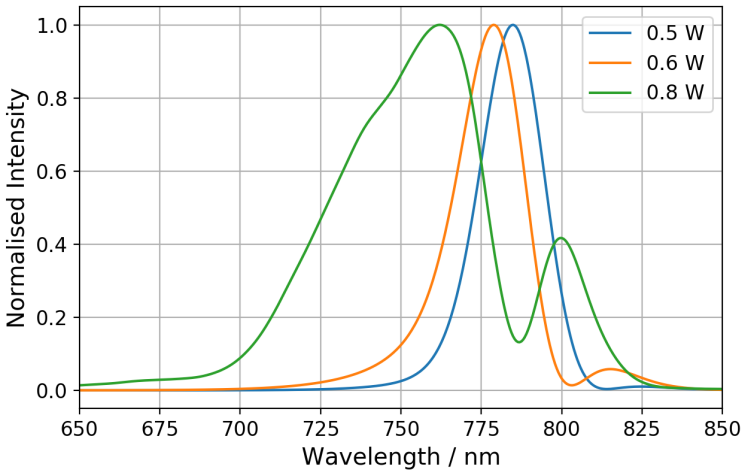

FIGURE 4.1: A 790 nm wavelength, 40 fs FWHM, 1000 Hz repetition rate laser with three different powers, 0.5, 0.6, and 0.8 W, with a 48 μm waist for optimal coupling into the fundamental mode of a capillary with radius 75 μm and filled with 200 mbar argon gas.

laser spectrum resulting from the 0.8 W average power laser there are peaks at around 760 and 800 nm for both results, with the secondary peak at 800 nm being a little under half intensity of the main peak in both cases, showing good agreement. The results of the 0.5 and 0.6 W laser powers are also comparable between our model and the results of Chapman et al., with the 0.5 W result being largely unchanged in both cases and the 0.6 W result undergoing small amounts of blueshift and starting to form a secondary peak at around 815 nm.

4.3 Single Atom Harmonic Spectra

Single atom harmonic spectra have been generated for four different laser systems using our single atom response model discussed in Chapters 2 and 3 and also using the three-dimensional model presented by Patchkovskii et al. [83], where this 3D model numerically solves the time-dependent Schrödinger equation in spherical coordinates for a laser pulse interacting with a one-electron atom system. The laser parameters for each modelled system are given in Table 4.1. Here a range of laser parameters have been used, such as driving wavelengths from 800 to 2000 nm and full widths at half maximums from 100 to 7 fs. For each, the driving pulse is Gaussian both spatially and temporally, with a waist of 48 μm.

The harmonic spectra gained from using the Ti:Sapph laser system for the 1D and 3D models are given in Figure 4.2. The harmonic spectra from the two different models match well. Here the harmonic intensity of the 3D result has had a constant scaling factor applied equally across harmonic energies to shift the maximum harmonic intensity to a value of 1.0, and the 1D result has had a different constant scaling factor

Laser System	Wavelength / nm	Average Energy / mj	FWHM / fs	Rep Rate / kHz
Ti:Sapph	800	1.0	50	1
Yb-fibre	1050	1.0	7	100
Mid-IR OPCPA	1700	0.17	50	100
Tm-fibre	2000	0.4	100	11

TABLE 4.1: A table giving the parameters of the four different laser systems used when comparing the single atom spectra generated using our 1D as discussed in Chapters 2 and 3 and the 3D model presented by Patchkovskii et al. [83].

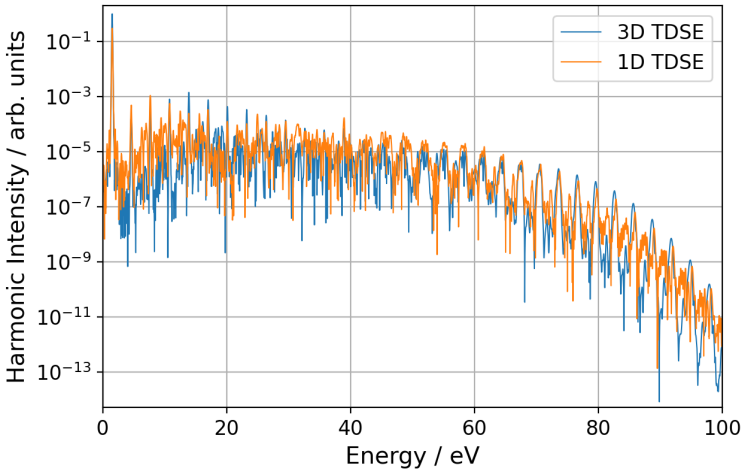

FIGURE 4.2: Single atom harmonic spectrum generated using the Ti:Sapph laser system for (blue) the 3D single atom model of Patchkovskii et al. [83] and (orange) our 1D single atom model discussed in Chapters 2 and 3.

also applied equally across harmonic energies to shift the harmonic intensity to that of the 3D spectra. Both have the cutoff at the same harmonic energies, both have peaks in harmonic intensities that correspond to odd harmonics of the driving laser pulse, and both having similar relative changes in their harmonic intensities over the range of the figure, from the perturbative region to the harmonic plateau and finally to the cutoff. However there are also differences too. The main difference is that the harmonic spectrum generated from our 1D model has increased amounts of harmonic generation between the odd harmonics of the driving laser which are not seen in the spectrum generated from 3D model. Despite this, for this laser system the harmonic spectra match well between the two models and therefore the 1D model is appropriate to use for driving laser systems with similar parameters to the Ti:Sapph system used here.

The harmonic spectra gained from using the Yb-fibre laser system for the 1D and 3D models are given in Figure 4.3 for the range of harmonic energies $0 - 100$ eV, with constant scaling factors across the harmonic energy again being applied to the harmonic intensities. Firstly, The classical cutoff is calculated to be 872 eV however our range is $0 - 100$ eV as within our work presented throughout we were only considering harmonic energies below 100 eV, particularly in the $16 - 45$ eV range. We find that over

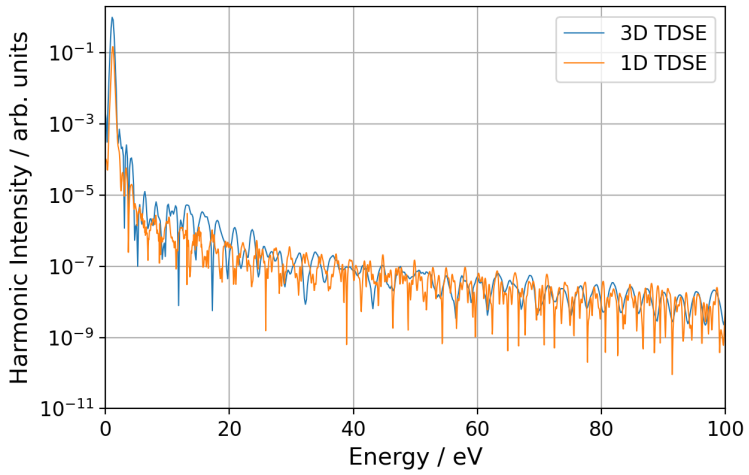

FIGURE 4.3: Single atom harmonic spectrum generated using the laser of the Yb-fibre laser system for (blue) the 3D single atom model of Patchkovskii et al. [83] and (orange) our 1D single atom model discussed in Chapters 2 and 3.

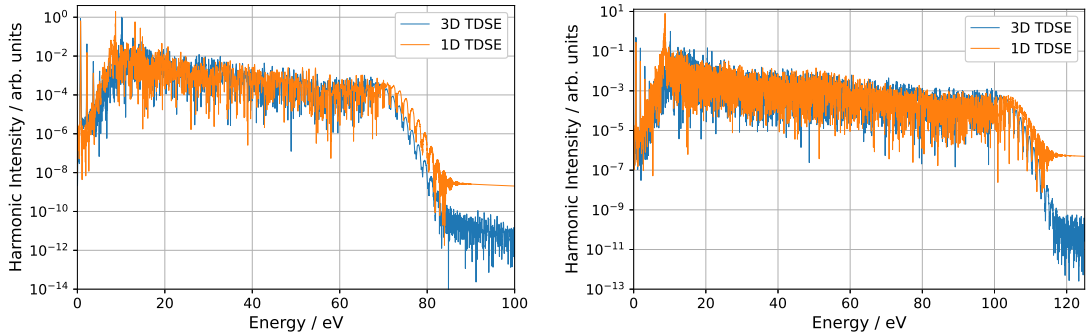

FIGURE 4.4: Single atom harmonic spectrum generated using the laser of the Mid-IR OPCPA and Tm-fibre laser systems for (blue) the 3D single atom model of Patchkovskii et al. [83] and (orange) our 1D single atom model discussed in Chapters 2 and 3.

this energy range the relative changes in harmonic intensities for the two models match well. At lower energies there are some differences in peak positions for the 1D model compared to the 3D model. At higher energies the local peaks match between the spectra of the two models. In general the 1D spectrum shows finer features, which could be due to the reduced quantum diffusion within it, as discussed later in Chapter 5, leading to sharper interference features between electron trajectories. Therefore, when considering the $0 - 100$ eV energy range our 1D model produces a comparable spectra for the 7 fs Yb-fibre laser and so can be used.

The harmonic spectra gained from using the Mid-IR OPCPA and Tm-fibre laser systems for the 1D and 3D models are given in Figure 4.4, also with constant scaling factors applied on the harmonic intensities across the harmonic energy. For both laser systems, the spectra generated match well between the 1D and 3D models. The Mid-IR OPCPA system gives a classical cutoff of 69 eV and the Tm-fibre a classical cutoff of 102 eV. The

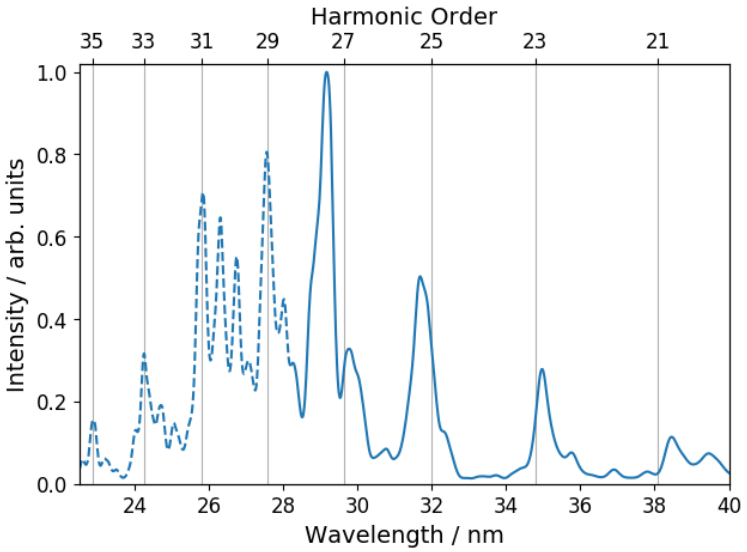

FIGURE 4.5: A high harmonic spectrum generated from using our capillary-based HHG model discussed in Chapters 2 and 3 for a 7 cm long capillary with 150 mbar gas pressure and a 48 μm waist driving laser pulse optimally coupled into the fundamental capillary mode. The laser pulse is initial spatially and temporally Gaussian, centred on 800 nm, with a FWHM of 50 fs, a repetition rate of 1000 Hz, and an average power of 1 W. Here wavelengths smaller than 28 nm have been plotted with a dotted line as in practice these would have smaller intensities than seen from our model as these wavelengths are suppressed due to the Cooper minimum which is an effect not captured by our model.

spectra from both systems do start decreasing in intensity at around these energies, as expected. However the spectra from the 1D model start to decrease at a very slightly higher energy than for the 3D model and, as a difference in the numerical noise floor, the 3D model decreases to smaller intensities than those for the 1D model. For both laser systems, the shapes of the spectra resulting from the 1D and 3D models match well across all energy ranges below the cutoff, with the relative changes in harmonic intensities closely matching too. Therefore, for laser systems with similar parameters to the Mid-IR OPCPA and Tm-fibre systems here our 1D model is appropriate to use when modelling HHG.

4.4 Capillary Spectrum

A harmonic spectrum has been generated using our capillary-based model and is given in Figure 4.5. This has been gained from using an initial laser pulse that is Gaussian spatially and temporally and has an 800 nm centred wavelength, a 50 fs FWHM, a 1000 Hz repetition rate, a 1 W average power, and a waist of 48 μm that achieves optimal coupling into the fundamental capillary mode. The capillary modelled for this was of 7 cm in length, filled with 150 mbar argon gas, and had a radius of 75 μm.

The capillary harmonic spectrum produced here can be qualitatively compared to that found within the work of Butcher et al. [24]. Within their work slightly different laser parameters have been used, with there being an initial 790 nm wavelength laser pulse with a FWHM of 53 fs, a repetition rate of 1000 Hz, and 0.81 W average power. Their laser has also been optimally coupled into the fundamental mode of a 7 cm radius capillary filled with 150 mbar argon gas through having a waist of 48 μm. These are slightly different to the laser parameters we used, with the largest difference being in the average laser power, and so some differences between the spectra produced are expected. However, these parameters are still similar enough that it is also expected both driving lasers will produce similar enough spectra such that they can be compared to each other. The part of the generated spectrum that has been plotted with a dotted line represents the part that would have a reduced intensity due to the effects of the Cooper minimum, a prominent minimum in the HHG spectra centred around 53 eV for argon [56, 118]. The reason why it does not here is that our 1D model does not include these effects, and so when comparing results between this model and experimental results this needs to be kept in mind.

Our spectrum in Figure 4.5 contains a number of peaks, with the majority being at energies which correspond to odd harmonic orders of the driving pulse. We do also see additional peaks between the 29th and 31st harmonics and also an additional small peak before the 21st harmonic. The corresponding spectrum from Butcher et al. has 5 peaks over the same harmonic wavelength range, with these at similar wavelengths to our 27th, 29th, 25th, and 23rd harmonics, plus the additional harmonic just past the 21st harmonic. Comparing our spectrum to that within Butcher et al., for the 27th, 23rd, and 21st harmonics we see similar relative differences between their harmonic intensities. However, we also see an underestimation in the intensity of the 25th harmonic for our result. This difference is not large though and could just be due to the higher driving power used in our simulation. For the harmonics at greater orders than the 27th, or smaller wavelengths than 28 nm, we find Butcher et al. to have much smaller intensities. This is due to the Cooper minimum being present experimentally though not being included in our model. This is a limitation of the model however and so long as it is kept in mind when using our model for HHG simulations it is not an issue and so comparisons and insights can still be made. Overall, we produce a similar spectrum when using a relatively similar set of laser parameters, showing that our model can reasonably simulate and model capillary-based high harmonic generation.

4.5 Conclusions

Here we have compared component parts our capillary-based laser driven HHG model to either results found in the literature or to other models. We have shown that our laser pulse propagation model behaves as would be expected, that our 1D single atom HHG

model produces spectra comparable to those gained from a more complex and time consuming 3D model, and have shown that our full capillary HHG model can produce similar spectra to those found within the literature. These all show that our capillary-based high harmonic generation model presented here is an appropriate and accurate tool to use when modelling capillary-based HHG.

Chapter 5

Pump-Wavelength Dependence of HHG

5.1 Introduction

The driving wavelength of a laser pulse used in high harmonic generation has a large effect on the high harmonics produced. Firstly, the wavelength dictates the position of the cutoff and thus the maximum energy of the harmonics produced, as shown in Eqs. (2.27) and (2.28) of Chapter 2. Secondly, through dictating this maximum energy it also dictates the width of the harmonic plateau and therefore also has an impact on the harmonic intensities within this region too. By choosing appropriate driving wavelengths, systems can be optimised for higher energy harmonics or higher intensity harmonics depending on the requirements of the target application.

Alongside this, the generation geometry can have a large effect too. A gas jet used as the generation medium has a short interaction length, reducing the coherent build up of the harmonics. However it also leaves the driving pulse largely undistorted by its propagation, keeping the harmonics generating at the same energies due to their energies being dictated by the mostly unchanged wavelength of the driving pulse, which results in clear harmonic structure to overall generated spectrum as the harmonics from the different generating atoms build up together. Contrary to this, a gas-filled hollow capillary has a much longer interaction length allowing for better coherent build-up of harmonics though also resulting in increased distortion of the laser pulse as it propagates through the capillary, impacting the harmonic structure.

When assuming all other parameters are kept constant, a useful metric for determining how the driving wavelength affects the harmonic generation is the efficiency, as determined from an integration over the generated harmonic intensities for a given range of harmonic energies. Through determining this efficiency for varying driving

wavelengths, the high harmonic generation dependence on pump-wavelength can be determined.

Here we investigate that pump-wavelength dependent high harmonic generation efficiency for three different geometries. These are a single atom at the centre of a laser beam, a thin sheet of atoms across the laser beam that sample the transverse intensity profile of the laser and are thin enough that propagation effects can be ignored, and a gas-filled hollow capillary with the laser propagating through it and interacting with many atoms. These geometries are discussed in further detail below.

5.2 Background

In the literature a simple power law has often been assumed for the scaling of the generated harmonic intensity I_h with the driving laser wavelength,

$$I_h \propto \lambda^x \tag{5.1}$$

where the scaling factor x was obtained by fitting Eq. (5.1) to experimental or simulated data. Due to the effects of quantum diffusion [67] a value of $x = -3$ was originally expected. In quantum diffusion, the part of the electron wave packet in the continuum spreads out with time. Assuming that this time-dependent electron wave packet is Gaussian, for each spatial dimension the resulting electron probability waist has a linear dependence on the return time of the electron wave packet, shown by [84]

$$|\psi(x,t)|^2 = \frac{a}{\sqrt{a^2 + (\hbar t/m)^2}} \exp\left(-\frac{ax^2}{a^2 + (\hbar t/m)^2}\right) \tag{5.2}$$

where a is the initial waist and $\frac{\sqrt{a^2+(\hbar t/m)^2}}{a}$ is the waist after a return time t. As the return time is inversely proportional to the pump-wavelength, for each spatial dimension the wave packet waist spreading, and therefore the quantum diffusion, has an inverse dependence on the pump-wavelength. For quantum diffusion in the planes transverse to the laser pulse this reduces the probability of recombination and in the plane longitudinal to the laser pulse it increases the spread of electron energies and thus reduces their intensities [62]. From this, quantum diffusion gives rise to a λ^{-1} dependence on the generated harmonic intensities for each spatial dimension, resulting in a λ^{-3} dependence when considering all three spatial dimensions.

First experiments suggested that rather than scaling with λ^{-3} the HHG efficiency instead scaled with $\lambda^{-6.5}$ [104] while theoretical models predicted scaling with $\lambda^{-4.7}$ to λ^{-6} [37, 41, 42, 59, 100, 101, 111]. The reason for this stark difference to the originally expected λ^{-3} is that the pump-wavelength affects HHG in many more ways than just the time an electron spends in the continuum before recombination. As discussed by

Falcão-Filho et al. [37] a λ^{-1} factor results from the energy carried by a cycle of the driving pulse scaling with its duration, another λ^{-1} results when considering a single harmonic due to the bandwidth, and finally an additional factor of λ^{-1} results when the harmonic under consideration is generated within the harmonic plateau as opposed to at the cutoff, which is related to the temporal spreading of harmonic frequencies during emission. The mentioned previous theoretical investigations were based on high harmonic spectra generated by single atoms and so do not reflect realistic experimental geometries where typically a laser beam passes through a cloud of atoms and harmonics are generated simultaneously by many atoms located at different positions within the beam and therefore experiencing different laser intensities.

The efficiency of high harmonic generation therefore depends strongly on the wavelength of the driving laser. A detailed understanding of this dependence is required for the design of new experiments which could be based on a large variety of current state-of-the-art ultrashort-pulse laser systems emitting wavelengths from the UV to the mid-IR. Several effects have been identified that contribute to the strong wavelength dependence of HHG.

The classical cut-off energy, defined by Eq. (2.27), gives the classically calculated maximum energy of the generated high harmonic photons and the position at which the harmonic plateau sharply drops off. This classical maximum energy has a λ^2 dependence, meaning that higher order energy harmonics can be generated using longer pump wavelengths. The efficiency of HHG is therefore extremely sensitive to pump wavelengths around the cutoff and beyond. On the other hand, within the plateau region of HHG, i.e. for harmonic energies below the cutoff, a longer driving wavelength is expected to result in smaller harmonic intensities due to the increased effects of quantum diffusion for the electron trajectories within the plateau that recombine with the atom after several optical cycles [113].

5.3 Experimental Geometry

As mentioned, we investigate the HHG efficiency scaling with driving wavelength for the single atom, the sheet of atom, and the gas-filled hollow capillary geometries. These geometries are shown in Figure 5.1. Here the single atom is taken from the on-axis atom of the sheet of atoms, and the sheet of atoms is taken as the first sheet of atoms within the capillary. Therefore, all three geometries can be modelled by just modelling the gas-filled hollow capillary geometry, as discussed in Chapters 2 and 3.

The choice of experimental geometry is expected to affect the high harmonic generation generation scaling efficiency. When a laser pulse passes through a thin sheet of atoms or a gas jet, atoms experience different laser intensities because of the transverse laser beam profile but all atoms will experience a similar pulse in time as the temporal

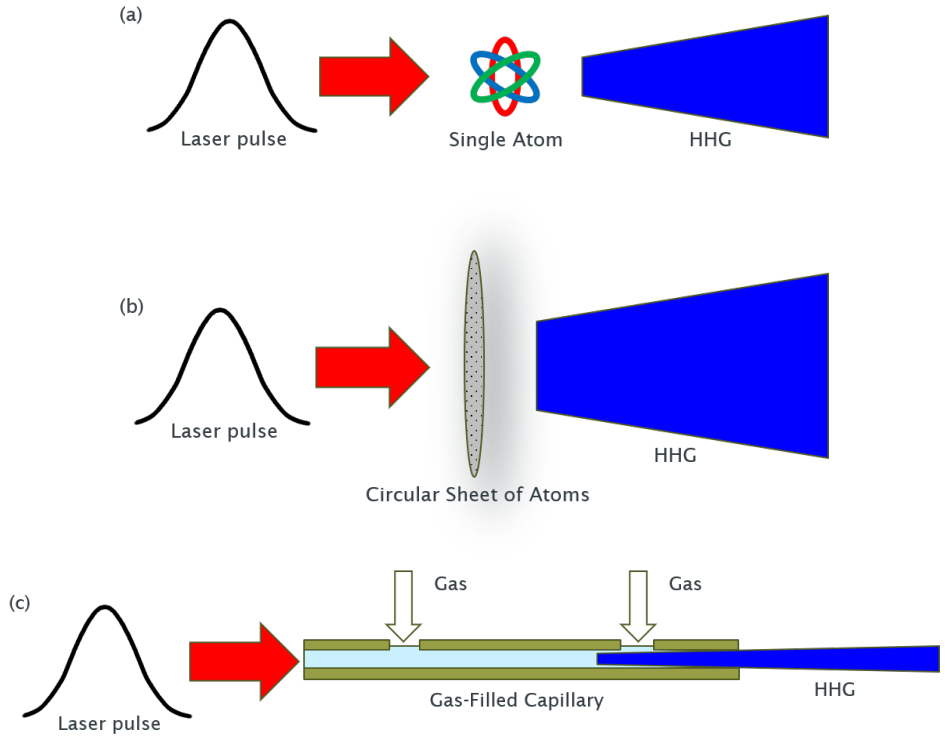

FIGURE 5.1: Geometries modelled, (a) single atom, (b) sheet of atoms, and (c) a gas-filled hollow capillary.

shape of the laser does not change significantly during propagation through the short distance of the sheet or jet. As an alternative, gas-filled capillaries or hollow-core optical fibres are being investigated as they can provide much longer interaction lengths and by controlling phase-matching between pump wave and generated harmonic allow for coherent build up and significant enhancement of HHG in a compact geometry [94, 17, 49, 24]. In such a system, however, the laser pulse undergoes nonlinear distortion due to its interaction with the gas as it propagates. Therefore, different atoms within the capillary also experience differently shaped laser pulses in time. This, along with phase matching effects and a build up of the harmonics as they propagate from their generation position to the end of the capillary, means that we should expect a different scaling of HHG efficiency than for the cases of a sheet of atoms or a single atom.

5.4 Comparisons Between Numerical Models

A factor to consider with numerical models and simulations is the dimensionality of the electron-atom system being modelled. For instance, the effects of quantum diffusion result in a λ^{-1} factor for each spatial dimension being included [67]. Therefore for

a one-dimensional atom being modelled the system will only include quantum diffusion effects of a λ^{-1} term but a model including all three spatial dimensions will instead result in the full λ^{-3} quantum diffusion term being included. Therefore if there is a reduced dimensionality within the numerical model being used then a reduced quantum diffusion term is to be expected.

Here we use the model discussed in chapters 2 and 3 and so employ one-dimensional electron-atom systems. Full three-dimensional single models have been developed for single atoms [83] and media such as gas jets and very short capillaries [47, 61] however these require significantly more computing power than one-dimensional models and so when simulating the many laser-atom interactions within our sheet of atoms and gas-filled capillary geometries these become infeasible. Whilst such three-dimensional simulations can take a handful of minutes for low power, very few cycle pulses, their computation times rapidly increase for higher powers and more optical cycles, which are the regimes under consideration here. For instance, the three-dimensional model found within Ref [83] can take a few days to run for a single atom calculation when using typical parameters considered in this chapter whereas our one-dimensional model instead takes a few minutes for those same parameters. This quickly results in the 3D model becoming infeasible for the macroscopic media under consideration here. Therefore to perform these simulations for macroscopic media with their longer interaction lengths and increased number of atoms the computational complexity needs to be reduced. However, by reducing simulation dimensionality approximations are introduced, though similar spectra and results are still produced, as discussed in Chapter 4.

Other considerations between models are the shape of the potential used and the ionisation levels. For instance, one-dimensional models overestimate the ionisation, particularly those using the soft Coulomb potential. This is due to the larger tunnelling rate within 1D models, caused by the much larger fundamental mode compared to the 3D fundamental mode. The result of this is that in 3D models the wavefunction is very much centred on the centre of the potential whereas in 1D models the wavefunction is much more spread out and so when a laser is applied more ionisation occurs as the wavefunction is already further away from the core. Despite this however, the shapes of the harmonic spectra produced from these models are in good agreement with those of equivalent three-dimensional models and hence one-dimensional soft Coulomb models can still be used to give useful insight.

5.5 Computational Running

For the simulations performed within this chapter, the models and implementation of Chapters 2 and 3 were employed. Here 158 radial positions and 15,000 steps along

the capillary were used. Between each step the single atom responses are interpolated onto an additional 10,000 steps and propagated to the capillary end. Simulations used 80 CPU cores, and the full simulation of capillary-based HHG for one set of parameters took a little over two days on the Southampton HPC cluster Iridis 5.

Through assuming circular symmetry, the sheet of atoms simulations are run for just a radial slice across the sheet, with each position on the radius being its own single atom calculation. From performing the sheet of atoms simulations, those for the single atoms can be gained at the same time too as these are taken as the on-axis atom from the sheet. Here each sheet is calculated by radially integrating across all radial positions. These are run independently from the capillary simulations to reduce the computation time as they do not require the capillary laser pulse propagation component. For the sheet of atoms and the single atom the driving laser pulse has a Gaussian profile, both temporally and spatially. For the capillary simulations, the harmonic spectra that have been propagated to and collected at the end of the capillary are also radially integrated over all simulated radiating atoms to give the expected output of the high harmonic source.

5.6 Results

The wavelength dependence of high harmonic generation for the three different geometries mentioned before is being investigated: a single atom, a thin sheet of atoms, and a gas-filled capillary. For the single atom and the sheet of atoms driving laser wavelengths from 400 - 1800 nm were simulated in intervals of 5 nm. Capillary simulations are much more time consuming even on a high-performance computing cluster and therefore a coarser 100 nm driving wavelength spacing was chosen, as was a more limited wavelength range of 800 - 1500 nm. Whilst the one-dimensional single atom model introduces approximations, sensible comparisons of the HHG between the different geometries are still made as the approximations of the model are present in the same way in all of the geometries and so their effects are removed when these comparisons are made. The single atom model though reaches its limit for the longest driving wavelengths and highest pump energies used in our analysis as the maximum electron displacement becomes comparable to the inter-atom distance. The results presented here also do not have the constant scaling applied that was previously seen for the single atom spectra in Chapter 4.

The pump-laser pulses used within this work had wavelengths varying from 400 to 1800 nm. All had 50 fs pulse widths, 1000 Hz repetition rates, 1 W average powers, 3.7×10^{14} W cm^{-2} peak intensities, and waists of 48 μm.

5.6.1 Single Atom HHG

Let us first consider the simplest case of HHG from a single atom which already highlights the most important aspects that govern the efficiency of HHG also for more complex systems. Figure 5.2 shows the harmonic spectra produced from a single atom driven by 50 fs, 1 mJ laser pulses (average laser power of 1 W at a repetition rate of 1 kHz) at 400 nm and 800 nm wavelength, respectively. Here the harmonic intensity is plotted against the photon energy of the generated harmonics and the classical cutoff, previously given in Eq. (2.27), for the two cases is indicated by the two dashed lines. Both spectra show the typical plateau of constant harmonic intensity and, beyond the cutoff, a rapid drop in intensity with longer pump wavelength.

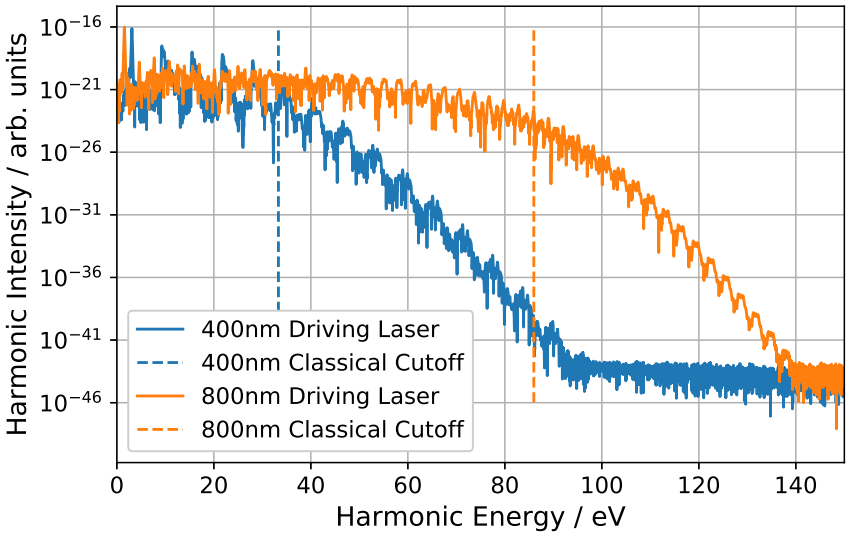

FIGURE 5.2: Single atom harmonic spectra for argon using a 400 and 800 nm pump-wavelength with a 50 fs pulse width, 1000 Hz repetition rate, and 1 W average power laser pulse. Dashed lines show the calculated classical cutoff energies. The longer driving wavelength exhibits an extended plateau region and HHG intensity therefore depends significantly on wavelength.

Comparing the spectra generated at the wavelengths of 400 and 800 nm in Fig. 5.2 it is clear that the position of the cutoff has a major impact on how the intensity of the harmonics depends on pump wavelength. Within the plateau, i.e. at low harmonic energies below 35 eV, both laser wavelengths generate relatively similar amounts of harmonics. On the other hand, at harmonic energies that are beyond cutoff of the 400 nm pump laser but in the plateau region of the 800 nm laser the difference in harmonic energy can be many orders of magnitude. We thus expect very different wavelength scaling depending on the chosen harmonic energy region and laser power.

Moreover, there is no unique way to compare the HHG conversion efficiency at different pump wavelengths. One possibility is to consider the intensity of a single harmonic order, e.g. the 21st harmonic. On the other hand, the energy of a specific harmonic

order moves across the spectrum with the pump wavelength. Alternatively, one can compare the intensity of single harmonic peaks that are closest to a target harmonic energy, for example the intensity of the first harmonic order with energy above 20 eV. As the pump wavelength is increased, this requires "jumping" between different harmonic orders, but for practical applications this is a more relevant comparison. Additionally, a long wavelength pump has more closely spaced harmonics, for example in Fig. 5.2 there are twice as many harmonic peaks for the 800 nm pump than for the 400 nm pump, which will on average reduce the intensity of each individual harmonic peak. An integral of generated harmonic intensity over a wider energy range will therefore provide a more accurate picture of the scaling of overall harmonic generation efficiency with pump wavelength. Several of these different measures to compare HHG efficiency will be investigated in the following. We therefore simulated harmonic spectra such as those of Fig. 5.2 for a wide range of pump wavelengths and integrated the generated harmonic intensities either over single peaks or over a range of harmonic energies. In all cases, these integrated harmonic intensities give the radiated energy per unit time of the generated harmonics over the given energy range [42].

Figure 5.3 gives the single atom harmonic intensity of two specific harmonics, 20 eV and 41.8 eV, and of an integrated harmonic energy range, 20 - 45 eV, for different driving wavelengths. The harmonic energy range was of interest as it was a range comparable to those investigated within the literature [41, 100, 111] and the two specific harmonics were of interest as one was close to the start of this interval and the other was close to the end of it. This then allowed us to compare the scaling behaviour of two individual harmonics and an integrated harmonic spectrum.

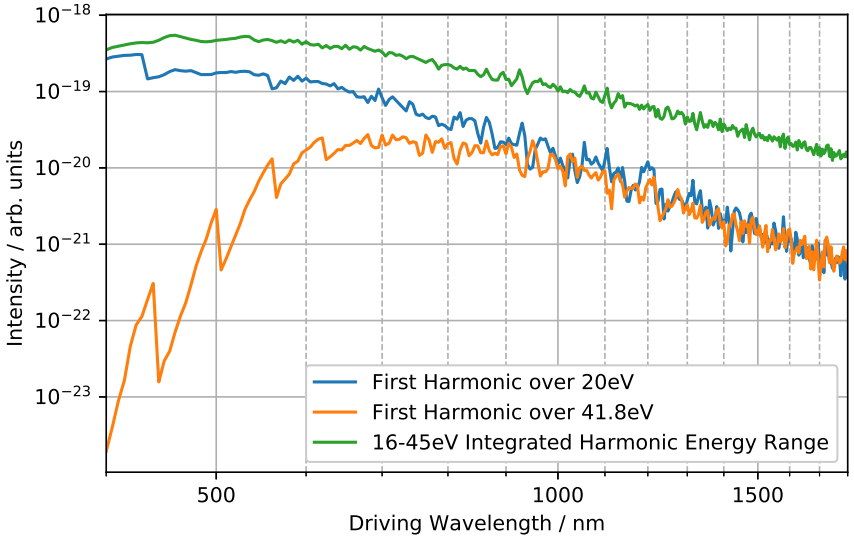

FIGURE 5.3: Single atom harmonic intensity for driving wavelengths 400 - 1800 nm for a 50 fs pulse width, 1000 Hz repetition rate, 1 W average power driving laser. Green line: harmonic intensity integrated over the 16-45 eV range. Blue line: first harmonic over 20 eV. Orange line: first harmonic over 41.8 eV.

Let us first consider the first harmonic above 41.8 eV. As a function of pump wavelength, its intensity first increases, then levels out, and finally decreases. At the shortest wavelength, this harmonic is beyond cutoff and hence little harmonic radiation is generated. As the pump wavelength increases, the cutoff increases, Eq. (2.27), and hence approaches the target harmonic energy of 41.8 eV leading to a major increase in generation efficiency. The sudden jumps in the figure below 700 nm occur when a harmonic order crosses below 41.8 eV and hence the next higher order is selected and followed along the curve. As the driving wavelength increases further, the energy of 41.8 eV moves into the plateau and the intensity of the chosen harmonic levels out. When the wavelength continues to increase, the harmonic moves further into the plateau and is generated less efficiently [37, 113]. Combine with this the larger number of harmonic orders being generated for increasing wavelength and there is thus a decreasing intensity with driving wavelength increases as the harmonic under consideration occupies an ever decreasing fraction of the total harmonic intensity generated.

The intensity of the first harmonic above 20 eV in Fig. 5.3 does not show the initial strong increase as seen with the harmonic at 41.8 eV because it is already below cutoff for all wavelengths shown in the figure. This curve thus starts at maximum intensity and the intensity decreases for longer pump wavelengths for the same reasons as discussed above. For sufficiently long wavelengths, from around 1000 nm, both harmonics at 20 and 41.8 eV have very similar intensities and scale similarly with wavelength.

Finally, we show the intensity of the harmonics generated in the energy range from 16 to 45 eV in Fig. 5.3. At the shortest wavelength shown (400 nm) this curve is very close to the curve of the harmonic at 20 eV, indicating that this single harmonic contributes the majority of generated harmonic radiation. For longer pump wavelengths, more and more harmonic orders contribute in this energy range and thus the curves differ more strongly. Due to this increasing number of contributing harmonics and the increasing number of harmonics generating within this energy range, the dependence of this integrated harmonic intensity on pump wavelength is weaker than for single harmonics, i.e. there is a smaller slope of the curve in the figure.

In the literature [37, 41, 42, 59, 100, 101, 104, 111] often a single power law following Eq. (5.1) is assumed to describe the wavelength dependence of HHG efficiency, i.e., a linear fit in a logarithmic plot such as Fig. 5.3 is made. When these linear fits are applied to our results that are below the cutoff, as shown later in Section 5.6.3, a scaling exponent of -3.3 ± 0.1 is found for the single atom case, showing good agreement with the literature as this would expect to become -5.3 when taking into account the missing quantum diffusion factors due to the reduced dimensionality of the model used. However, our simulations show clearly that this approach is generally too simplistic and a single exponent x in Eq. (5.1) is not a true representation of the scaling. In the following we fit a power scaling law to curves such as those in Fig. 5.3 over different ranges of wavelengths and discuss the corresponding power law exponent x.

Figure 5.4 shows the HHG driving wavelength scaling exponents x of the harmonic energy integrated over the range 16-45 eV for different driving wavelength ranges when using our 1D single atom model. The error bars given in the figure have been calculated as the 95% confidence interval of the fit applied to the data used within Figure 5.3. Here the cutoff is between the 400-600 nm and 600-800 nm intervals, shown by the transition from positive to negative exponents. The exponent then is relatively constant around $x = -3$ to -4. Here we expect a dependence of -3 for harmonic generation occurring close to the cutoff and -4 for generation from within the harmonic plateau, which would then become -5 and -6 respectively when using a 3D single atom model and accounting for the missing quantum diffusion. Whilst these -3 and -4 factors could be present in our results, due to the wide range of the confidence intervals it is inconclusive.

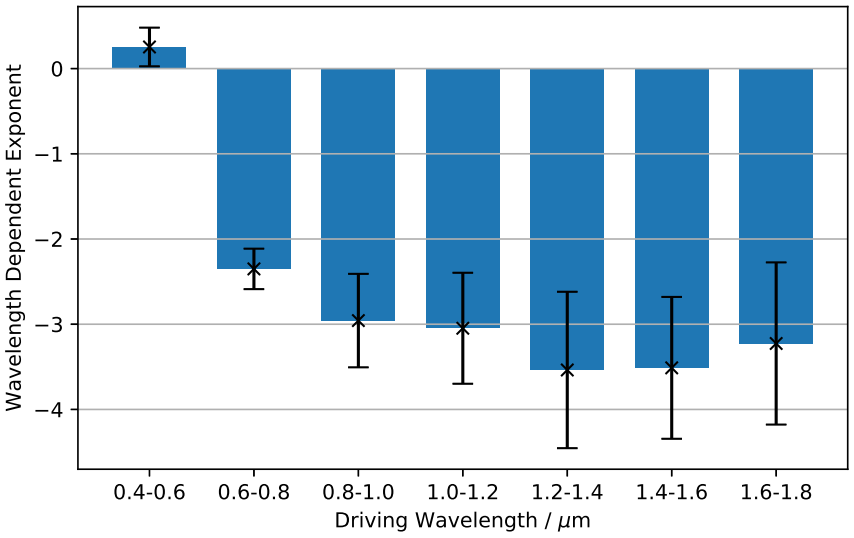

FIGURE 5.4: HH driving wavelength exponent x for the harmonic intensity integrated over the 16-45 eV energy range generated by single atoms driven by a 50 fs pulse width, 1000 Hz repetition rate, 1 W average power laser versus varying driving wavelengths, using our 1D single atom model. The error bars indicate the 95% confidence interval of the fit.

The driving wavelength exponents for the first harmonics over 20 eV and over 41.8 eV are given in Fig. 5.5, again for our 1D single atom model.

In Fig. 5.5(a) for the first harmonic above 20 eV all exponents are negative indicating that for the chosen parameters the harmonic is never beyond the cutoff. For wavelengths between 600 and 1800 nm the exponent is generally higher than for the integrated harmonic energy of 16-45 eV case shown in Fig. 5.4, being typically between $x = -4$ to $x = -6$, as already seen by the steeper slope of the corresponding curve in Fig. 5.3, and which would be expected to be between $x = -6$ to $x = -8$ in the full 3D case. Thus, while each single harmonic becomes less intense with longer driving

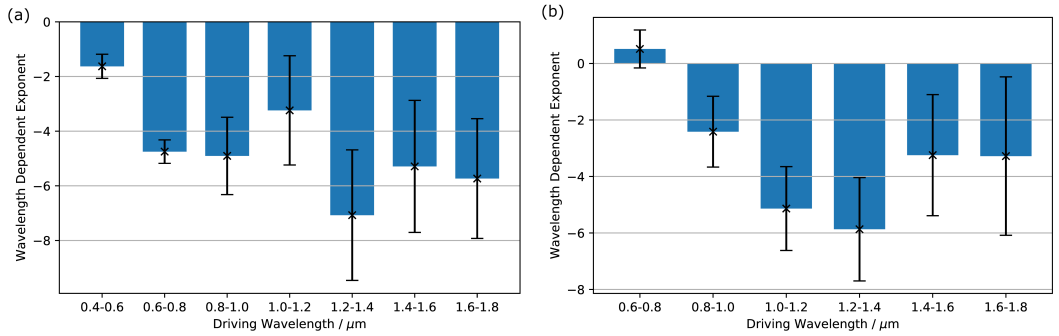

FIGURE 5.5: HH driving wavelength exponent x for (a) the first harmonic over 20 eV and (b) over 41.8 eV generated by single atoms driven by a 50 fs pulse width, 1000 Hz repetition rate, 1 W average power laser versus varying driving wavelengths, using our 1D single atom model. The error bars indicate the 95% confidence interval.

wavelength, this is partially compensated in the integrated spectrum by there being more harmonics inside the energy range of integration and by their closer spacing.

The 41.8 eV harmonic, Fig. 5.5(b), shows similar trends as the 20 eV harmonic and the integrated harmonic spectrum. The main difference, however, is at the shortest wavelengths where we notice the effect of the cutoff playing an important role. Here the cutoff lies between the 600-800 nm and 800-1000 nm intervals, giving rise to very low and even positive scaling exponents. For longer wavelengths, beyond the cutoff, we again observe a value of x typically between around -4 and -6, expected to become between -6 to -8 for the full 3D case. For 1400 nm and upwards the error bars becomes wide, spanning from almost 0 to -6 for the highest wavelength range. This is due to the large fluctuations in the intensity of this harmonic and means that the determined value of x for this wavelength range is unreliable since the error bars show the range of values in which there is a 95% confidence of the true value being within it. Overall, we note the larger error bars in Figs. 5.5(a) and (b) compared to Fig. 5.4 because the integration over a larger number of harmonic peaks leads to an averaging of the driving wavelength dependent variations in harmonic intensities and thus smoother curves.

In order to get a more detailed understanding of how both the driving laser intensity and wavelength affect the generated harmonic intensity we plot this dependence for the first harmonics over 20 and 41.8 eV in Fig. 5.6. Note that as the driving wavelength increases, different orders of harmonics correspond to the first harmonic above 20 or 41.8 eV, leading to the observed jumps at specific wavelengths in the figures. The previous 20 and 41.8 eV plots of Fig. 5.3 are also horizontal cuts through Fig. 5.6 here.

In Fig. 5.6(a), the intensity of the first harmonic over 20 eV clearly shows the effect of the classical cutoff (indicated by the white line), with negligible intensities generated beyond the cutoff. For constant driving laser wavelength, as pump intensity is increased towards and beyond the cutoff the generated harmonic intensity rapidly increases. HHG just beyond the cutoff is generally most efficient. For further increasing

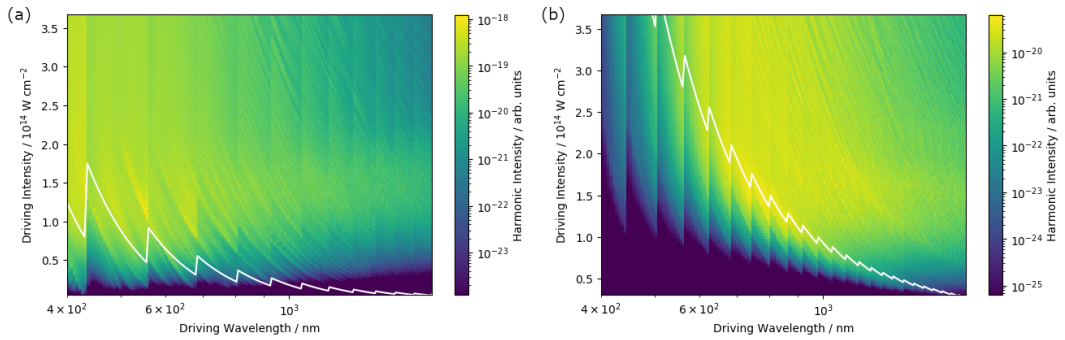

FIGURE 5.6: High harmonic intensity generated by single atoms of the first harmonic (a) over 20 eV and (b) over 41.8 eV for a laser pulse with changing driving wavelength and intensities, and a 50 fs pulse width. The white lines indicate the driving laser intensity required for the harmonics to be generated at the classical cutoff, for the given driving wavelengths.

laser intensity the harmonic generation occurs further into the harmonic plateau where HHG is less efficient and the generated harmonic intensity decreases again. For a given laser wavelength, there is thus an optimum laser intensity to generate the maximum intensity in a given harmonic. The figure also indicates a finer structure of harmonic intensity as a function of laser power, leading to the diagonal stripes. This fine structure has previously been studied and found to be a result of interference between high-order quantum orbits when using quasiclassical analysis [100, 101] and to be a result of threshold phenomena at the closing of multiphoton ionisation channels [41, 59] when using quantum analysis.

For fixed laser intensity, we find that the highest intensity of the harmonic beyond 20 eV is generally generated at shorter pump wavelengths and the harmonic intensity decreases with increasing wavelength. As discussed above, this is attributed to the wider spacing between harmonics at short pump wavelengths which on average leads to higher harmonic peaks compared to longer wavelength pumping where the generated harmonic intensity is distributed among many more peaks, as well as more efficient generation from lower order, more efficient electron returns. Interestingly, there is an optimum laser intensity between 1.0×10^{14} and 1.5×10^{14} W cm^{-2} that is optimum for all wavelengths considered here. As the data used to form Fig. 5.6(a), and also Fig. 5.6(b), is multiple single atom calculations for different laser wavelengths and intensities, where the driving laser in all cases is Gaussian both temporally and spectrally but no spatial dependence is taken into account, this optimum is not specific to a given geometry.

The behaviour of the first harmonic above 41.8 eV, Fig. 5.6(b), is generally similar. The largest difference compared to Fig. 5.6(a) is that here the shorter driving wavelengths are below the cutoff (indicated by the white line) for the selected harmonic at nearly all powers shown in the figure. As a function of laser wavelength, the most efficient HHG

is therefore found at intermediate wavelengths around 600 to 1000 nm, and for laser intensities ranging from 1.0×10^{14} to 2.5×10^{14} W cm^{-2}.

5.6.2 Sheet of Atoms

As mentioned before, experimental investigations typically involve clouds of atoms that are larger than the laser beam size and thus single atom simulations do not represent such experiments. Next, we therefore consider the case of a laser beam with a Gaussian transverse mode profile passing through a cloud of atoms short enough that beam propagation effects can be neglected. This is the geometry of a thin gas jet or a sheet of atoms. We thus simulate the high harmonic spectra emitted from atoms located at different distances from the laser beam axis and perform an integration of the harmonic intensity over the cross section of the laser.

The use of a Gaussian laser beam profile means that atoms at different distances from the axis experience laser pulses of different peak intensities. Two effects are thus impacting the integrated harmonic spectrum. First, as seen above in Fig. 5.6, for every given laser wavelength there is an optimum laser intensity that generates the highest intensity harmonic radiation; typically this is a laser power near the classical cutoff. Second, the number of atoms at a radial position r scales linearly with r and thus the harmonic spectrum integrated over the laser beam cross section has much larger contributions from atoms sitting in the lower-intensity outer regions of the laser than from atoms near the maximum laser intensity at its centre.

When the harmonics under consideration are close to the cutoff for radial positions close to the centre of the sheet then the integrated spectrum from a sheet of atoms will be dominated by atoms sitting at these locations where the laser has this optimum intensity. From this it would be expected for the scaling of the harmonic intensity to be similar to the cutoff scaling for the single atom. As the driving wavelength increases the radial position corresponding to generation at the cutoff increases, whilst radial positions prior to this would then be generating from within the plateau. Therefore, due to the rapidly growing number of atoms generating within the plateau, the harmonic scaling would be expected to start with the lower cutoff-based wavelength dependence and then to rapidly transition to the higher plateau-based dependence. Comparing the scaling for the harmonic energy integration over 16 - 45 eV and the two specific harmonics at 20 and 41.8 eV we would again expect to see a similar difference in the scaling. This is since any effects of moving from a single atom to a sheet of atom are expected to be the same for the harmonic energy integration range and the specific individual harmonics. Therefore additional λ^{-1} effect on pump-wavelength scaling when moving from an integrated harmonic energy range to a single harmonic is expected to remain.

In Fig. 5.7 we show the driving wavelength scaling exponent x, Eq. (5.1), after fitting the harmonic spectrum integrated over the cross section of a thin sheet of atoms for the harmonic intensity integrated over the energy range 16-45 eV, the first harmonic over 20 eV, and the first harmonic over 41.8 eV. Here the radius of the thin sheet of atoms is 75 μm and the waist of the laser pulse is 48 mum.

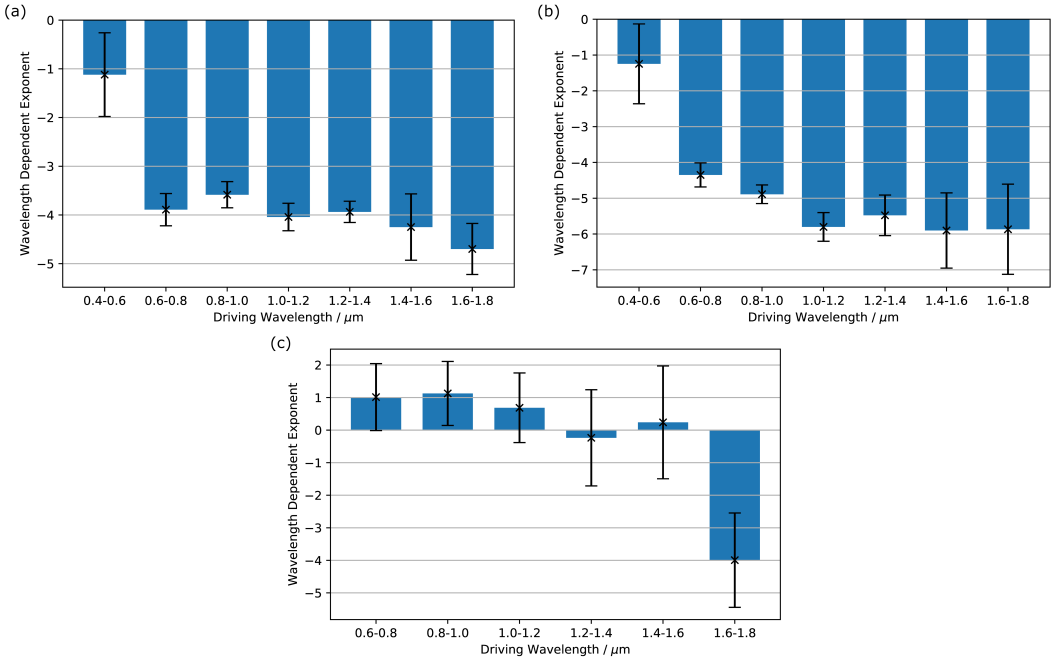

FIGURE 5.7: HH driving wavelength exponent x for a 50 fs pulse width, 1000 Hz repetition rate, 1 W average power, 48 μm waist driving laser exciting a thin sheet of atoms for (a) harmonic intensities integrated over 16-45 eV, (b) the first harmonic over 20 eV, and (c) the first harmonic over 41.8 eV. The error bars are the 95% confidence interval.

For the harmonic intensity integrated over the energy range 16 - 45 eV, Fig. 5.7(a), the HHG efficiency scaling lies between the extremes of the two individual harmonics. Given that the spatial laser profile is generally dominated by the low intensity components, the scaling is closer to the case of the harmonic at 20 eV than to the high energy 41.8 eV harmonic. The scaling starts very small at 400 - 600 nm with a value of approximately -1 and then this very quickly increases to around -3.5 to -4.5 over the rest of the driving wavelengths. This is due to the harmonics within the 16 - 45 eV range quickly moving from generation at the cutoff to the plateau, increasing the scaling dependence. For the longer driving wavelengths, the error bars of both the sheet of atoms and the single atom are too large to determine if their scalings are comparable, though for the shorter wavelengths below 1200 nm we see that the sheet of atoms has a larger wavelength dependence on the scaling compared to the single atom, with the values being -4 and -3 respectively.

For a low energy harmonic such as the first harmonic over 20 eV, Fig. 5.7(b), the cutoff is only affecting the shortest driving wavelengths of 400-600 nm. For longer wavelengths

the exponent x is around -4 and slowly increases to -6 at the longest wavelengths under consideration. In this regime, far above threshold, the scaling exponent is the largest out of all those seen within the sheet of atoms though is comparable to some of the observed dependences for the single atom.

For the first harmonic over 41.8 eV, Fig. 5.7(c), most atoms within the laser beam cross section are below the cutoff. This leads to positive values of x up to around 1600 nm. At long wavelengths, 1600 to 1800 nm, the exponent is between $x = -3$ and -5. This is potentially smaller than the value found for the single atom at this driving wavelength. This is due to most atoms in the sheet experiencing lower laser intensities and so generating this harmonic closer to cutoff where there is the smaller driving wavelength scaling value.

5.6.3 Capillary

Finally, we investigate the driving wavelength dependence of high harmonic generation in a capillary. These are three-dimensional simulations including all propagation effects of the driving laser pulse and the generated harmonics through the 7 cm long capillary. They are complex and time-consuming simulations, each taking around 2 - 2.5 days to run. Each involves 2.37 million single atom response calculations throughout all the capillary, with each of these calculations involving a unique interacting pump-laser pulse. These give the resulting HHG spectra throughout the entire capillary, which are then propagated to the end and combined together to give the high harmonic spectrum as seen at the capillary end. The results for the capillary thus provide unique insights into the wavelength scaling of realistic experimental setups [24, 25, 43, 44].

To highlight some of the effects of laser pulse propagation on HHG we first discuss a few high harmonic spectra for selected laser parameters and the corresponding on-axis lasers as seen after propagation through the 7 cm length capillary. The on-axis spectral laser profiles are used, given in Figure 5.8, as they display the largest amounts of nonlinear distortion to the laser pulse as it has propagated, helping to highlight the effects of its propagation that affect the properties of the harmonic generation. Figure 5.9 shows the high harmonic spectra produced from the argon-filled capillary for 1 W laser power at 400 and 800 nm wavelengths. With the 400 nm driving wavelength, Fig. 5.9(a), we observe two distinct peaks at the 7th and 9th harmonics. Here the harmonics are shifted to slightly higher energies than expected from the laser driving wavelength, due to blue shifting of the pump laser frequency by the induced plasma nonlinearity as the pump pulse propagates through the capillary as seen in Fig. 5.8(a).

In addition to nonlinear laser pulse propagation, the strong absorption of XUV radiation by argon gas, as shown previously in Fig. 2.5, also significantly alters the harmonic

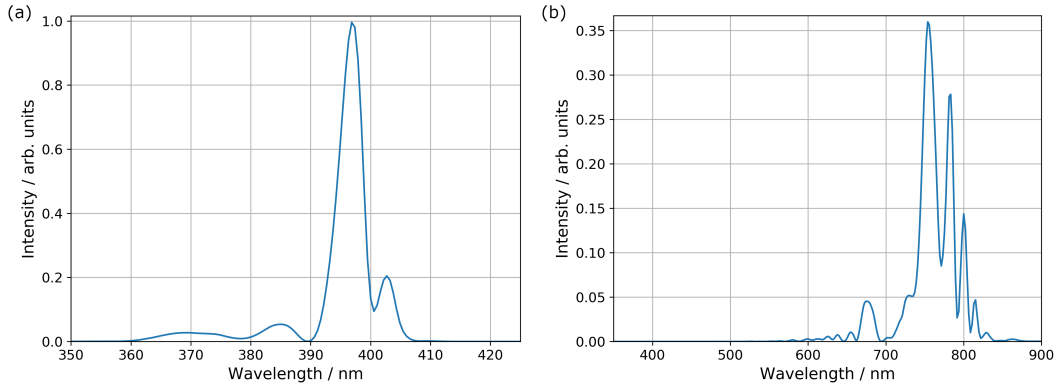

FIGURE 5.8: On-axis spectral laser profiles of two 50 fs pulse width, 1000 Hz repetition rate, 1 W average power lasers with a (a) 400 nm and (b) 800 nm wavelength, as seen propagated to the end of a 7 cm length 150 mbar pressure hollow capillary.

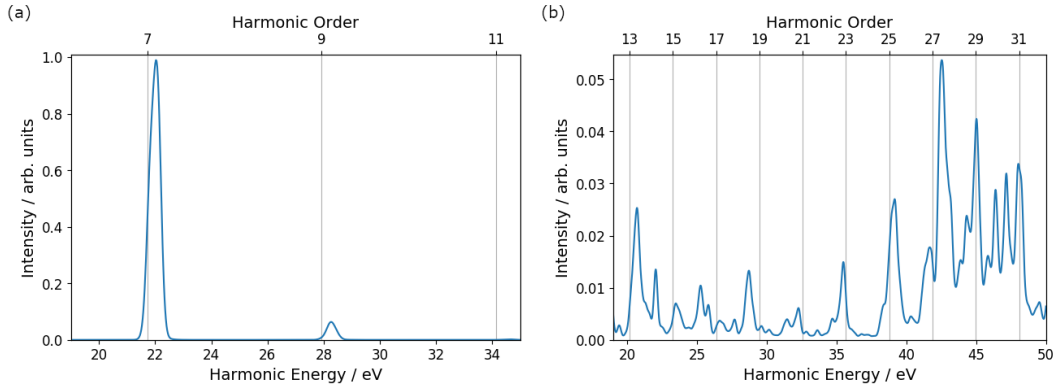

FIGURE 5.9: Harmonic spectra generated by a 50 fs pulse width, 1000 Hz repetition rate, 1 W average power, 48 μm waist driving laser in a capillary of 7 cm length filled with argon at 150 mbar pressure. The laser wavelength is (a) 400 nm and (b) 800 nm.

spectrum observed at the end of the capillary. While the capillary allows for HHG over an extended length of propagation, most spectral components of the generated XUV are subsequently absorbed again by the gas; even harmonics in the energy range of approximately 16 to 40 eV, where absorption is relatively low [55, 2], are only transmitted to the capillary output if they are generated within the last few mm of the capillary.

The harmonic spectrum generated with a 800 nm laser is shown in Fig. 5.9(b). At 800 nm wavelength the same 50 fs pulse length corresponds to a broader spectrum than at 400 nm wavelength and the harmonics are more closely spaced by a factor of two. Nonlinear pulse propagation effects in the capillary further broaden the driving spectrum and hence in this case the spreading of generated harmonics is more pronounced compared to the 400 nm driving wavelength, as shown in Fig. 5.8(b). As expected, the spectrum extends to much higher energies and maximum spectral densities are observed at around 45 eV for the 800 nm driving wavelength.

Because of these significant propagation and wavelength dependent effects in a three-dimensional situation, we can expect that HHG in a capillary scales differently than

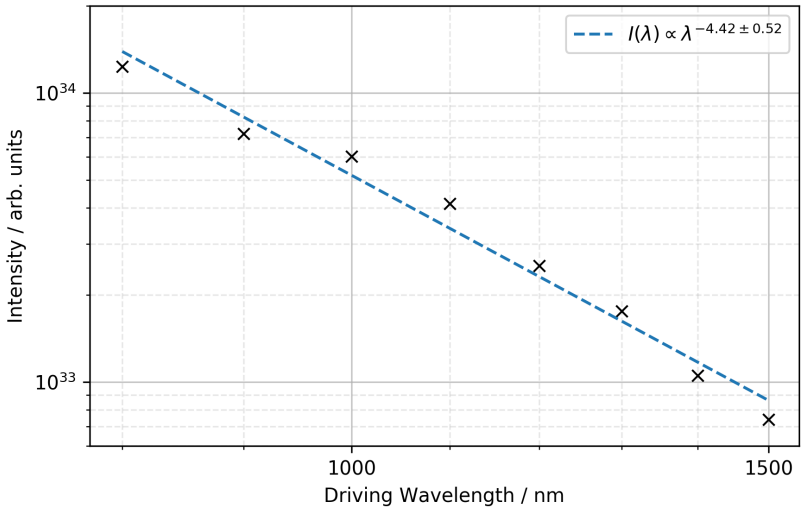

FIGURE 5.10: High harmonic intensities integrated over the 16 - 45 eV harmonic energy range for pump-wavelengths 800 - 1500 nm when using a 50 fs pulse width, 1000 Hz repetition rate, 1 W average power 46 μm waist driving laser and a 7 cm length, 75 μm radius, 150 mbar pressure argon gas-filled hollow capillary.

single-atom HHG and HHG from a sheet of atoms. Given that in the capillary simulations it is often difficult to distinguish individual harmonics, as shown in Fig. 5.9, we will here only present results for the total harmonic intensity integrated over the harmonic energy range 16 - 45 eV. We also note that these three-dimensional simulations are very time consuming and thus data was only generated for driving wavelengths in the range 800 - 1500 nm in increments of 100 nm.

Figure 5.10 gives the resulting harmonic intensities integrated over the 16 - 45 eV harmonic energy range. Here we see a pump-wavelength dependent exponent of $x = -4.4 \pm 0.5$. This dependence for the capillary is larger than for the single atom by approximately a factor of λ^{-1}, shown in Fig. 5.5. Due to the coarse grid of pump-wavelengths any fine scale structure cannot be seen.

Figure 5.11 shows the HHG wavelength scaling exponents x for the single atom, sheet of atoms, and capillary cases. Here the scaling exponents from Figs. 5.4 and 5.7(a) have been averaged over the driving wavelength range 800 - 1500 nm to give the single atom and sheet of atoms averaged exponents, and the exponent for the capillary has been determined by a fit of harmonic intensities over this same driving wavelength range.

We clearly observe a distinctly different behaviour for the different geometries. The weakest wavelength dependence of $x = -3.3 \pm 0.1$ is observed for the single atom case, in line with previous studies of this geometry [111, 100, 101, 59, 41, 42, 37] when taking into account the differences in quantum diffusion for one and three dimensions. The averaging effect of a sheet of atoms with atoms experiencing different laser intensities depending on their position within the beam profile leads to a higher dependence of $x = -4.1 \pm 0.1$. Whilst nonlinear propagation effects, coherent build-up and phase

matching, and XUV re-absorption are present in the capillary, the dependence for the capillary is still comparable to the sheet of atoms, having a value of $x = -4.4 \pm 0.5$. For these three geometries, we would then expect their scalings to be $x = -5.3$, $x = -6.1$, and $x = -6.4$ respectively when taking into account the full effects of the quantum diffusion.

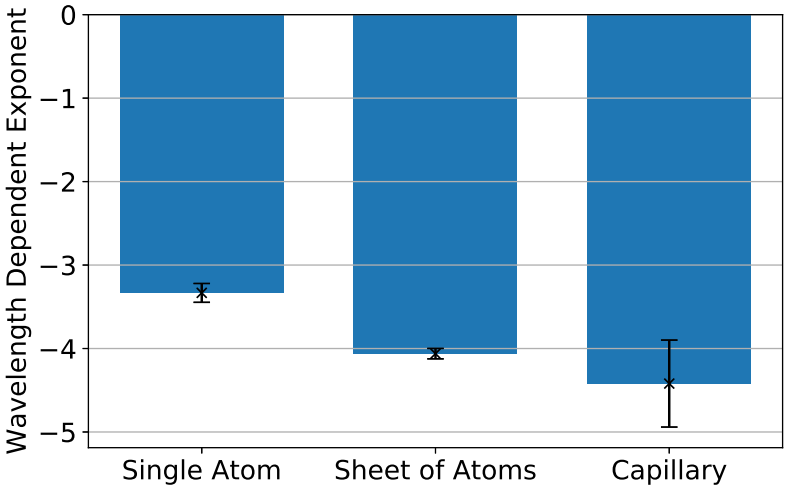

FIGURE 5.11: HH driving wavelength exponents x for a single atom, a thin sheet of atoms, and for a gas-filled capillary, with a 50 fs pulse width, 1000 Hz repetition rate, 1 W average power, 48 μm waist driving laser. Here the exponent was obtained by fitting harmonic intensities integrated over 16 - 45 eV and over driving wavelengths from 800 to 1500 nm. The error bars are the 95% confidence interval.

5.6.4 Pump-Wavelength Scaling Comparisons with a 3D Model

Using the same approach as for the 1D model, we investigate the pump-wavelength scaling on the harmonic generation of single atoms using the 3D model of Patchkovskii et al. [83] using a much more limited range of driving wavelengths, from 400 to 1150 nm and in steps of 50 nm. This shorter and coarser range was used as the 3D model takes considerable time to perform a single atom calculation for the parameters used here, taking up to a few days per atom.

The pump-wavelength scaling for a 16 - 45 eV integrated harmonic energy range is shown in Figure 5.12, with the intensity for each pump wavelength being given as an individual point and the wavelength scaling fit being shown by the blue dashed line.

In Figure 5.12 we see a similar shape to the equivalent plot using our 1D model in Figure 5.3. We see an increase from the shortest pump wavelengths up to a maximum harmonic intensity at around 500 nm, after which a decrease begins in the harmonic intensity that levels out to a constant exponent decrease after a couple of hundred nm increase in pump wavelength. Due to the coarse spacing of data points within the

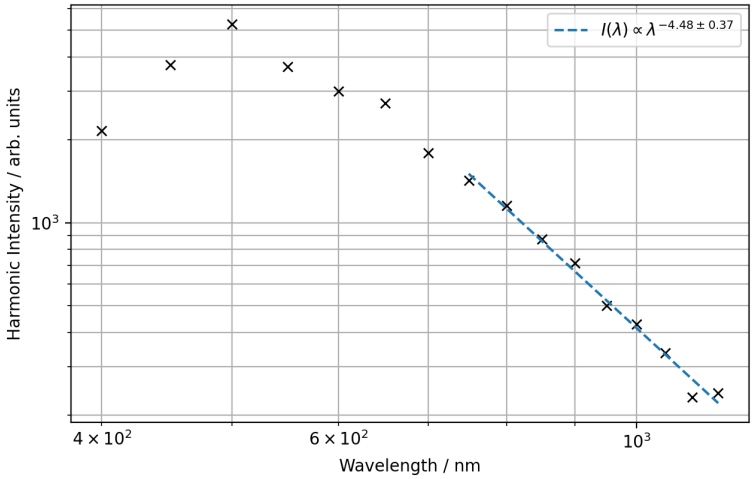

FIGURE 5.12: Pump-wavelength scaling efficiency for the 16-45 eV harmonic energy integrated range using the 3D model of Patchkovskii et al. [83]. Here the laser pulse used had a 50 fs pulse width, a 1000 Hz repetition rate, and a 1 W average power.

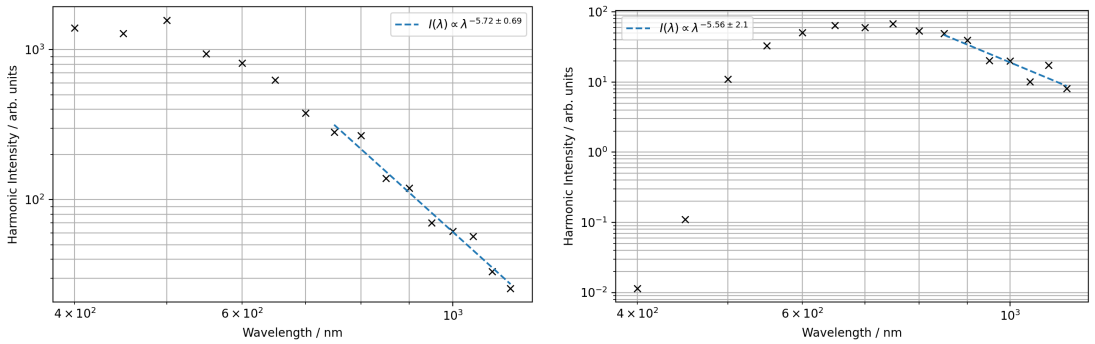

FIGURE 5.13: Pump-wavelength scaling efficiency for (a) the first harmonic over 20 eV and (b) the first harmonic over 41.8 eV using the 3D model of Patchkovskii et al. [83]. Here the laser pulse used had a 50 fs pulse width, a 1000 Hz repetition rate, and a 1 W average power.

figure, there is not enough resolution present to observe any fine scale changing in harmonic intensity with pump wavelength. Fitting the pump-wavelength-dependent exponent to the part of the figure where the wavelength has increased enough for the harmonic generation to be occurring just within the plateau and cutoff, the exponent has been determined to be $x = -4.48 \pm 0.37$. This is close to the expected exponent of -5 for a harmonic energy range, particularly when considering the limited number of data points and wavelength range. This also shows that the 1D and 3D models scale as λ^{-2}.

The harmonic intensities and the resulting pump-wavelength dependence for the first harmonics over 20 and 41.8 eV are shown in Figure 5.13. Here the range of pump-wavelengths is again 400 - 1150 nm, with a spacing of 50 nm between each wavelength.

For the first harmonic over 20 eV, Figure 5.13(a), there is again a similar shape to that

for the 1D model case in Figure 5.3. Again, for the shortest wavelengths the harmonic generation is already occurring at or below the cutoff. As wavelength increases this harmonic intensity decreases, first gradually and then increasing to a constant exponent decrease. For this constant exponent region we calculate that pump-wavelength scaling exponent to be $x = -5.72 \pm 0.69$. This is inline with the expected value of -6 for a single harmonic.

As with the previous figures, the first harmonic over 41.8 eV for the 3D model, Figure 5.13(b), follows a similar shape to the equivalent plot in Figure 5.3, with very small initial harmonic intensities that increase until the harmonics are generating at the cutoff, and then a decrease occurring in harmonic intensity past this. The fit here has again been made using the data points at and after the peak in harmonic intensity so that only harmonic within the plateau and at the cutoff are included. Doing this we find the scaling exponent to be $x = -5.56 \pm 2.1$, again similar to the expected value of -6. Due to the very limited number of data points and the coarse grid used, the 95% confidence interval is very large however and so this result is not reliable on its own.

Overall, the general shapes of the harmonic intensities with increasing pump-wavelength match well between the 1D and 3D model. Peaks in harmonic intensity and positions of cutoffs also appear at comparable pump-wavelengths between the models. The exponent values determined using the two models match well with each other, and with expected values from the literature, when taking into account the reduced dimensionality to the quantum diffusion within the 1D model.

5.7 Conclusions

We have investigated in detail how the efficiency of high harmonic generation in a gas medium depends on the wavelength λ of the driving laser. In previous literature this HHG efficiency was assumed to scale as λ^x, Eq. (5.1), with the scaling exponent x assumed to be constant. In our simulations we find that the value of x is not constant across all wavelengths and also depends significantly on the geometry of the high harmonic generation setup.

Generally speaking, the wavelength dependence is lowest when high harmonics are generated within the harmonic plateau near to or at the cutoff, i.e. with values of $x = -3$ to -4. Beyond the cutoff the generated harmonic intensities are too small to be relevant, whereas for harmonic generation deep within the harmonic plateau, i.e. values of x are between $x = -4$ and -6. These then become $x = -5$ to $x = -6$ and $x = -6$ to $x = -8$ respectively when taking into account the full 3D effect of quantum diffusion.

Comparing our single atom results to those gained from full 3D simulations, whilst our model involves a simpler 1D atom it still provide useful insight, and when taking into account the reduced dimensionality to the quantum diffusion of our 1D atom, our results are comparable to those from full 3D models within the literature. Previous numerical models within the literature have been limited to investigations into the pump-wavelength scaling of single atoms. Here, however, we expand that to two further geometries, a thin sheet of atoms and a gas-filled hollow capillary. These geometries are much more complex than the single atom and involve many harmonic-generating atoms, and pump-pulse propagation effects for the capillary. Due to this they take significantly more computing power to simulate, which would not be practical to do with more complex 3D models.

In geometries such as the thin sheet of atoms and the gas-filled hollow capillary, where many atoms interacting with different parts of the driving laser pulses contribute to the overall harmonic generation, averaging effects make the harmonic generation more wavelength dependent. Specifically, we found that HHG from single atoms on the laser beam axis exhibit weaker wavelength dependence of HHG efficiency compared to thin sheets of atoms sampling the entire laser beam profile. Despite laser pulse propagation, in particular nonlinear spectral broadening, and re-absorption of generated harmonics in the fully three-dimensional situation of a gas-filled capillary, there is a similar wavelength dependence to the sheet of atoms.

We anticipate that these results will provide important guidance for the design of future HHG sources of extreme ultraviolet and X-ray radiation for applications in coherent imaging and spectroscopy.

Chapter 6

HHG Comparisons with Different Laser Systems

6.1 Introduction

When designing laser systems to be used in experiments involving capillary-based high harmonic generation there are many different system parameters that can be chosen, all of which can dramatically affect the HHG profiles. For instance, a longer driving wavelength extends the cutoff and harmonic plateau, allowing for the generation of higher energy harmonics though also decreasing the intensity of lower energy harmonics compared to shorter driving wavelengths. Additionally, a higher intensity driving pulse increases the maximum possible energy of the generated harmonics, as well as increasing the intensity of harmonics generated within the plateau. However, it also gives rise to increased amounts of nonlinear distortion and breakup of the laser pulse as it propagates through the capillary which in turn can reduce the intensity or maximum energy of the generated harmonics due to potentially less favourable HHG conditions. The pulse length of the driving laser can also dramatically affect the HHG and can, for instance, be chosen to be either very wide or very narrow. The first results in a many-cycle pulse with a lower energy per cycle, giving rise to lower intensity and energy harmonics. However, it also results in a lower amount of nonlinear distortion for the driving pulse and therefore generation of clearer harmonics. The second results in a few-cycle pulse with higher energies per cycle. This gives rise to higher intensities and maximum energies of the generated harmonics though it also results in much more distortion of the driving pulse, potentially reducing the clarity and maximum energy of generated harmonics. Therefore, by knowing how these parameters affect the harmonic generation of a given system, a laser can be chosen to optimise for various effects, such as the clarity, intensity, and maximum energy of generated harmonics.

Laser System	Wavelength / nm	Average Energy / mJ	FWHM / fs	Rep Rate / kHz
Ti:Sapph	800	1.0	50	1
Yb-fibre 1	1050	4.0	220	100
Yb-fibre 2	1050	2.0	25	100
Yb-fibre 3	1050	1.0	7	100
Mid-IR OPCPA	1700	0.17	50	100
Tm-fibre	2000	0.4	100	11

TABLE 6.1: A table giving the parameters of the six different laser systems modelled throughout Chapter 6.

In this chapter, six different laser systems are modelled and investigated to gain insights into their capabilities for harmonic generation when using them in conjunction with gas-filled hollow capillaries. The lasers differ in terms of their wavelength, average energy, FWHM, and repetition rates. The parameters from each system are given in Table 6.1, with there being one Ti:Sapph [24], three Yb-fibre [80, 82], one Mid-IR OPCPA [1], and one Tm-fibre [70] laser systems.

High harmonic generation is considered for the capillary geometry, as previously shown in Figure 5.1(c) of Chapter 5. Here the initial capillary used was 7 cm in length, had gas inlets 2 cm from either end, was 150 μm in diameter, had a maximum gas pressure of 150 mbar, and all pump laser beams have a waist of 64% the capillary radius to achieve the optimal launch conditions of the laser pulse discussed in Section 2.1.5 [24, 25, 43, 44].

Each laser system is investigated in turn. First, the spectra they produce for the 7 cm capillary are given and compared with each other, then temporal, spectral, and spatial profiles of the lasers are examined, along with the resulting high harmonic generation. After that, the harmonic spectra produced from capillaries of varying lengths are investigated, as are the increases in harmonic intensity for different length capillaries, normalised to a 7 cm capillary.

6.2 High Harmonic Comparisons at the End of the Capillary

Each laser system generates different harmonics at different intensities and so comparing the spectra generated from the same capillary using the different laser systems helps in determining which optimisations in HHG can be obtained from which laser systems.

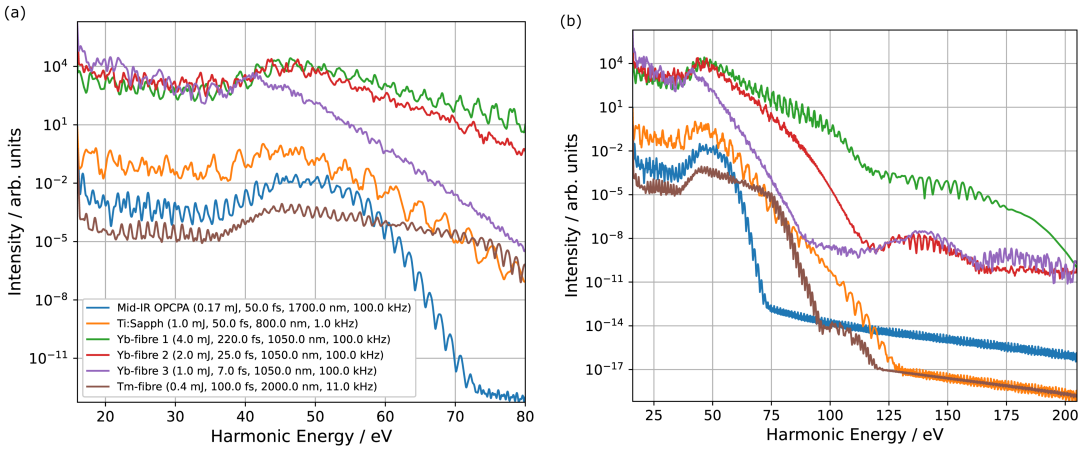

FIGURE 6.1: Spectra of high harmonics generated within a capillary and propagated to its end for six different laser systems, for the harmonic energy range (a) 16 - 80 eV and (b) 16 - 205 eV. X-ray absorption effects are seen between 16 - 40 eV. Different cutoffs and plateau region lengths are observed for each laser system, with the Mid-OPCPA system having the shortest plateau and cutoff and then Yb-fibre systems having the highest intensities and longest plateaus.

6.2.1 Combined Harmonic Spectra

Figure 6.1 presents the generated harmonic spectra at the end of the 7 cm capillary for the six different laser systems given in Table 6.1 and over two harmonic energy ranges, 16 - 80 eV and 16 - 205 eV in Figure 6.1(a) and Figure 6.1(b) respectively. Here the three Yb-fibre laser systems dominate and produce significantly higher intensity harmonics for all harmonic energies under consideration. This is due to a number of factors, including their higher average pulse energies compared to the Mid-IR and Tm-fibre systems, their longer wavelengths compared to the Ti:Sapph system, and their higher repetition rates compared to the Ti:Sapph and TM-fibre systems.

Observing Figure 6.1 in more detail, for harmonic energies around 16 - 30 eV the Yb-fibre 3 laser system generates the highest harmonic intensities. Above 30 eV this instead changes to the Yb-fibre 1 and 2 systems, with the Yb-fibre 1 system eventually consistently generating the highest harmonic intensities for harmonics over 50 eV. Over the harmonic energy range 16 - 80 eV, the largest decreases in harmonic intensity with increasing harmonic energy are experienced by the Yb-fibre 3 and Mid-IR systems, with both decreasing by nine orders of magnitude. The biggest difference between the two here is that the decrease for the Mid-IR laser system is due to the effects of the cutoff, which is classically found at 69 eV for the initial driving pulse, whereas this is not the case for the Yb-fibre 3 laser as its initial driving pulse corresponds to a classical cutoff energy of 872 eV. Instead it is due to the large amounts of nonlinear distortions the pulse undergoes as it propagates resulting in conditions unfavourable to the generation of high energy harmonics by the end of the capillary, as discussed further in

Section 6.3.4. Over the harmonic energy range 16 - 205 eV the largest decrease in harmonic intensity is instead seen in the Ti-Sapph laser.

The harmonic intensities resulting from the Ti:Sapph laser are found approximately half way between the Yb-fibre 2 and Tm-fibre lasers for harmonic energies 16 - 40, and then they rapidly decrease, briefly crossing under the Tm-fibre intensities at around 70 eV, before those begin to decrease faster than it. The decrease in harmonic generation relative to the Tm-fibre laser occurs at a faster rate over harmonic energies 50 - 75 eV, which is due to the cutoff for the Ti:Sapph laser system being smaller than the Tm-fibre system, with the corresponding classical cutoff energies of the two lasers being 85 eV and 103 eV respectively. However, between 75 - 100 eV the harmonic intensities of the Tm-fibre laser decreases at a faster rate compared to the Ti:Sapph system, due to the lower peak intensity of the Tm-fibre laser and the Ti-Sapph laser experiencing much larger changes during its propagation and so giving rise to much more complex HHG dynamics, as shown later. The initial larger harmonic intensities of the Ti:Sapph laser are due to the higher laser intensities of that system, discussed further in Section 6.3.1.

All the spectra display clear harmonics depending on which harmonic energies are being considered. The spectra resulting from the Yb-fibre 2 and 3 laser systems display less obvious structure after harmonic energies of around 50 eV for the Yb-fibre 2 laser, except for a small harmonic energy range of 125 - 150 eV, and after around 40 - 45 eV but before 130 eV for the Yb-fibre 3 system. This less obvious harmonic structure is due to the amount of nonlinear distortion these two lasers experience as they propagate through the capillary resulting in large amounts of blueshift and therefore large ranges of driving wavelengths, reducing the clarity of the harmonics generated, as discussed in Sections 6.3.3 and 6.3.4. For the majority of harmonic energies under consideration here, the Mid-IR and Tm-fibre lasers produce the lowest harmonic intensities. However, they also give some of the most distinct harmonic structure, followed then by the Ti:Sapph and Yb-fibre systems. For both the Mid-IR and Tm-fibre lasers, the lower harmonic intensities and clearer harmonics are both due to the lower driving laser pulse intensities. Therefore these lasers generate harmonics at lower intensities though also experience less blueshift and so generate well defined harmonics centred closer to their initial driving wavelengths, as explained in Sections 6.3.5 and 6.3.6. The classical cutoff energies of the Yb-fibre 1, 2, and 3 systems are 125, 495, and 872 eV respectively. These are the highest out of all the systems and the dramatic increase going from Yb-fibre 1 to 2 to 3 is due to the increasing driving laser field between them. The Yb-fibre 1 laser system is seen to generate harmonics beyond the calculated classical cutoff energy. This is due to the distortions it experiences, as well as other potential effects such as phase matching.

Inside the harmonic plateaus generated from all the laser systems there are clear effects of increased absorption by the argon gas for the lower energy harmonics below around 45 eV [55, 2]. This high harmonic absorption has previously been shown in Figure 2.5

of Chapter 2 and here the resulting effects of it are seen as decreases in the harmonic intensities for what should be part of the harmonic plateau. This starts at around 16 eV, with the absorption increasing to a maximum between around 20 - 35 eV, and then decreasing and resulting in the harmonic intensities increasing again past 35 eV.

At a glance, Figures 6.1(a) and (b) show that the Yb-fibre laser systems perform better than the other systems in terms of generated harmonic intensities, with the Yb-fibre 1 system performing the best for harmonic energies over 50 eV, and a mix of the Yb-fibre 2 and 3 systems performing best for lower harmonic energies. This is also however for the specific case of a 7 cm length capillary with 150 mbar argon gas pressure. Analysis of the laser systems profiles and the resulting HHG is needed to try and gain understanding as to why the performance of each system is such, and is discussed in Section 6.3 below.

6.2.2 Individual Harmonic Spectra

Figures 6.2, 6.3, and 6.4 give the generated harmonic spectra obtained from the 7 cm length capillary when using the different laser systems. The distinction between these figures and the previous one of Figure 6.1 is that these show the generated harmonic spectra on a linear-scale plot. This is done to help highlight the details of each one.

The Ti:Sapph laser system result is given in Figure 6.2. Here there are distinct harmonics present close to their expected energies, determined from the odd harmonic orders of the initial driving pulse. Most of the generated harmonics are quite close to these expected energies, with a few harmonics being at energies that are not expected. The reasons for these harmonics at unexpected energies as well as the reasons for most harmonics not being precisely at their expected energies will be explored in more detail later, though briefly, it is due to the nonlinear distortions experienced by the laser pulse within the capillary causing spectral broadening and blueshift, changing the energies at which the harmonics are generated at. The increased absorption effects shown previously are again on display for the lower energy harmonics between 16 and 40 eV. As previously stated, this is expected and due to the harmonic energies within this range being more readily absorbed by the argon gas. This is a feature present in the harmonic spectra for all of the laser systems.

The high harmonics generated using the three Yb-fibre laser systems are given in Figure 6.3. All three results for the Yb-fibre laser systems show significantly higher intensities for the harmonics generated compared to the Ti:Sapph result. For the harmonic energy range 40 - 50 eV we see factor increases in harmonic intensity of 25,000, 20,000, and 5,000 for the Yb-fibre 1, 2, and 3 systems respectively, compared to the Ti:Sapph laser. For the very lowest harmonic energies of around 16 - 15 eV the Yb-fibre 3 laser produces significantly larger harmonic intensities than the other two Yb-fibre systems.

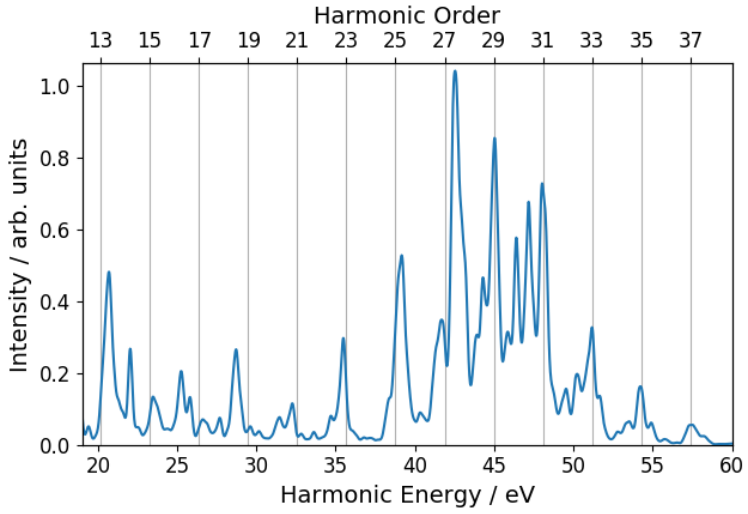

FIGURE 6.2: Generated high harmonic spectrum from a 7 cm length capillary with 150 mbar argon gas using the Ti:Sapph laser system.

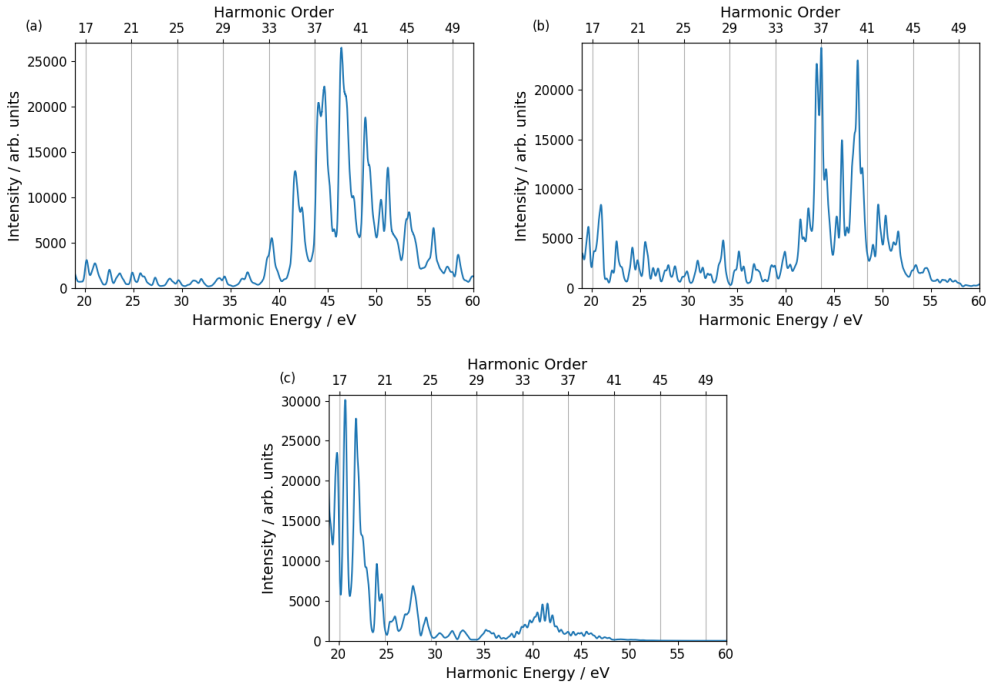

FIGURE 6.3: Generated high harmonic spectrum from a 7 cm length capillary with 150 mbar argon gas using the (a) Yb-fibre 1, (b) Yb-fibre 2, and (c) Yb-fibre 3 laser systems.

The first two have factor increases of up to 2,500 and 7,500 relative to the Ti:Sapph laser, whilst the third Yb-fibre system gives a factor increase of 32,000 times that of the Ti:Sapph system. Comparing the specifications of the laser systems, significant increases are expected as the three Yb-fibre laser systems have a repetition rate two orders of magnitude larger than the Ti:Sapph system, whilst also having a comparable peak pulse intensity for the Yb-fibre 1 system and a higher peak pulse intensity for the Yb-fibre 2 and 3 systems. If all other laser parameters were kept the same, a repetition rate being two orders of magnitude larger would increase the harmonic generation by two orders of magnitude. In addition to this, the scaling in harmonic intensity with the fibre lasers is likely to be due to the differences in other laser parameters, dispersion differences, and different dynamics, such as phase matching. For instance, the different peak intensities of the laser pulses will mean that there are different nonlinear effects, such as ionisation and plasma density, leading to the pulses experiencing very different dynamics. Whilst the dispersion of the fundamental capillary mode for a 150 μm diameter capillary is small, and so will lead to negligible differences between the different laser pulses, the model dispersion (or inter-mode dispersion) differences, which result in wavelength-dependent periodic mode beating oscillations, will have an impact. The HHG phase matching is likely to have an impact too, with it also largely depending on the ionisation, as shown in Eq. (1.9). As such, these need further investigation. Out of these three lasers, the Yb-fibre 1 laser produces the most distinct and regular harmonics, with the harmonics also being the closest to their expected energies, as determined from the initial driving pulse wavelength. This is then followed by the Yb-fibre 2 system and then finally the Yb-fibre 3 laser system. This is due to the laser dynamics of each system, with each successive Yb-fibre system undergoing larger amounts of broadening and blueshift, as examined in Sections 6.3.2, 6.3.3, and 6.3.4 below.

The harmonic generation gained from the Mid-IR and Tm-fibre laser systems are given in Figure 6.4. For the harmonic energies under consideration, the harmonic intensities generated from these laser systems are much lower than the intensities generated from the other systems. The Mid-IR system produces up to 0.03 times that for the Ti:Sapph laser system, and the Tm-fibre system produces up to 0.0085 times that of it. However, the Tm-fibre laser system produces the most distinct and regular harmonics out of all six laser systems, with the Mid-IR laser system producing quite distinct and regular harmonics too. Reasons for this lower harmonic intensity includes that both these two laser systems have significantly smaller pulse energies than the other lasers, lending themselves to less favourable intensity-based HHG conditions, and also the Tm-fibre system having the second smallest repetition rate, reducing the amount of harmonics it can generate relative to the higher repetition rate systems.

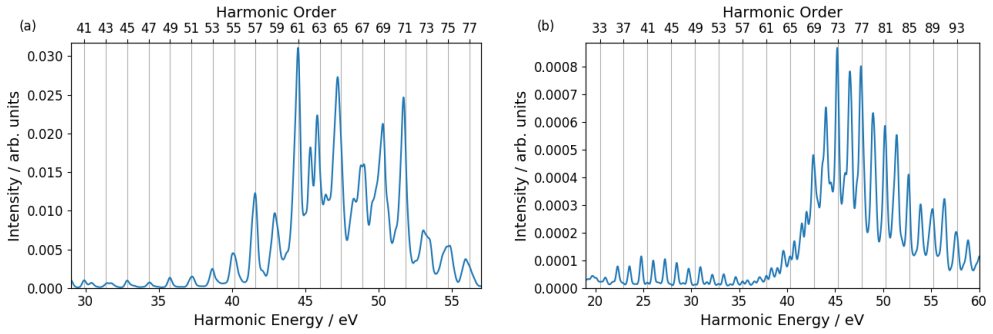

FIGURE 6.4: Generated high harmonic spectrum from a 7 cm length capillary with 150 mbar argon gas using the (a) Mid-IR OPCPA and (b) Tm-fibre laser systems.

6.3 Laser Profile and HHG Comparisons

The temporal, spectral, and spatial laser profiles and resulting high harmonic generation throughout the capillary are of interest as they can be used to give insights and understanding to the behaviour of the laser as it propagates and the resulting HHG due to that given laser profile, which can in turn lead to optimisations in the high harmonic generation. By studying the laser profiles and the harmonic spectra due to them, an understanding can be gained into which laser profiles and conditions produce given harmonic properties. By then knowing these laser profiles that enhance aspects of the high harmonic generation such as clarity, intensity, or maximum energy of the harmonics, capillaries and laser parameters can be tailored to result in increases to these.

The initial laser pulse for each system is Gaussian shaped, both spectrally and temporally. This is then coupled optimally into the fundamental mode of the capillary and propagated through it to the end, where optimal coupling is achieved by using an initial Gaussian pulse with a waist 64% of the capillary radius, as discussed in Section 2.1.5. The plots below give the on-axis and radially integrated laser profiles of each laser system, both temporally and spectrally, as well as the radially dependent and radially weighted laser profiles too, as explained below. The on-axis positions are typically where the laser has the highest intensity and so the on-axis profiles show this highest-intensity behaviour. The radially integration gives an "averaged" laser profile and so these show the behaviour of an "average" laser pulse over the length of the capillary. These are given by

$$I(l) = \frac{1}{\pi R^2} \int_0^R 2\pi r I(r,l) dr \tag{6.1}$$

where $I(l)$ is the radially integrated laser intensity and $I(r,l)$ the radially dependent laser intensity, with r and l being the radial and longitudinal positions throughout the capillary respectively and R being the radius of the capillary. The radially dependent profiles show how the laser intensities vary over both the radial and z-positions of

the capillary and so show where harmonic generation is likely occurring within the capillary.

As the capillary is three-dimensional, with each z-position being a circular cross-section and each radial position for it being a a thin circular band at that radial position, there are significantly less atoms present at the radial centre of the capillary compared to further out radial positions, with the number of atoms present along a given radial position of the circular cross-section linearly increasing with increasing radial position. The result of this is that further out along the radius there is an increasing number of contributions to the total HHG, compared to the centre of the capillary. At the same time, the laser pulse intensity decreases with increasing radial position due to its initial Gaussian shape resulting in a decrease in HHG intensities and energies at further out radial positions. These two effects combine together to give a net effect where further out radial positions contribute much more to the total HHG whilst also contributing diminished harmonic intensities and energies. It is important to consider this and this can be done by performing just the intermediary step in the laser radial integrations to obtain radially weighted laser profiles. These then highlight radial positions that can give rise to significant proportions of observed lower energy HHG. The resulting radially weighted profiles are given by

$$I_{RW}(r,l) = \frac{r}{R} I(r,l) \tag{6.2}$$

where $I_{RW}(r,l)$ is the radially weighted laser intensity and $I(r,l)$ the laser intensity, with each being a function of the radial, r, and the longitudinal, l, positions throughout the capillary of radius R.

During the simulations for each system, the HHG is outputted at 30 different steps along the capillary. Each of these steps gives the harmonic spectra resulting from that slice along the length of the capillary, as seen at the end of the capillary. These can be combined together to give the full spectra as seen at the end of the capillary, as shown in Section 6.2, or instead additional postprocessing work can be performed to gain other insights too.

The high harmonic generation at each position along the length of the capillary is gained and investigated. This is used both on its own to observe and better understand the capillary HHG and also in conjunction with the laser profiles of the system to gain an understanding of how the laser pulse nonlinear distortions and resulting conditions affect the harmonic generation.

Comparisons of the HHG with the laser profiles can be done via observing features present in both at the same capillary positions. These can then be used to deduce or infer information about the causes or effects. The aim from this is to better understand

the capillary harmonic generation and how a given laser pulse and the nonlinear distortions it experiences affects it, with the idea in mind that HHG could then be improved or optimised through using this information.

6.3.1 Ti:Sapph Laser

The laser pulse profiles for the Ti:Sapph system are given in Figure 6.5 and the resulting harmonic generation profile is given in Figure 6.6.

The on-axis laser pulse, Figures 6.5(a) and (b), undergoes spectral broadening and blueshift due to the nonlinear effects of the plasma as described in Eq. (2.22) of Section 2.1.4, as well as temporal breakup and compression [14]. These effects start to occur quite early in the capillary with them becoming particularly noticeable after approximately 2 cm of propagation, corresponding to where the gas pressure within the capillary has the highest value. However for the radially integrated profile, Figures 6.5(c) and (d), the laser pulse takes most the length of the capillary for the temporal effects to become noticeable. Similar to the on-axis profile, the spectral effects become noticeable after 2 cm, though with them becoming much more significant after approximately 4 cm. The differences between the on-axis and radially integrated behaviour are due to the on-axis positions typically experiencing the largest laser intensities, leading to larger distortions of the laser pulse. Whereas the radially integrated profile has large contributions from positions centred around the middle of the capillary radius and so has much more contributions from smaller laser intensities that experience much less distortions and nonlinearities and therefore undergo smaller changes as they propagate. There is also beating between the modes of the capillary which cause periodic increases and decreases in the laser intensity at different radial positions along the length of the capillary, with the beat length between the fundamental and first modes of the capillary having been calculated to be 22.5 mm for an 800 nm driving pulse. Along with this too, parts of the laser can propagate at angles different to their initial propagation angles. Combined with this, the capillary walls have a reflective boundary condition and so once these differently angled parts of the laser pulse hit the capillary walls and reflect off them they then pass along the radius again and through the centre to the capillary walls at the other side. This can then lead to increases and decreases in on-axis laser intensity that appear unexpectedly but are just these parts of the laser passing through the centre as they propagate at their different angles.

Discussing the blueshifting observed in Figure 6.5(d) in more detail, the refractive index decreases rapidly in time because of the rapidly increasing ionisation and free electron density at the leading edge of the laser pulse, resulting in a blueshift to the laser spectrum [115]. In addition to this, the radial dependence of the laser intensity results in a radial dependence on the free electron density and thus refractive index, plasma defocusing, and blueshift too. As the radial positions closer to the capillary centre

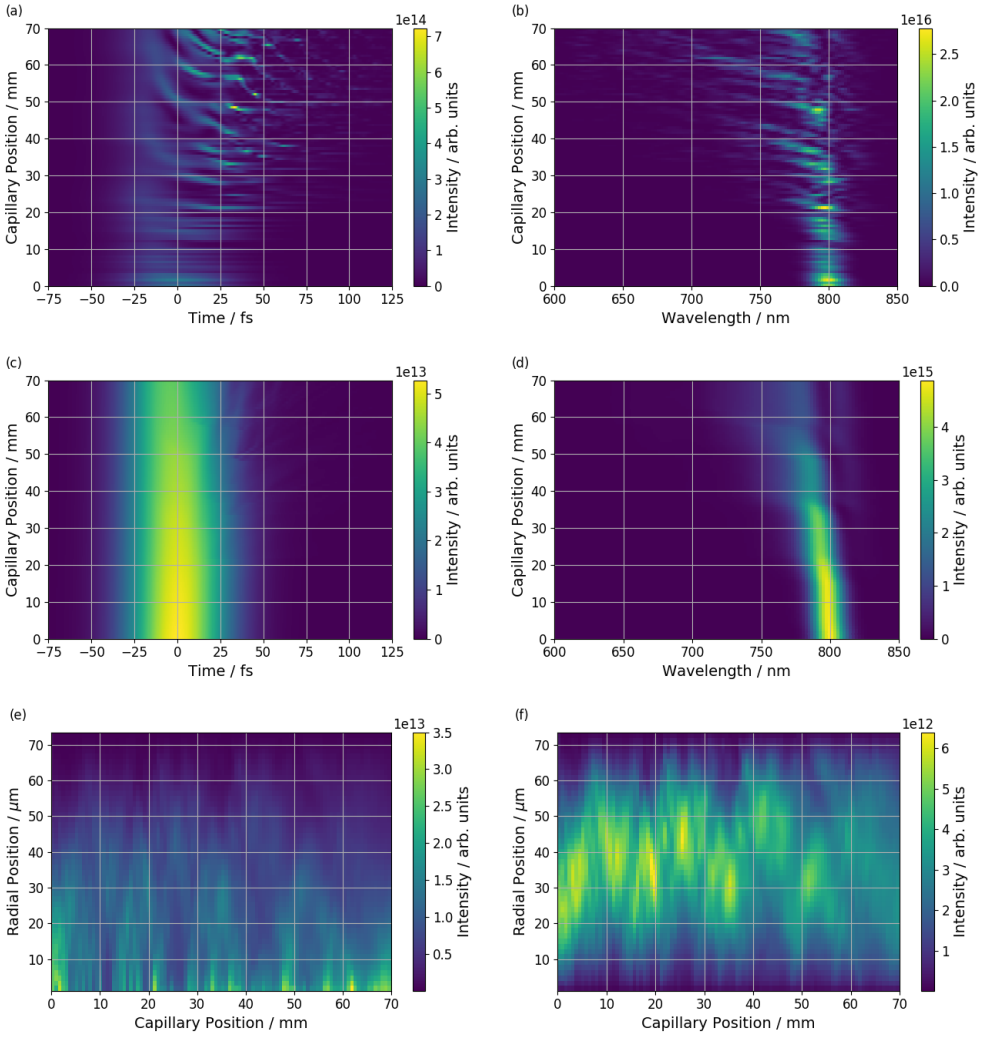

FIGURE 6.5: Laser profiles of a laser pulse from the Ti:Sapph laser system as it propagates through a capillary, for (a) on-axis temporal, (b) on-axis spectral, (c) radially integrated temporal, (d) radially integrated spectral, (e) radial, and (f) radially weighted profiles.

typically experience higher laser intensities they undergo larger blueshifts and plasma defocusing, which also reduces these laser intensities and so decreases the blueshift they subsequently undergo. The blueshifting and plasma defocusing also depend on the mode beating of the laser as this causes the laser intensity to periodically increase, giving positions along the capillary at which the laser intensity is large enough to cause more significant blueshift. This mode beating also can cause the laser at off-axis radial positions to have enough intensity to experience blueshifts and plasma defocusing too, though to lesser extents than for the highest laser intensities. Overall, this then results in the observed blueshifting that occurs in stages along the capillary and to a lesser extents than the on-axis case.

The harmonics generated throughout the capillary that result from the Ti-Sapph laser, shown in Figure 6.6, are quite distinct along most of the length of capillary, with their

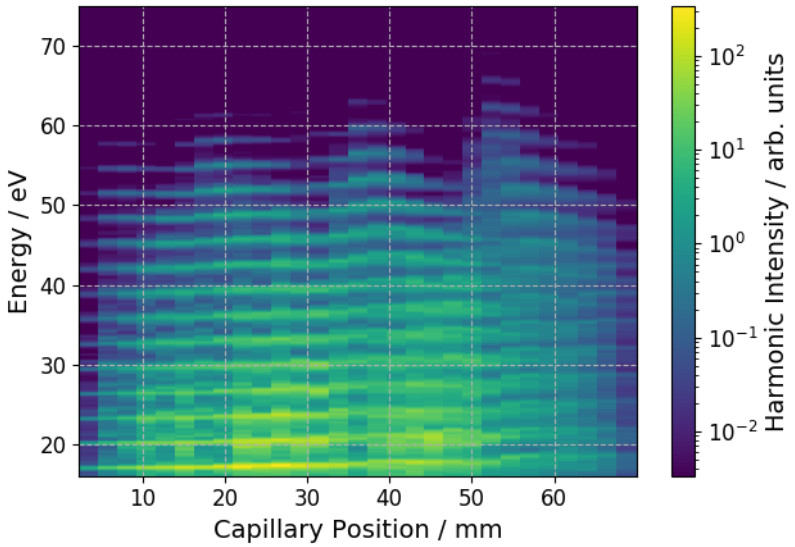

FIGURE 6.6: The high harmonic generation at different positions along the capillary for the Ti:Sapph laser system.

clarity starting to diminish by the final 2 cm. Lower amounts of HHG are observed at the beginning and end of the capillary due to the gas pressure not being at a maximum in the first and last 2 cm of the capillary and so the resulting harmonics generally have a reduced intensity compared to those from the central 5 cm of the capillary. There are also variations in the energies that each harmonic is being generated at, with there being a tendency for each harmonic to shift slowly to higher energies along the length of the capillary, and that shifting increasing more so in the final 2 cm. Whilst the tendency is for the harmonics to shift to higher energies, there is also some oscillation to it. This is most prominently seen in the final 2 cm of the capillary, where some of the higher energy harmonics shift to slightly lower energies. The shifting is due to the spectral profile of the laser pulse undergoing nonlinear distortions as it propagates through the capillary, as seen in Figure 6.5(d), with blueshift causing the harmonics to shift to higher energies and broadening resulting in some harmonics having small shifts to lower energies.

The radial profile of the laser pulse, Figure 6.5(e), shows that the strongest laser intensities are primarily found within the first 10 μm of the radius from the capillary centre. These intensities are not constant across the length of the capillary and instead appear very briefly for only 1 or 2 mm at a time. From these peaks in on-axis laser intensity we would expect the laser conditions at these positions to give rise to increased HHG, with these main peaks being at just over 2.2, around 3 - 4, just under 5 cm, and just over 6 cm along the length of the capillary. When examining the harmonic generation profile in Figure 6.6 we see increases in harmonic intensity for all but the final position. Here though the increases do not occur equally for all harmonic energies, with the increase

between 3 - 4 cm along the capillary being for higher harmonic energies than for those at just over 2.2 cm and just under 5 cm.

The radially weighted laser profile, Figure 6.5(f), also tells an interesting story. Peaks occur regularly, due to mode beating of the laser pulse, though these peaks do not occur at the same radial position and instead oscillate from around 35 μm to 45 μm and back. These peaks can only be faintly seen in the radial profile plot and so do not correspond to the highest energies harmonics being generated, though they generate the large proportions of the lower energies harmonics. The close to centre peaks found in the radial profile appear faintly in the radially weighted profile and so contribute to the HHG, particularly for the higher energy harmonics which need the higher intensity laser pulses to be generated. The lower energy harmonics that are generated at further out radial positions typically make up a large proportion of the overall lower energy harmonics due to the 3D nature of the capillary. This is since at each distance along the length of the capillary there is a circular surface that cuts through the capillary. A line sweeping around this surface at a given radial distance sweeps through less atoms at radial positions closer to the centre and more atom at radial positions further from the centre. The number of atoms at different radial positions is therefore not constant and as the harmonic generation at a given radial position depends on the number of atom present, provided the laser conditions allow for HHG, further out radial positions result in large radial contributions to the HHG, relative to the more central radial positions. Considering the laser intensity typically decreases quickly moving along the radial position, radial positions closer to capillary centre will generate the full range of potential harmonic energies whilst further out radial positions will generate only the lower energy harmonics, though at larger intensities, and so the radial contributions to the HHG increase the generation of the lower energy harmonics, relative to the higher energy harmonics. This is seen in Figure 6.6, though is also a general result that is true for all the laser systems examined. Additionally, since there is typically a lower cutoff for further out radial positions but more contributing atoms, the integrated harmonic spectrum over the cross-section at a given position along the length of the capillary no longer has the flat harmonic plateau as seen in single atom calculations and instead develops the slope in harmonic plateau as seen in Figure 6.1.

It is hard to see from just the radially integrated temporal and spectral plots on their own what insights there may be to guide HHG design, though the on-axis, radial, and radially weighted plots are better for this. As already mentioned, the laser intensities in the on-axis profiles peak at the very start of the capillary and around 2, 3 - 4, and just under 5 cm into the capillary, as well as smaller peaks in the final 1 cm. These peaks correspond to increases in HHG intensities and energies and so HHG design can be guided using this by reducing capillary lengths to take advantage of these on-axis laser peaks [24]. The laser peaks within the first and last 2 cm of the capillary do not result in significant increases to HHG due to the reduced gas pressures here. There are

also many peaks, both temporally and spectrally, at the same capillary position in the last 2 cm of the capillary due to laser pulse break up. These also reduce the HHG and its clarity due to a decrease in coherence with each other due to their many temporal generation positions and also their wide range of driving wavelengths. The laser peak at just before 5 cm into the capillary is very narrow and bright, both temporally and spectrally, and results in a source of clear and improved harmonic generation. The spectral peak at just after 2 cm along the capillary is also very narrow though in this case time temporally there is no narrow peak coinciding with it and instead the laser pulse spans a little over 75 fs though there is also increased harmonic generation for it too. If just either the temporal or spectral on-axis profile is used on its own then it becomes harder to accurately predict improvements to HHG as a peak present in one representation may not correspond to a peak, or other suitable conditions, in the other representation. Therefore they need to be used together. However, a singular peak at a given capillary position in the spectral profile is likely to correspond to distinct and clear harmonic generation due to the narrow spread in the driving wavelength there, and if the temporal profile at this position has not experienced a lot of break up or other pulse effects then HHG is still improved for this position.

In the radially integrated spectral plot, the laser profile broadens and blueshifts as the laser propagates along the capillary. Due to this we see the harmonics shift from their expected energies based on the initial 800 nm central wavelength of the driving pulse to energies based on shorter driving wavelengths. We see the harmonics becoming less distinct and clear as the range of driving wavelengths increases with capillary length, increasing the different energies the harmonics are being generated at. Another interesting observation is that changes in the driving wavelength of the radially integrated spectral profile occur in steps, with there being just small amounts of change for 1 - 2 cm of propagation followed by quick changes over a handful of mm. The regions within the capillary where there are these small changes also correspond to lower laser intensities in the radial profile and also shifts to peaks at further out radial positions for the radially weighted profile. This then suggests that this repeating pattern of slow spectral changes followed by quick changes is due to the mode beating of the laser pulse. These oscillations are also seen in the maximum harmonic energy generated, as well as in the harmonic intensity for lower energy harmonics. Here the maximum harmonic energy with significant generation is at around 65 eV.

Similar to the on-axis profiles, using the radial and radially weighted profiles of the laser pulse, HHG design can be improved by reducing the capillary length to take advantage of peaks in these profiles.

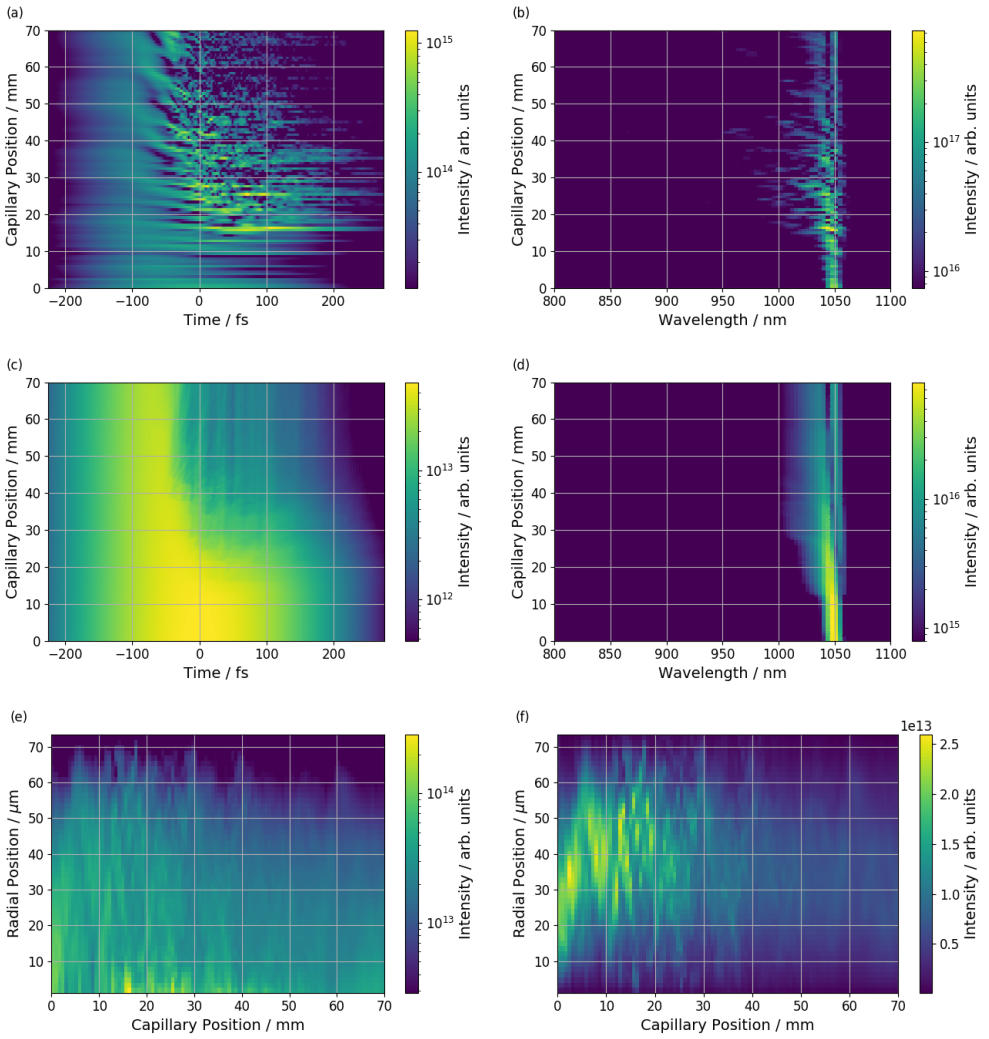

FIGURE 6.7: Laser profile of a laser pulse from the Yb-fibre 1 laser system as it propagates through a capillary, for (a) on-axis temporal, (b) on-axis spectral, (c) radially integrated temporal, (d) radially integrated spectral, (e) radial, and (f) radially weighted profiles.

6.3.2 Yb-Fibre 1 Laser

The temporal and spectral, on-axis and radially integrated laser intensity profiles of the Yb-fibre 1 laser are given in Figure 6.7, as are the radial and radially weighed profiles. The resulting harmonic generation due to this laser system is given in Figure 6.8.

Whilst the on-axis profiles of the laser are initially Gaussian coupled optimally into the capillary fundamental mode, they experience significant nonlinear distortions after around 1.5 cm of propagation in the capillary. Both temporally and spectrally, narrow high intensity peaks are also formed in the capillary after this initial 1.5 cm of propagation.

Observing Figure 6.8, there is a greater range of harmonic energies generated using the Yb-fibre 1 system than for the Ti:Sapph laser system, with the energies reaching up

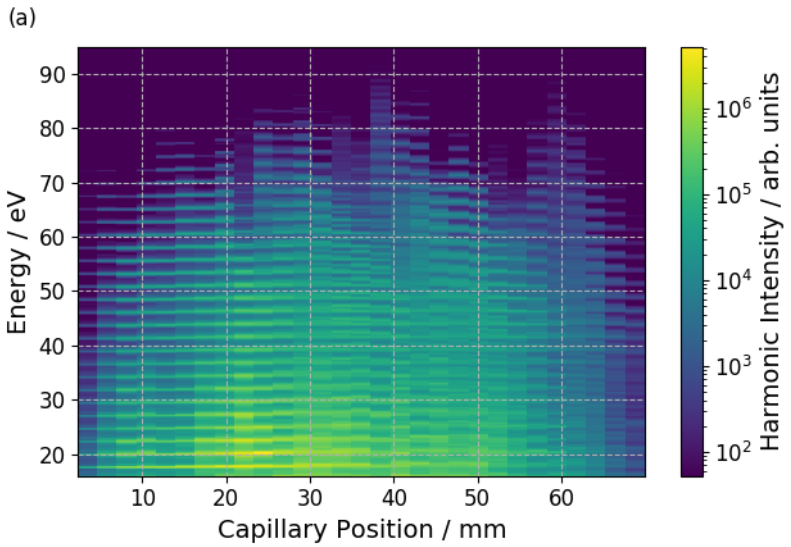

FIGURE 6.8: The high harmonic generation at different positions along the capillary for the Yb-fibre 1 laser system.

around 90 eV. There is also an increase in the harmonic intensities by over four orders of magnitude when again compared to the Ti:Sapph laser system.

The 220 fs pulse width of the laser is the widest of all the laser systems under consideration, though due to the fast breakup and compression of the on-axis pulse in the capillary, the pulse quickly becomes significantly different to this. This compares to the radially integrated temporal laser profile that remains relatively unchanged for the first 1.5 cm of propagation in the capillary, after which the latter two thirds of the pulse experience large nonlinear distortions and breakup whilst the front third continues to remain relatively unchanged due to the lower laser intensities here experiences less distortions. On-axis there are many narrow bright peaks, with a tendency for the same capillary position to contain multiple ones. The peak between 1.5 - 2 cm is however a single continuous peak, albeit spanning a wide time. A local increase to the maximum harmonic energy being generated is present at around this position though it is less than the overall maximum harmonic energy generated. This is due, at least in part, to the reduced gas pressure at this position. The other peaks present do also generally correspond to increases in harmonic generation though the pattern is harder to distinguish than for the Ti-Sapph system as there is much more nonlinear distortion experienced by the laser pulse.

The on-axis spectral profile of the laser shows nonlinear distortions after the first 1.5 cm of propagation, with it undergoing both blueshift and broadening. As mentioned, there is one bright on-axis spectral peak between 1.5 - 2 cm in the capillary. This coincides with the temporal peak and as mentioned together these give a local increase to the generation of harmonics. The radially integrated spectral profile also undergoes these effects though to a lesser extent. These changes again start to take effect after around

1.5 cm into the capillary, where the gas pressure begins to quickly ramp up, reaching its maximum value of 150 mbar at 2 cm along the capillary. This increasing gas pressure increases the nonlinear distortions of the laser pulse. Whilst the radially integrated spectral intensity does significantly decrease over the length of the capillary and there is broadening, the central driving wavelength only shortens to around 1025 - 1030 nm. Combined with the temporally radially integrated profile, clear harmonics are generated along the length of the capillary, shown in Figure 6.8. This is as the front third of the radially integrated temporal pulse remains relatively unchanged along the length of the capillary whilst still having HHG-generating intensities. The spectral profile is also only undergoing a small amount blueshift and so these provide conditions for the generation of clear harmonics. There is also some small variability in the energies of the generated harmonics, though to a lesser extent than for the Ti:Sapph result.

As expected from the on-axis profiles, in the radial profile there are a handful of short bright peaks, all of which are very close to the centre of the capillary. From the radially weighted profile, higher energy harmonics are generated when the weighted laser intensity increases close to the radial centre, with this being at around positions 1.5, 2.5, 3.5 cm etc along the capillary. The intensities of the lower energy harmonics increase when the weighted laser pulse at further out radial positions increases, around capillary positions 1, 2, 3, 4 cm etc. These are again due to the radially-dependent mode beating of the driving laser pulse. For this 1050 nm driving wavelength laser system, the beat length between the fundamental and first modes of the capillary has been calculated to be 17.1 mm. With the increased distortions of the laser pulse as it propagates, the mode beating is less obvious than for the Ti-Sapph system though with a 1 cm period.

6.3.3 Yb-Fibre 2 Laser

The on-axis and radially integrated temporal and spectral intensity profiles of the Yb-fibre 2 laser system are given in Figure 6.9. The resulting harmonic generation is given in Figure 6.10.

Here the laser profiles are significantly different to those from the Yb-fibre 1 laser system in Figure 6.7. This is due to the pulse width reducing from 220 to 25 fs resulting in the initial laser pulse peak intensity being greater than for the Yb-fibre 1 system despite the reduction in average energy from 4 to 2 mJ, increasing the rate at which the laser pulse experiences nonlinear distortions. The highest intensity temporal peak of the laser within the capillary is around five times larger than that in the equivalent Yb-fibre 1 laser figure, though spectrally it is instead around an order of magnitude less in intensity.

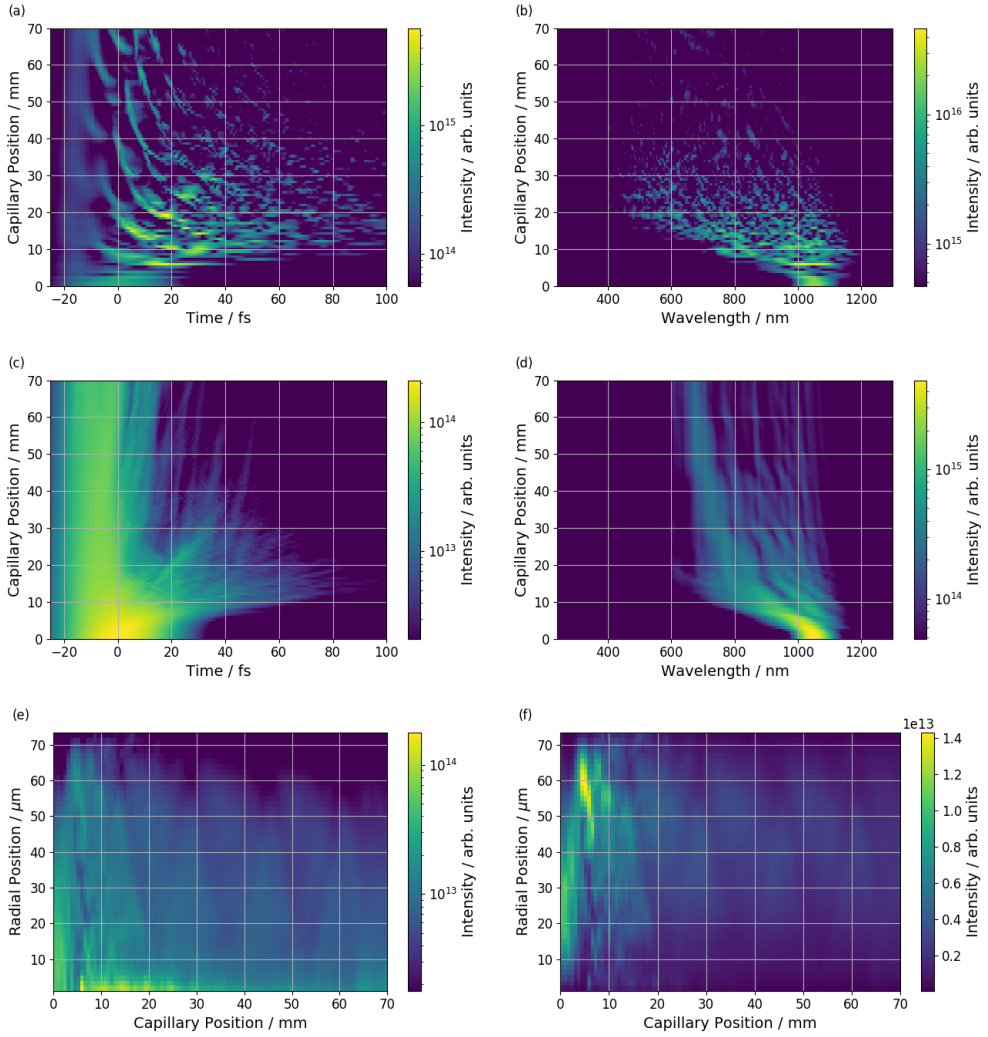

FIGURE 6.9: Laser profile of a laser pulse from the Yb-fibre 2 laser system as it propagates through a capillary, for (a) on-axis temporal, (b) on-axis spectral, (c) radially integrated temporal, (d) radially integrated spectral, (e) radial, and (f) radially weighted profiles.

For the harmonic generation, as shown in Figure 6.10, there is again a greater range of harmonic energies and intensities generated than for the Ti:Sapph system, with the energies reaching up around 90 eV for the Yb-fibre 2 laser system and intensities increased by over four orders of magnitude. Going from the first Yb-fibre system to the second, Figure 6.10(a) to Figure 6.8(b), harmonics are still being generated though their lines are noticeably less distinct and the harmonic energy they are generated at vary more. Some harmonic structure starts to appear for the higher energy harmonics past around 3 cm into the capillary.

The on-axis laser profile shows two large peaks in the temporal domain, the first at around 0.5 cm and the second at 2 cm into the capillary. Here this second peak is very narrow with a width of just a handful of fs, which is considerably narrower than the initial laser width of 25 fs. Observing Figure 6.10, we see increased generation of

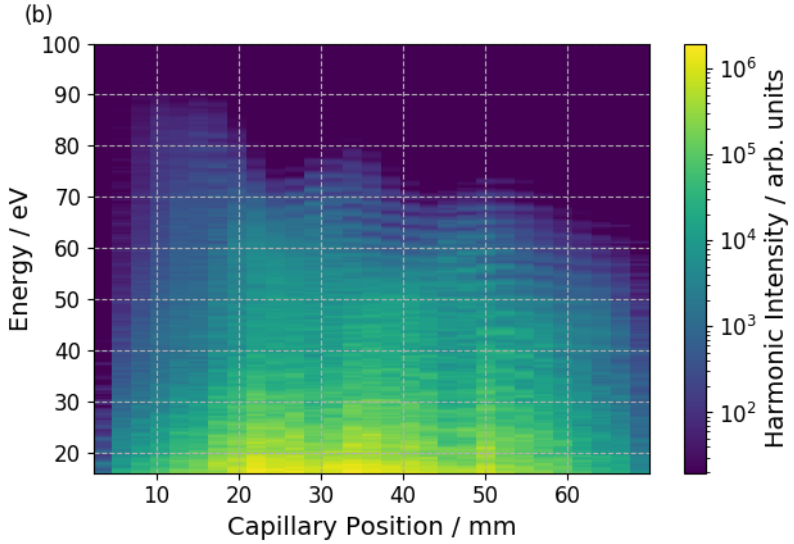

FIGURE 6.10: The high harmonic generation at different positions along the capillary for the Yb-fibre 2 laser system.

maximum harmonic energies during these first 2 cm of the capillary. The harmonic generation however does not have clear harmonics present, due to the wide range of the driving wavelengths between 450 - 1050 nm.

Both the on-axis and radially integrated spectral profiles of the laser undergo large amounts of broadening and blueshift. As with the spectral plots of the previous laser systems, these effects are much more prominent for the on-axis profiles due to this typically being the radial position experiencing the highest laser intensities. The radially integrated pulse at the end of the capillary has a spectrum ranging from 650 - 950 nm. Rather than it being a continuous range, there are distinct bands of driving wavelengths, with the main one being at around 675 nm and fainter ones being at, for example, 780 and 850 nm. The bands quickly shift from the initial driving wavelength early on in the capillary though soon after their shifting starts to decrease as they approach their wavelengths as seen at the end of the capillary. All these drive the HHG and as a result there is a combination of clear harmonics not correlating to the initial driving wavelength of the laser and harmonic generation with a lack of structure. Early in the capillary, over approximately the first 2 cm, these driving wavelength bands form a reasonably continuous range of driving wavelengths causing the HHG in this region of the capillary to not have clear structure. It is after this as these bands begin to separate that structure to the harmonics improves.

The front half of the radially integrated temporal profile remains relatively unchanged throughout its propagation along the capillary whilst the latter undergoes nonlinear distortions and breaks up after approximately the first 0.5 cm of propagation. Due to this, a lot of the harmonic generation results from the front half of this pulse.

For the radial profile, the majority of the intensity is close to the radial centre, with some faint intensities across the radius, particularly for the first 1 cm along the capillary. Radially weighted, 0.5 cm into capillary there are expected to be significant contributions to the HHG from close to the capillary edge due to the increased intensity of the weighted laser here. We would expect these to be for low energy harmonics due to the laser intensities being very small here. However, we do not see increased HHG at 0.5 cm into the capillary due to the reduced gas pressure here limiting the HHG possible. There are contributions to the HHG from across all the radial width within the first 2 cm of the capillary. For these we see high and low energy harmonics being generated as the larger laser intensities close to the centre of the radius generate higher energy harmonics whilst those from further out along the radius generate the lower energy harmonics. After that we see a faint pattern repeating every 1.75 cm in the radially weighted laser profile due to the mode beating of the laser. Over 1.5 - 2.75 cm there is an increased laser intensity from 40 - 70 μm along the radius, then over 2.25 - 3.25 cm from 20 - 50 μm, with this patter then repeating over the rest of the length of the capillary. As a result of this we observe increases in harmonic intensity for lower energy harmonics over the 1.5 - 2.75 cm capillary positions due to the lower laser intensities here, and then increases in higher energy harmonics over 2.25 - 3.5 cm due to the higher laser intensities here, with this pattern repeating along the rest of the capillary.

6.3.4 Yb-Fibre 3 Laser

The on-axis and radially integrated, temporal and spectral profiles of the Yb-fibre 3 laser pulse system are given in Figure 6.11, as are the radial and radially weighted profiles. The resulting harmonic generation is given in Figure 6.12.

This laser system has the narrowest pulse width of all three Yb-fibre systems, as well as all the laser systems under investigation overall. This system has a 7 fs pulse width, which compares to 220 and 25 fs for the other two Yb-fibre systems. This is 31 and 3.6 times narrower respectively and results in an initial peak intensity greater than that for those other two systems. The effect of this is that the Yb-fibre 3 system experiences much more laser pulse nonlinear distortions much sooner than in the other systems, as is seen in the figures.

For the resulting HHG of this system, Figure 6.12, there is a slightly greater range of harmonic energies generated than for the Ti:Sapph system, with the energies reaching up around 75 eV, and again an increase in the harmonic intensities by over four orders of magnitude. The harmonics generated from all three Yb-fibre laser systems have intensities comparable to each other, depending on the harmonic energy and capillary position under consideration. From this final Yb-fibre system the harmonics are the least distinct. This is due to the laser pulse for this system having the largest distortion, which results in harmonics being generated from many different driving wavelengths

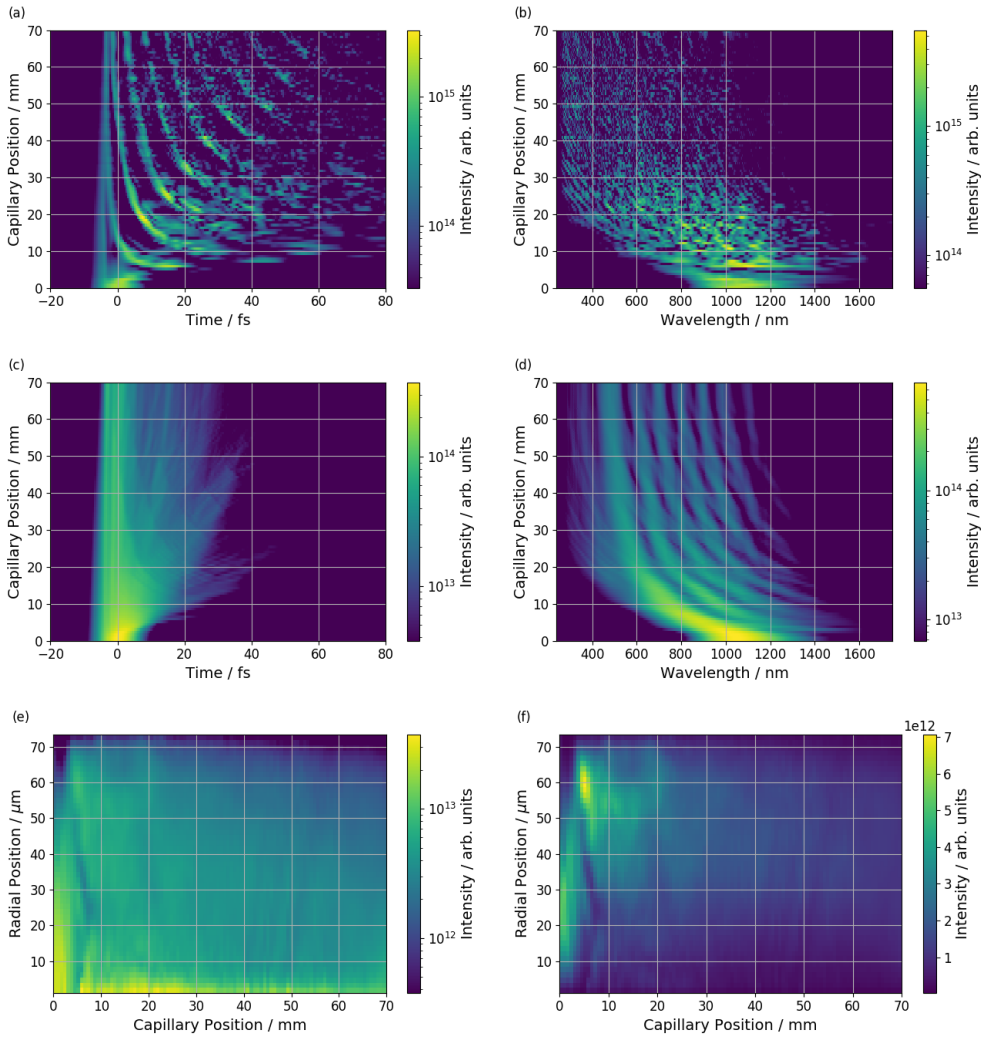

FIGURE 6.11: Laser profile of a laser pulse from the Yb-fibre 3 laser system as it propagates through a capillary, for (a) on-axis temporal, (b) on-axis spectral, (c) radially integrated temporal, (d) radially integrated spectral, (e) radial, and (f) radially weighted profiles.

and so becoming less distinct. The pulse widths reduce from 220 to 25 to 7 fs for Yb-fibre 1, 2, and 3 respectively and each successive laser system has a decreasing average energy. However, the decreasing pulse widths counter the decreasing average laser energies, which then results in each of these successive systems having a greater intensity than the previous one. All this culminates in increased amounts of nonlinear distortions to the laser pulse, temporal breakup and spectral blueshift going from Yb-fibre 1 to 2 to 3. This in turn reduces the conditions for favourable HHG, resulting in the generation of less clear and less distinct harmonics, which is observed when considering the HHG figures for all three Yb-fibre systems together.

Again, the front of the temporal radially integrated pulse remains mostly unchanged as the laser pulse propagates along the capillary. The on-axis profile has a recurring pattern with peaks that occur approximately every 0.5 cm which also appear at later

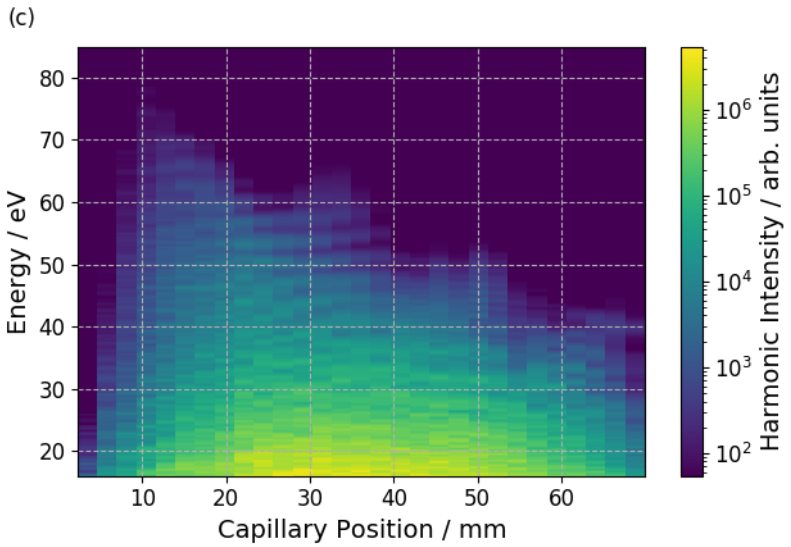

FIGURE 6.12: The high harmonic generation at different positions along the capillary for Yb-fibre 3 laser system.

and later times with each one appearing round 10 - 15 fs later than the previous one. These are due to a mixture of mode beating, pulse nonlinear distortions and the parts of the laser propagating at angles not along the axis of the capillary though further study is needed to understand them better. Whilst we would expect to see increases in the maximum HHG energies at these peaks due to the increased driving laser intensity of these points increasing the maximum possible HHG energies, in Figure 6.12 we do not see increases in the HHG that correspond to this, suggesting that the main contributions to the HHG come primarily from off-axis but also from the on-axis temporal front of the laser pulse rather than these peaks. Similar to the radially integrated temporal profiles of the previous laser systems, the front of the laser pulse remains relatively unchanged throughout the capillary, with the rest of it experiencing significant nonlinear distortion. There are also faint intensities around positions and times similar to the diagonal on-axis peaks and so this would imply other radial positions close to the capillary centre have similar profiles too.

Spectrally, the on-axis profile breaks up the fastest out of all other laser systems due to the high peak intensity of this laser pulse causing large amounts of nonlinear distortions. The result of this is that it very quickly develops a spectral range from less than 400 nm up to 1200 nm, depending on the capillary position. The radially integrated spectral profile breaks up quickly too, with a pattern similar to the on-axis temporal profile forming, with there being bands of increasing and decreasing laser intensity that initially quickly shift to smaller wavelengths but with this shifting gradually reducing such that over the last few cm of the capillary their wavelengths do not change much. As this is so similar to the on-axis temporal pattern they are likely to be related though further study is still needed.

For the radial laser profile, over the first couple of mm into the capillary the laser intensity spans from the centre up to 30 - 40 μm. After this some faint intensities for radial positions remain though to a much less extent, with the laser intensity being by far the largest close to the radial centre for the remainder of the capillary. The radially weighted profile shows that over the first 1 cm of the capillary there are strong HHG contributions along 10 - 50 μm of the radius, as well as from the peak at 60 μm. After this radially weighted intensities remain along the radius of the capillary though there is no obvious oscillating pattern for this laser system. For the most part this is also true of the resulting harmonic generation, though there are four peaks in the maximum harmonic energy at 1, 3, 5, and 6.5 cm along the capillary. Here only the first has a clear cause when examining the radially weighted laser profile, with the other three peaks in harmonic energies not having a distinct cause from this laser profile representation. There are faint intensities close to the radial centre throughout however, with these being largest earlier on in the capillary and then decreasing. These result in the higher energy harmonics being generated earlier on in the capillary, with the maximum harmonic energy generated decreasing with with capillary position after the peak at 1 cm.

6.3.5 Mid-IR OPCPA Laser

The laser pulse profiles of the Mid-IR OPCPA system is given in Figure 6.13 and the resulting high harmonic generation is given in Figure 6.14.

Both the on-axis and radially integrated profiles show only small changes to the pulse as it propagates through the capillary due to the peak intensity of the laser pulse being too low for significant nonlinearities. There is also not any temporal breakup present during the pulse propagation and very little change to the central driving wavelength. The on-axis, radial, and radially weighted profiles show that mode beating is present, whilst the radially integrated profiles do not, due to energy conservation. For this 1700 nm driving laser, the beat length between the fundamental and first modes of the capillary has been calculated to be 10.6 mm.

Figure 6.14 gives the high harmonic generation as seen from their generation positions within the capillary for the Mid-IR laser system. Here the Mid-IR system produces significant amounts of harmonic generation up to energies of 70 eV, corresponding to the classical cutoff of 69 eV for the initial pulse of this system. The harmonics generated are clear and distinct throughout the length of the capillary, though due to the longer driving wavelength the energy spacing between the harmonics is very small when compared to the other laser systems. The intensities generated are also significantly less than than those for the other laser systems. The HHG for this laser system depends a lot on the mode beating. This is due to it being the largest effect present on the laser intensity, with the peaks in laser intensity giving rise to corresponding peaks in harmonic energies and intensities due to the laser intensity dependence of HHG.

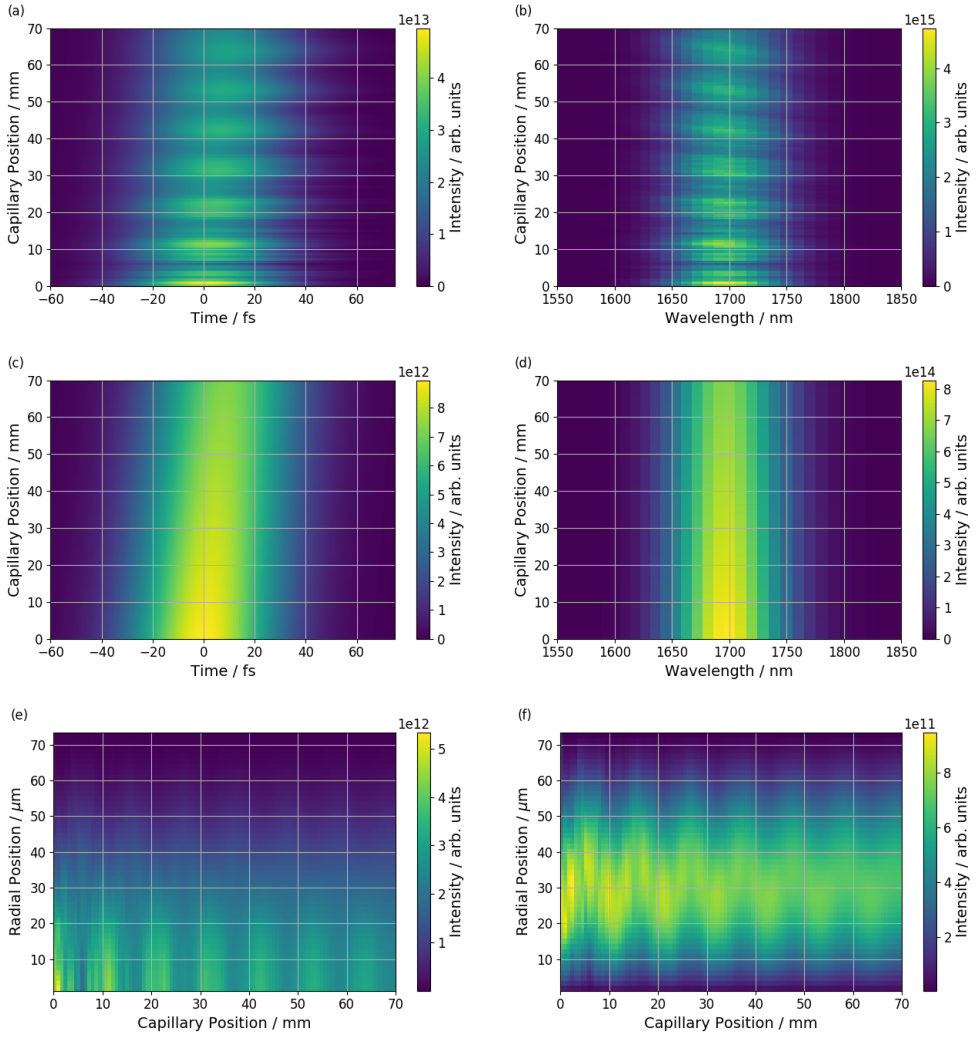

FIGURE 6.13: Laser profile of a laser pulse from the Mid-IR OPCPA laser system as it propagates through a capillary, for (a) on-axis temporal, (b) on-axis spectral, (c) radially integrated temporal, (d) radially integrated spectral, (e) radial, and (f) radially weighted profiles.

The radial laser profile shows clear mode beating occurring along positions 0 - 20 μm of the radius. The radially weighted and integrated profiles show that most HHG contributions come from radial positions between 0 - 55 μm. Similar to some of the previous laser systems, the radial positions of these contributions vary and oscillate over the length of the capillary. From this the intensities for higher energy harmonics are expected to increase between around 0.75 - 1.25, 1.85 - 2.65, 3 - 3.65 cm along the capillary, etc and the lower energy harmonics increase between around 1.25 - 1.85, 2.5 - 3, 3.5 - 4 cm, and so on, along the capillary. The higher energy harmonic peaks occur at around these positions though the lower energy peaks instead are twice as wide along the length of the capillary than expected. This is due to the lower energy harmonics being generated from the laser intensity peaks that are both further out along the radius and also closer to the radial centre, whereas the higher energy harmonics are only generated from those laser intensities closer to the radial centre. Overall, the mode beating is

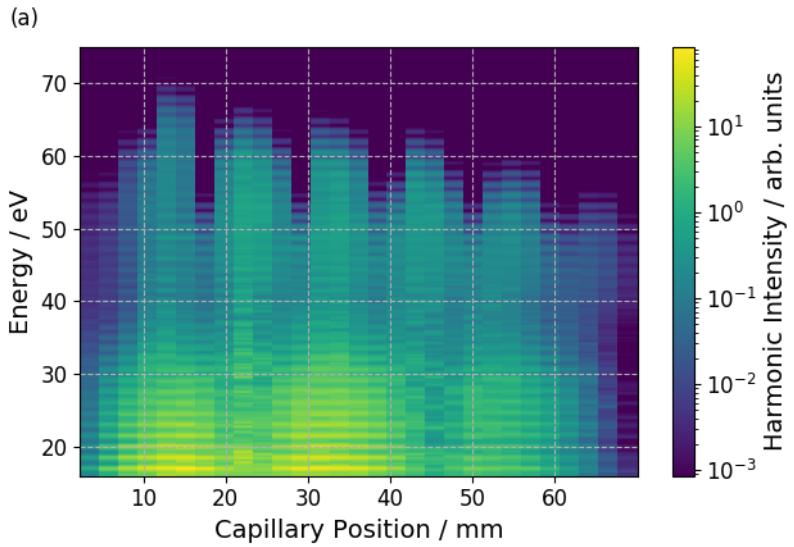

FIGURE 6.14: The high harmonic generation at difference positions along the capillary for the Mid-IR OPCPA laser system.

the largest contributor to the effects seen in the harmonic generation. As discussed before, this is due to the laser having relatively low power and therefore only undergoing small amounts of nonlinear distortion.

6.3.6 Tm-fibre Laser

The laser profiles of the Tm-fibre laser are given in Figure 6.15 and the resulting high harmonic generation is given in Figure 6.16.

The on-axis, radial, and radially weighted laser profiles show mode beating is the major effect present, with the beat length between the fundamental and first modes of the capillary having been calculated to be 9.0 mm for this 2000 nm wavelength driving laser. Much like the previous laser, except for the mode beating, there are not many effects present in the capillary laser propagation. This is due to the temporal intensities of these two laser systems being significantly smaller than those for the other lasers, leading to significantly less nonlinear distortions of the laser pulse.

Figure 6.16 gives the high harmonic generation resulting from the TM-fibre laser system. The Tm-fibre produces harmonics up to energies of around 110 eV, corresponding to energies just above the classical cutoff of 103 eV. The harmonics generated are clear and distinct throughout the length of the capillary, and again, due to the longer driving wavelengths of this system the energy spacing between the harmonics is very small when compared to the other laser systems. The intensities generated are also again significantly less than than those for the first four laser systems.

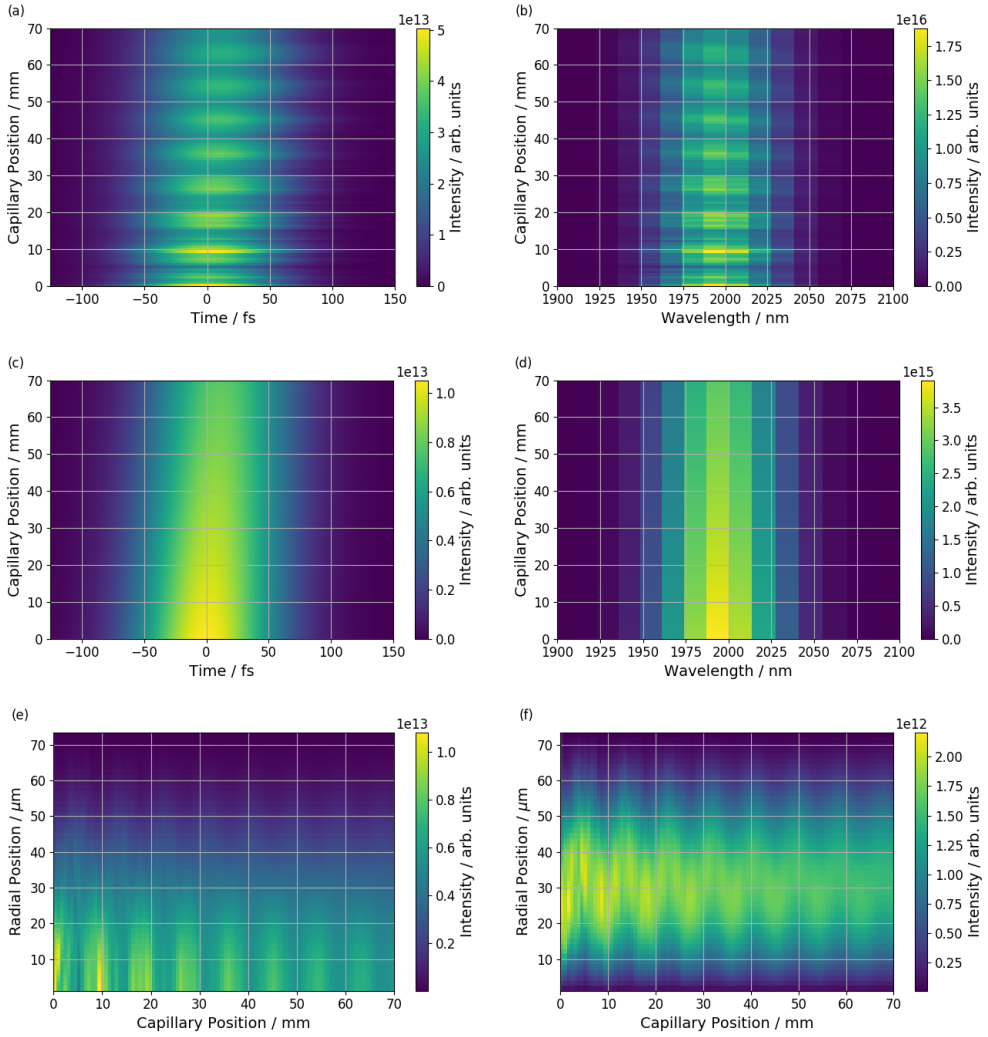

FIGURE 6.15: Laser profile of a laser pulse from the Tm-fibre laser system as it propagates through a capillary, for (a) on-axis temporal, (b) on-axis spectral, (c) radially integrated temporal, (d) radially integrated spectral, (e) radial, and (f) radially weighted profiles.

Similar to the Mid-IR laser system, the radial profile of the TM-fibre system has reasonable amounts of laser intensity present along 0 - 50 μm of the radius. There are also qualitatively comparable similarities to the radially weighted profile too, with it resulting in regular increases in large contributions to the higher energy harmonics from positions 17.5 - 35 μm along the capillary radius and with a periodicity of around 1 cm along the capillary length. For the lower energy harmonics this periodicity is again longer than for the higher energy harmonics and is due to the lower energy harmonics being generated from both the further out radial positions and those closer to the radial centre. Larger HHG intensities occur earlier in the capillary as both the on-axis and radially integrated laser intensities decrease due to absorption as the laser propagates through the capillary.

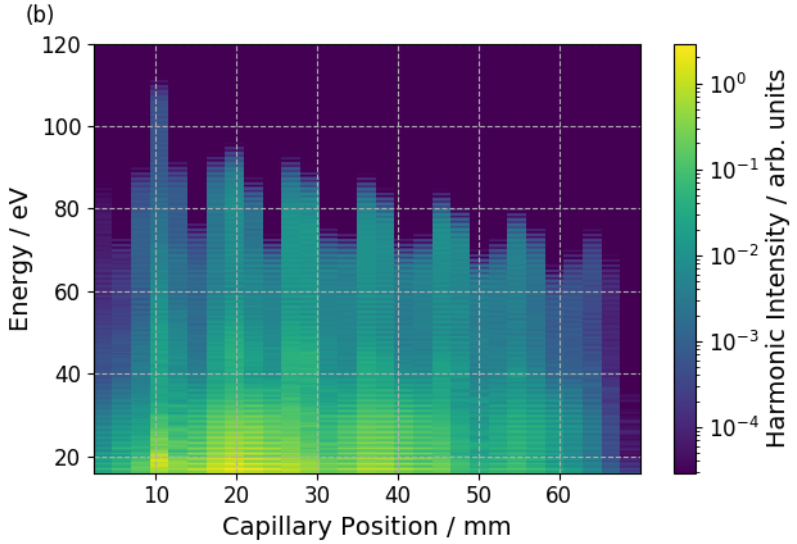

FIGURE 6.16: The high harmonic generation at difference positions along the capillary for the Tm-fibre laser system.

6.4 High Harmonic Generation for Different Length Capillaries

Using the high harmonic generation results of the previous section, Section 6.3, an additional postprocessing step can be performed to transform the harmonic generation as seen throughout a 7 cm length capillary to the harmonic generation of different length capillaries ranging from a couple of mm up to the original 7 cm. The aim of this is to gain insights into how different capillary lengths will affect the harmonic generation for the six different laser systems simulated. This can then be used to improve capillary design and choices of laser systems for HHG to increase either the intensities of generated harmonics or their maximum energies.

To do this, the harmonic generation from each position along the capillary is forward-propagated to each subsequent position and summed together with the rest of the harmonics propagated to that position to give what would be the harmonic spectrum if the capillary were to suddenly end there. Doing this then gives multiple harmonic spectra each for a different length capillary whilst only needing to do the computationally expensive simulations for just the longest capillary. The gas pressure profile used in these forward-propagations follows that for the 7 cm capillary and so the gas profiles for the shorter capillaries abruptly stop at their given shortened lengths rather than there being a tapering off of gas pressure over the last part of the capillary. The plots produced from this differ from the plots of the previous section that showed harmonic generation in a number of ways. The previous plots showed the harmonic generation as it occurred at the given positions within the capillary whereas here the propagation

of the harmonics throughout the capillary has been included. Due to this there is also then absorption effects present which depend strongly on harmonic energy.

A final postprocessing stage can also be performed on the harmonic generation from the different laser systems in which the harmonics are integrated over a given energy range to give the HHG yield of that range for the different length capillaries. These can then be normalised too to make comparisons between the different lengths easier.

We do this final postprocessing stage by integrating the generated harmonics from the different length capillaries over the harmonic energy range 20 - 45 eV. Then we normalise the resulting harmonic intensity to that of the 7 cm length capillary. This gives the increase (or decrease) in harmonic yield of the different length capillaries relative to the 7 cm length capillary for the 20 - 45 eV energy range. From this we gain clearer insights into how different length capillaries can be used to optimise the harmonic generation and we can also gain the increases expected from this relative to the 7 cm length capillary.

The normalisation of harmonic intensities to that of the 7 cm length capillary was done as that has been the longest capillary under consideration by us and also as it has largely been the length of choice for the capillary harmonic generation work of the Ultra-Fast X-ray group at the University of Southampton [24, 25, 43, 44]. Doing this therefore then helps guide possible future capillary design and HHG improvements. In addition to this, by normalising the energy-integrated harmonic intensities the result is that we get factors of increase and decrease, giving easier to visualise comparisons of potential HHG intensities for different length capillaries.

The harmonic energy integration range 20 - 45 eV is used for two main reasons. The first is that it enables us to make comparisons to the literature for the Ti:Sapph laser system as Butcher et al. [24] used the energy integration range 20 - 62 eV when they obtained their 40 times increase in harmonic yield by changing from a 7 cm to a 4.5 cm length capillary. The second reason for our choice of energy integration range is that our 1D TDSE simulations do not account for the Cooper minimum, a prominent minimum in the HHG spectra centred around 53 eV for argon [56, 118], and so stopping our energy integration range prior to this avoids the effects which we are not able to simulate with our current model. Combining these two reasons together, experimentally there is a significant decrease in the harmonic spectra observed centred around 53 eV which we do not see due to the limitations of our one-dimensional TDSE model. By cutting our harmonic energy integration range short of this effect we better match the experiment and this therefore then allows us to still make fair comparisons to the experiment, particularly the experimental work of Butcher et al [24].

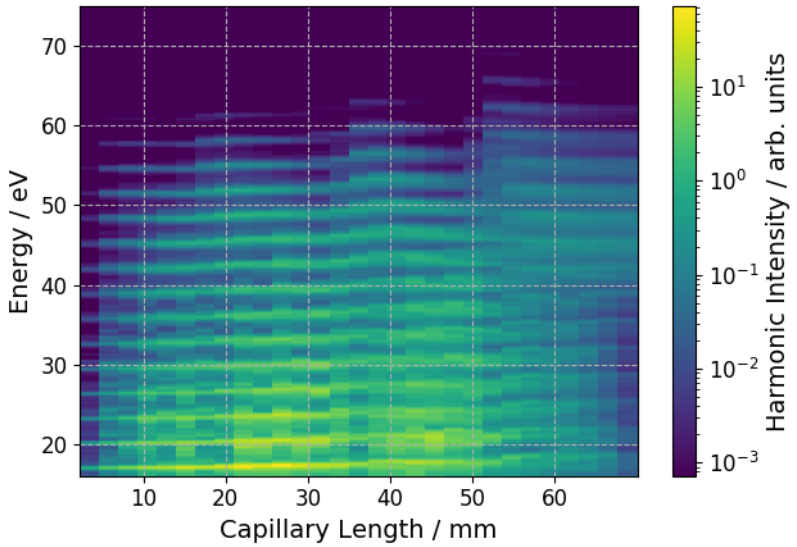

FIGURE 6.17: The high harmonic generation from the Ti:Sapph laser system for different length capillaries.

6.4.1 Ti:Sapph Laser System

Figure 6.17 gives the harmonic spectra generated for different length capillaries using the Ti:Sapph laser system. Here the maximum gas pressure is 150 mbar, with a ramping up to it over the first 2 cm and a ramping down from it over the last 2 cm, as shown in Figure 2.2 of Chapter 2.

Absorption plays a large effect on the harmonic spectra produced. The lower harmonic energies under 40 eV are readily absorbed by the gas and so are only able to propagate a few mm before absorption effects are too great. Therefore, the spectra for these energies are very similar to the spectra of the previous section. For higher energies over 40 eV we see effects of their propagation as they build up and produce streaking lines across different capillary lengths. This is due to the absorption being less for these harmonic energies and so they can propagate further, and noticeable, distances before they are absorbed. The energies the harmonics are generated at change here again too, and for the same reasons as in the previous section. For the higher energy harmonics there is less absorption present and so when their energies vary they propagate and build up causing the harmonics to become less clear and distinct as combined together they are not generating and building up at the same specific energy but instead at a range of energies close together.

The gradual ramp down of the gas pressure does not lend itself to effective HHG conditions, particularly for the lower energy harmonics. This is due to absorption still having a large effect in the ramp down region but the number of atoms present being significantly less. With the reduced number of atoms there is less HHG and so for the lower energy harmonics there is a decrease in harmonic intensity compared to the

shorter length capillaries with abrupt ends to their gas pressure profiles rather than the longer and gradual ramp down. The higher energy harmonics also have a reduced amount of generation in the capillary region where the gas pressure is ramping down. At the same time though they experience less absorption by the gas and thus they can propagate for longer distances. The result is that for capillary lengths ending in this region of ramping down gas pressure, the higher energy harmonics are better at maintaining their intensities compared to the lower energy harmonics and do not show the significant absorption effects that the lower energy harmonics experience.

Inspecting Figure 6.17, decreasing the capillary length to around 4.5 - 5 cm significantly increases the HHG for most of the harmonic energies under consideration, but particularly for energies under 40 eV. This is in agreement with the experimental result by Butcher et al [24] who measured a 40 times increase in the HHG when moving from a 7 cm length capillary of the same design as ours to a 4.5 cm length capillary that had a short sharp decrease in gas pressure over the last 3 mm of the capillary. We also observe here that reducing the capillary length further to 3 cm increases the HHG still for harmonic energies below 40 eV. If instead the capillary is shortened to 5.5 cm it optimises the maximum possible harmonic energy, which for this case would be at 65 eV.

The harmonic increase for different length capillaries when using the Ti:Sapph laser is given in Figure 6.18. Here we again see that the 7 cm capillary is not the optimal design for HHG over the 20 - 45 eV harmonic energy region. As previously discussed, the ramping up and down of the gas pressure over the first and last 2 cm of the capillary is counterproductive to the high harmonic generation. For capillaries of shorter lengths that also follow this 7 cm length based gas pressure profile, there is a reduction in the obtainable harmonic increases when these capillaries end within one of these regions of ramping up or down gas pressure. Also, as discussed previously, the mode beating results in large harmonic increases for 2.5 and 4.5 cm length capillaries.

The 2.5 cm length capillary corresponds to an increase in harmonics of around 35 times compared to the 7 cm capillary, and the 4.5 cm length corresponds to an increase of around 25 times. Butcher et al found a harmonic increase of 40 times for a 4.5 length capillary compared to the 7 cm one [24]. There is a difference between our simulated result and the experimentally measured one though the simulated value is still close to the experimentally measured one with it being 63% of it. When considering the approximations involved in the simulations to be able to perform them in practical amounts of time, this is respectfully close. Additionally to this, both give this harmonic increase for the same capillary length of 4.5 cm too. This shows that whilst the exact values of increase in harmonics may vary between simulation and experiment, the positioning and approximate increase do align well with each other. A 2.5 cm length capillary is then expected to improve the harmonic increase further than the 4.5 cm capillary does as it is shown to give a 40% harmonic increase relative to the 4.5 cm length capillary.

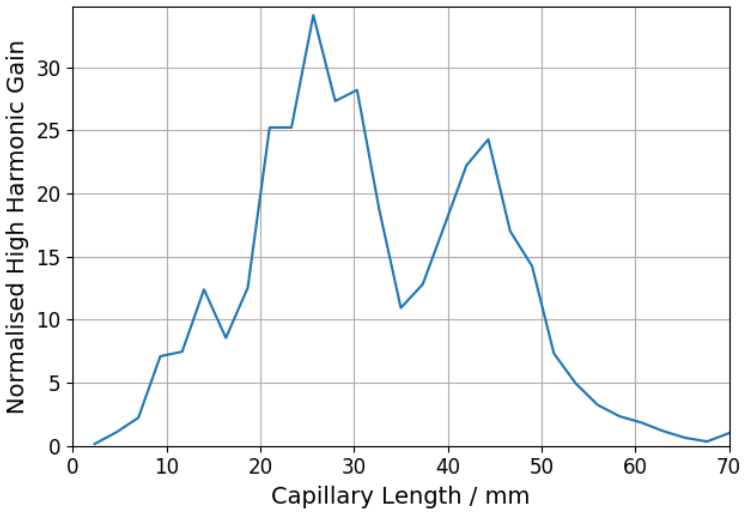

FIGURE 6.18: High harmonic increase for different length capillaries, integrated over the harmonic energy range 20 - 45 eV and normalised to the 7 cm length capillary, when using the Ti:Sapph laser system.

6.4.2 Yb-Fibre Laser Systems

Figure 6.19 gives the HH spectra for different length capillaries for the three Yb-fibre laser systems. As with the different capillary lengths for the Ti:Sapph system, the gradual ramping down of gas pressure over the last 2 cm is not optimal for generating the lower energy harmonics and so shortening the capillary and having a much sharper decrease in gas pressure improves the HHG for these energies. For the higher energy harmonics, there is also a dependence on the conditions of the laser for capillary lengths that end during this region. For example, the Yb-fibre 1 and 2 systems largely maintains the intensities of harmonics generated over 40 eV whilst the Yb-fibre 3 system does not. This is due to the first two systems still generating enough harmonic intensities for capillary lengths ending in this region to counter the absorption whilst the final Yb-fibre system does not.

As mentioned, the harmonic energies below 40 eV for the Yb-fibre systems favour capillaries of shorter lengths with sharper decreases in gas pressure at the capillary end. For the Yb-fibre 2 system we find that reducing the capillary length to 5, 3.5, and 2.5 cm gives noticeable increases to the HHG below 40 eV. This is due to the mode beating of the laser and the high amounts of absorption for harmonic energies below 40 eV which result in the propagated harmonics for this energy range to be very close to the harmonics as generated at those capillary positions, as seen previously in Figure 6.10. For harmonic energies 40 - 50 eV the longer capillary lengths all give similar amounts of HHG whilst reducing the capillary to a 2 - 4 cm in length gives an increased HHG in this energy region. For harmonics between 50 - 60 eV capillary lengths of 5.5 and

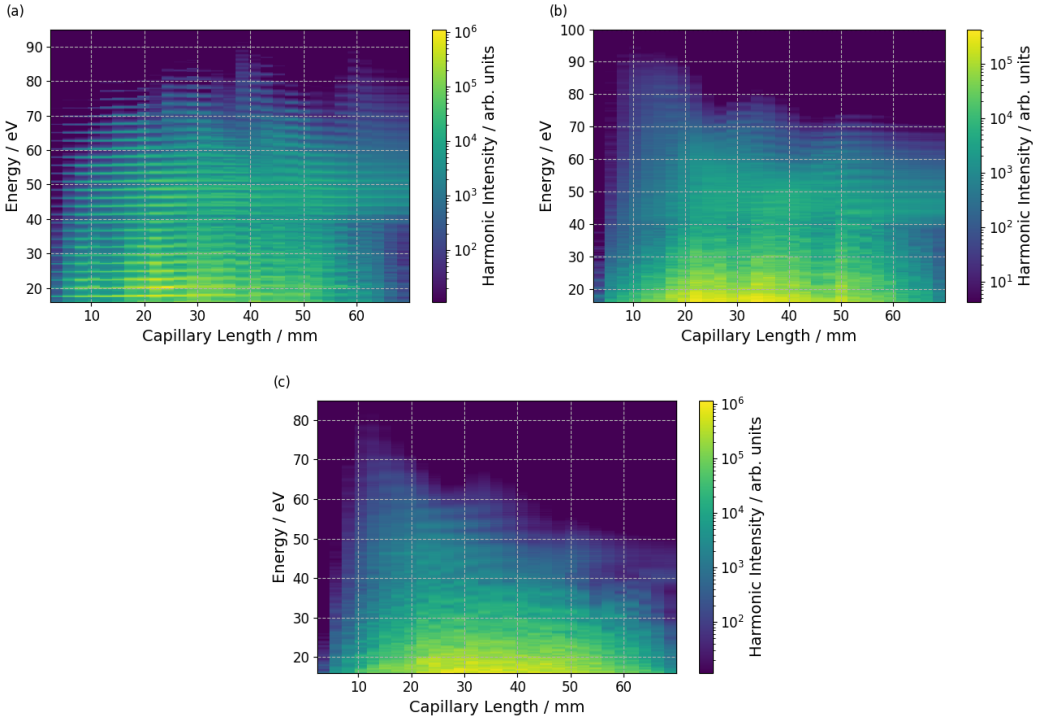

FIGURE 6.19: The high harmonic generation due to the Yb-fibre (a) 1, (b) 2, and (c) 3 laser systems for different length capillaries.

2.5 cm give an increase in HHG as well. For energies over 60 eV, a 6 cm length capillary increases the maximum harmonic energy generated up to around 85 eV, and a 4 cm length capillary gives an increase in the maximum harmonic energy up to just under 90 eV. For the very shortest length capillaries the Yb-fibre 1 system produces very clear and distinct harmonics. Extending the capillary length, these remain clear though due to the longer medium for the laser to propagate in the harmonics become wider and lose some of their clarity. This is due to the harmonics beginning to generate at other energies different from their original ones based on the initial driving pulse wavelength. The effects of the laser mode beating are again seen though for the harmonic energies over 40 eV they are less clear than in Figure 6.8. This is due to the propagation effects for these energies resulting in harmonic intensities being presented for capillary lengths where originally the generation at these positions had dips in harmonic intensity instead.

The effects of the laser mode beating are also seen in the harmonic generation for different capillary lengths using the Yb-fibre 2 laser system, as shown in Figure 6.19(b). Similar to the HHG for different length capillaries using the Yb-fibre 1 system, the effects of this are more prominent for the lower energy harmonics. The maximum harmonic energy generated using this system is slightly more than for the first Yb-fibre system, reaching an energy approaching 95 eV compared to 90 eV. Here though this is generated for a 1 - 2 cm length capillary rather than a 4 cm length capillary as seen for the Yb-fibre 1 system. The harmonics generated here are also less clear than those for

the Yb-fibre 1 system and so whilst similar harmonic intensities are generally obtained it comes at the expense of these less distinct harmonics. This would mean then that when using capillary HHG in both cases if a user desired clear harmonics that are generated at specific and predictable energies then the Yb-fibre 1 laser system would be a more appropriate choice compared to the Yb-fibre 2 system. There is a lack of harmonic structure observable for the shortest length capillaries though this improves going to longer capillary lengths with the harmonic structure being the most clear for a 5 cm length capillary.

The harmonic intensities generated for different length capillaries using the Yb-fibre 3 laser system, as shown in Figure 6.19(c), are comparable to the other two Yb-fibre systems. Here though there is a lack of harmonic structure for most capillary lengths, and similar to that observed in Figure 6.12, the maximum harmonic energy of 80 eV is achieved for a capillary length of 1 cm, after which the maximum harmonic energy decreases and becomes just as little as 50 eV by the end of the capillary. As discussed previously, this is due to the large nonlinear distortions of the laser pulse as it propagates through the capillary reducing the conditions for HHG. Reducing the length to between 2 and 5 cm increases the HHG intensities for the lower harmonic energies below 40 eV. Despite the lack of harmonic structure for most capillary lengths, there are some faint harmonics observed between, for example, 50 - 60 eV for 2 - 4 cm length capillaries. These harmonics shift in their energy and are also wider and further spaced than would be expected from a 1050 nm driving pulse. This is as the driving wavelength for these being smaller than that of the initial laser pulse due to the blueshift that has occurred.

When considering different length capillaries for all three of the Yb-fibre laser systems, the intensities of the lower energy harmonics follow the gas pressure profile due to them being readily absorbed by the gas. This results in the slow ramping down of the gas pressure not being conducive to effective generation of these harmonics. The higher energy harmonics for all three of these laser systems propagate further before being absorbed and so this ramping down of gas pressure has less of an impact on them. However, reducing the capillary lengths still improves the HHG for these energies still. The first Yb-fibre system produces the clearest harmonics, followed in turn by the second and third laser systems. Decreasing the pulse width between each system causes increased amounts of nonlinear distortions to the laser pulse which in turn results in less clarity to the harmonics. This is generally true irrespective of the capillary length. Despite this, comparable harmonic intensities can be gained from each of the Yb-fibre laser systems, depending on the choices of capillary lengths.

The normalised harmonic increase for different length capillaries when using the three Yb-fibre laser systems are given in Figure 6.20. For all three of these results the gas pressure profile once again plays a large effect for capillaries that end where the gas pressure is not at a maximum.

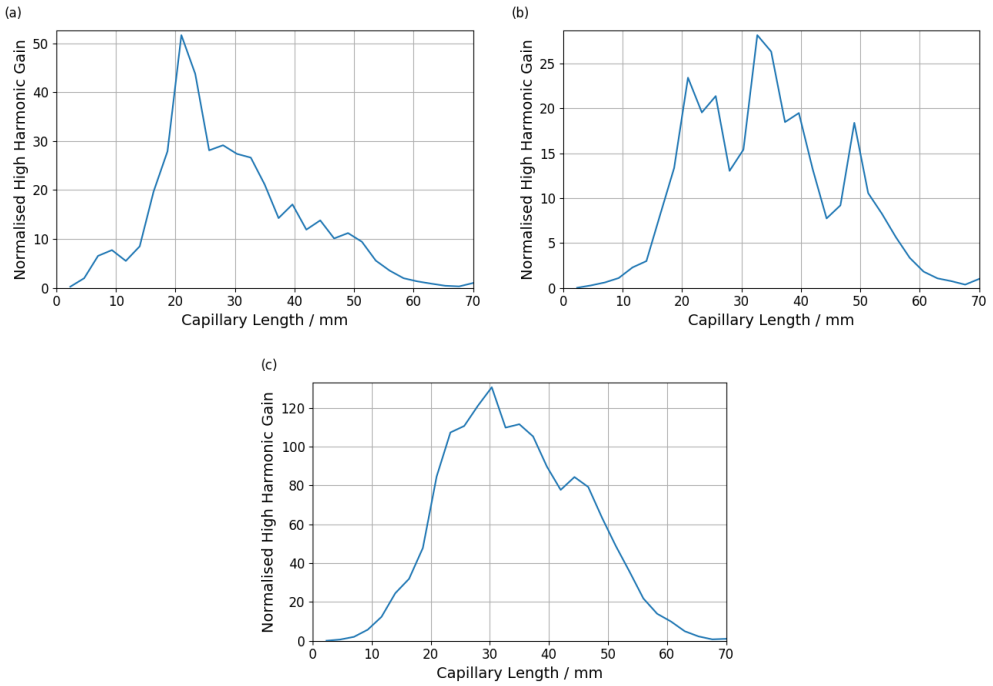

FIGURE 6.20: High harmonic increase for different length capillaries, integrated over the harmonic energy range 20 - 45 eV and normalised to the 7 cm length capillary, when using the (a) Yb-fibre 1, (b) 2, and (c) 3 laser systems

For the Yb-fibre 1 shown in Figure 6.20(a) there is a single large peak for a 2 cm length capillary that gives a harmonic increase of just over 50 times that of the 7 cm length capillary. After this peak the harmonics rapidly decrease for increasing capillary lengths. This laser experiences the least nonlinearities and distortions out of the three Yb-fibre systems as it propagates through the capillary and therefore provides better conditions for HHG by the end of the 7 cm length capillary. This conversely also results in lower values of harmonic increase normalised to the 7 cm length capillary due to the better HHG by the 7 cm length end. Additionally, from the laser pulse profiles given in Figure 6.7 we see that the laser pulse breaks up temporally soon after 2 cm into the capillary. This combined with the pulse spectral broadening and blueshift after this position reduces the conditions for HHG and therefore harmonics for capillary lengths greater than 2 cm, resulting in the large peak in harmonic increase for the 2 length capillary.

The normalised harmonic increase given here is from the energy integration range 20 - 45 eV. This means that the effects of the increases in harmonic intensities for the higher energy harmonics over 45 eV, as given in Figure 6.19(a) and other relevant figures, are not factored into the harmonic increase results as they are not included within the energy integration range.

For the Yb-fibre 2 laser system the normalised harmonic increase is given in Figure 6.20(b). Here there is a maximum increase about 27 times that of the 7 cm length capillary, just

over half that for the Yb-fibre 1 system, and also comparable to the Ti:Sapph laser system. Three peaks are present, with capillary lengths corresponding to peaks in the laser mode beating. The first is for a 2 cm length capillary, the second for a length between 3 - 3.5 cm, and the third for a length just under 5 cm. The length for the first peak also corresponds to that for the peak in the Yb-fibre 1 system though with the increase here being just under half it. Overall here, the first peak gives an increase of around 23 times, the second peak 27 times, and the third peak 17 times. Therefore, reducing the capillary length to a length corresponding to one of the peaks will increase the harmonic generation for harmonics within the 20 - 45 eV range.

For the harmonic increases of different length capillaries using the Yb-fibre 3 laser system, shown in Figure 6.20(c), we see one single peak in harmonic increase for a capillary length just over 3 cm. This gives a factor increase of around 130 times compared to the 7 cm capillary length. The laser profiles for this capillary have the largest amounts of laser pulse nonlinear distortion of all three Yb-fibre systems, resulting in largest amounts of temporal breakup and spectral broadening and blueshift. This results in a very wide range of generating driving wavelengths which causes a lot of the harmonics generated to be at a range of energies not corresponding to the initial driving wavelength which also causes them to have a lack of harmonic structure. Whilst reducing the capillary length to just over 3 cm would dramatically increase the high harmonic intensities within the 20 - 45 eV energy range, the harmonics would not be distinct or at predictable energies. Instead, other factors would be worth investigating, such as using a lower intensity driving pulse or a reduced capillary gas pressure to limit the nonlinear distortions experienced by the laser pulse and increase the clarity of the generated harmonics whilst hopefully maintaining the harmonic intensities and gains produced here.

6.4.3 Mid-IR OPCPA and Tm-Fibre Laser Systems

The high harmonic generation for different length capillaries using the Mid-IR and TM-fibre laser systems is given in Figure 6.21. Both systems produce clear harmonics for most of the capillary lengths, with just the Tm-fibre system losing some of the harmonic clarity for capillary lengths over 6 cm. Both systems also have significantly smaller harmonic intensities for all capillary lengths, compared to the results of the other laser systems. The harmonic intensities and maximum energies also follow the mode beating of the driving laser.

The Mid-IR laser system generates harmonics with a maximum energy of 70 eV for a capillary length of 1.5 cm whilst the Tm-fibre system produces harmonics with a maximum energy of 110 eV for a capillary length of around 2 - 2.5 cm. The harmonics from both systems are much more closely spaced together for all capillary lengths than

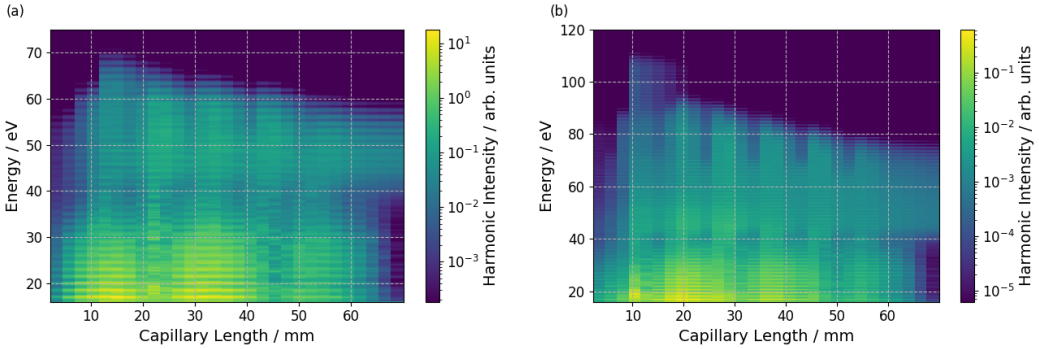

FIGURE 6.21: The high harmonic generation due to the (a) Mid-IR OPCPA and (b) Tm-fibre laser systems for different length capillaries.

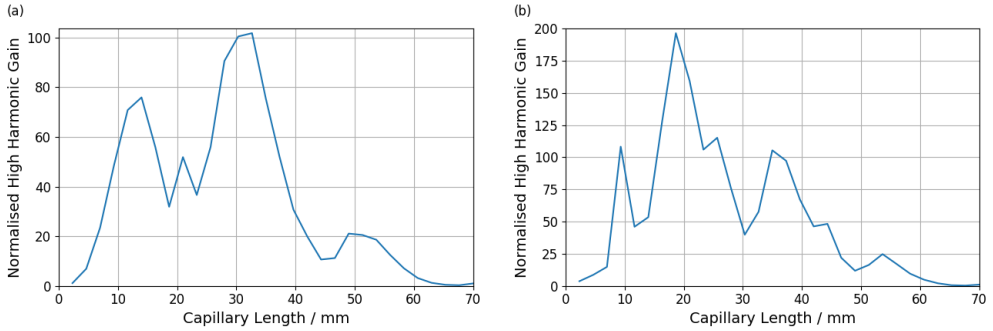

FIGURE 6.22: High harmonic increase for different length capillaries, integrated over the harmonic energy range 20 - 45 eV and normalised to the 7 cm length capillary, when using the (a) Mid-IR OPCPA and (b) Tm-fibre laser systems.

for those resulting from the previous laser systems. This is due to the driving wavelengths being much larger than for the previous systems, as well as the lasers for these Mid-IR and Tm-fibre systems not undergoing noticeable blueshift to shorter driving wavelengths. There are small amounts of nonlinear distortion to the Tm-fibre laser for capillaries over 6 cm in length. This is seen by the reduced clarity in harmonics between 40 - 60 eV for these capillary lengths. However, this effect is small.

The different length capillary HHG results for these two lasers are primarily affected by the laser mode beating. This could be used to optimised the HHG by choosing capillary lengths that coincides with peaks in laser intensity from this mode beating.

The normalised harmonic increase for different length capillaries when using the Mid-IR and TM-Fibre laser systems are given in Figure 6.22.

The normalised harmonic increase for different length capillaries when using the Mid-IR laser system, shown in Figure 6.22(a), has two large peaks in the increase achieved and also a third smaller peak, with these being for capillary lengths just under 1.5 cm, just over 3 cm, and at 5 cm. These give factors of increase in the harmonics of 70, 100, and 20 times respectively, relative to the 7 cm capillary. These again match the mode beating of the laser and whilst they give large increases the resulting harmonic

intensities are still much less than for the optimised capillary lengths of the other laser systems.

The normalised harmonic increase for different length capillaries when using the Tm-fibre system, as shown in Figure 6.22(b), has four peaks. These being for capillaries of lengths just under 1 cm and 2 cm, and at 3.5 and 5.5 cm length capillaries. These give harmonic increases of around 100, 190, 100, and 25 times respectively, compared to the 7 cm length capillary. The harmonic increases presented here could then be optimised by changing the capillary length to end at one of these peaks though the resulting harmonic generation over 20 - 45 eV energies would still be much less than that for the optimised capillary lengths of all the other laser systems.

6.5 Conclusions

The aim of this chapter was to essentially answer the question of which laser system is the best to use for capillary-based high harmonic generation. We found that whilst there is no clear answer to this question as it very much depends on the application and the targeted properties of the harmonics generated, there was a general trend for the three Yb-fibre systems to outperform the other three systems investigated. For this we demonstrated the potential of the advanced simulation model that we have developed by investigating the laser propagation and resulting harmonic generation when using capillaries of varying lengths with six different laser systems. We found that each laser system resulted in very different laser dynamics and harmonic generation. From this, if the clearest most distinct harmonics were the target then the lower initial peak laser intensity systems are better suited for this as their lasers stay the most unchanged and so produce the clearest harmonics. If instead the highest harmonic energies are the target then the Yb-fibre system performs the best out of the harmonic energy range we investigated, and for maximising the intensities of lower energy harmonics then the Yb-fibre 2 and 3 perform the best instead. A future line of investigation that would be of interest would be to test a Tm-fibre system with a comparable initial peak laser intensity and repetition rate to the Yb-fibre systems. This is since with the increased driving wavelength of 2000 nm compared to Yb-fibre systems of 1050 nm and with the comparable peak intensities, it would be interesting to see how the resulting HHG compared to the Yb-Fibre systems.

Within our work presented in this chapter we found that the capillary-based laser pulse dynamics and nonlinear distortions dramatically affect the HHG observed throughout that capillary. In general we saw that higher power lasers result in greater harmonic intensities though they also give rise to greater pulse distortions and reduced clarity in harmonics. Lower power lasers have negligible pulse distortions and give very clear harmonics though at the expense of harmonic intensities. The initial pulse width also

greatly affects the scale of these distortions as reducing it increases the laser pulse intensity and thus also the distortions it experiences. We found the mode beating of the driving laser and its radial variations to have a large effect on the harmonic generation, with significant contributions to the harmonic generation also coming from a wide range a wide range of radial positions. As such, we showed that to accurately simulate and predict the harmonic generation from a gas-filled hollow capillary, a laser pulse propagation and harmonic generation model that simulates along the full radius of the capillary is needed.

For the harmonic generation using different length capillaries, propagation of the harmonics became an important effect for those over 40 eV due to these harmonics not undergoing significant absorption by the gas and so experiencing build up that was not present for harmonics less than 40 eV. It was found generally that harmonics generated from capillary lengths less than the 7 cm had higher intensities. This was due to a combination of better laser conditions for HHG and gas pressure profiles that stopped abruptly rather than gradually ramping down. From this, we observed that different harmonic energies could be optimised for by carefully choosing capillary length. For example, using the Ti:Sapph laser system, the maximum harmonic energy could be optimised to give 65 eV for a capillary length between 5 - 6 cm, though to maximise the harmonic intensities below 40 eV then either a 3 or 4.5 cm length capillary should be chosen instead. Therefore, when designing a capillary-based HHG system, general harmonic generation optimisations can be made though if there is a harmonic energy to target then capillary length can be specifically optimised for this too.

Through determining the high harmonic increase normalised to a 7 cm length capillary for the integrated energy range 20 - 45 eV, we have shown that significant increases for all laser systems can be achieved by using shorter length capillaries. Through this we also showed that the gas pressure profile of the modelled 7 cm capillary is not an ideal choice and instead reducing the length over which the capillary pressure goes from a maximum to zero greatly increases the harmonics generated. Through the normalised harmonic increase results and those for the HHG using different length capillaries, if we know what the driving wavelength of the system will be at design time then generally the capillary length can be optimised to take advantage of the laser mode beating such that a peak in laser intensity occurs very close to the end of the capillary.

Chapter 7

Conclusions and Future Work

7.1 Conclusions

A complex computational model has been developed that simulates the propagation of a laser pulse through a gas-filled hollow capillary, the interactions of that laser with the gas atoms within that capillary, the resulting high harmonic generation, and the propagation of that high harmonic radiation to the end of the capillary. The laser propagation is performed through solving a unidirectional pulse propagation equation, the high harmonic generation through solving the time dependent Schrödinger equation, and the harmonic propagation through using a capillary-adapted angular spectrum method. The theoretical description of this model was first presented, followed by an overview of the computational implementation. The model is complex and a result in itself, providing the ability to simulate high harmonic generation within capillary geometries of multiple cm length scales, with these lengths being significant improvements on previous work. The full computational model can take a long time to run, using significant computing power to achieve appropriate resolutions for modelling capillary-based HHG. For example, a full capillary simulation takes approximately two days on the Southampton Iridis 5 HPC system. Despite this the developed model is extremely useful as parameters can be changed and tested within it much faster than they can be experimentally and parameters can be changed that are impractical to change experimentally without prior knowledge of potential improvements to the HHG resulting from them.

The computational model was validated against the literature through comparisons with both experimental and numerical results and showed good agreement despite the various approximations involved in our complex model. Features of the laser spectra matched well, with peaks occurring at the same wavelengths and the laser undergoing blueshift and broadening as it propagates through the capillary. For the harmonic energies under consideration within the work presented here, typically between $16 - 45$ eV,

good agreement were found between harmonic spectra produced from our 1D single atom harmonic generation model and ones gained from a 3D atom model. We therefore found that for the regimes under consideration our 1D model produced valid and useful spectra. The full capillary model was found to produce a close harmonic spectrum to one found in the literature when using comparable parameters, validating the ability of the model to produce harmonic spectra that would be expected experimentally.

The high harmonic generation scaling with driving wavelength was investigated for three different geometries. The first geometry, a single atom, was investigated to compare to results found within the literature whilst using a typically higher resolution. The second and third geometries, a thin sheet of atoms and a gas-filled hollow capillary, were investigated to expand our understanding of wavelength scaling to realistic experimental geometries as these had not been the focus before. The nature of our 1D single atom harmonic generation model presented differences to results from the literature due to the effects of quantum diffusion being reduced for our 1D model compared to 3D models and real life. When taking this into account we see comparable results to the literature. We show the often assumed pump-wavelength scaling law with harmonic intensity of a simple constant exponent, $I_h \propto \lambda^{-x}$, is an oversimplification as firstly there are quick rapid oscillations on the fine wavelength scale, secondly as sharp jumps in harmonic intensity occur as harmonics enter or leave the harmonic energy range under consideration, and thirdly as around the cutoff the dependence changes from a positive exponent to a zero and then to a negative one, with it then settling out to overall largely constant exponent value over the next a few hundred nm increases in driving wavelength. Prior to this, similar investigations in the literature predominantly focussed on the single atom geometry. Here however we explore two other geometries that are more complex and more representative of experimental situations where many atoms experiencing different parts of the pump laser contribute to the high harmonic generation: the sheet of atoms and the gas-filled hollow capillary. We found the sheet of atoms and capillary geometries to have comparable dependencies that were also larger than the single atom.

Six different laser systems were then investigated using our model. These lasers varied in their peak intensity, pulse width, repetition rate, and wavelength. This was done to investigate the capillary harmonic generation, laser evolution, and increases in harmonic generation for different capillary lengths when using each of these laser systems. We found that for the 7 cm length capillary the 1050 nm driving wavelength lasers generated the highest intensity harmonics. Out of these we also found that the smaller the pulse width laser the higher the harmonic intensities and energies generated. The clearest harmonics, however, were produced by the laser systems with the lowest laser pulse energies. This was due to the laser undergoing less distortion during its propagation for these and therefore having a central driving wavelength and temporal profile

that remains largely unchanged throughout the generation medium. Within the capillary the mode beating of the driving laser pulse corresponded to significant increases in the higher harmonic generation, with there being a radial dependence of the mode beating on the harmonic energies being generated. For different length capillaries it was also found that the 7 cm length capillary design was not optimal for HHG. Instead, shorter capillaries that had sudden quick decreases in gas pressure at their ends gave increased generation of harmonic intensities and energies. A comparison of the increase in harmonic generation going from a 7 cm to a 4.5 cm length capillary was made to a result found in the literature and there was found to be good agreement, showing the predictive capabilities of our model.

The aim of this work was to improve the understanding of capillary-based high harmonic generation and to help guide future laser system and capillary design so that target harmonic intensities and energies may be optimised for. The capillary-based HHG simulation model developed here is an advanced and complex a priori model that performs millions of calculations for each capillary simulation, giving access to unprecedented levels of detail of the laser-driven high harmonic generation throughout gas-filled hollow capillaries. This model can be used to enhance future experiments and table-top XUV source design through modelling and simulation so that optimisation may be found and exploited.

7.2 Future Work

Many directions can be taken for future work using the model developed here. Investigations undertaken within this work can be continued further and new lines of investigation performed too. The model developed can also be improved, in terms of speed, usability, and also accuracy of physical models used.

The model can also be used alongside an experiment, with the two running in parallel and guiding each other. Easy to change experimental parameters can be varied and studied to find observations of interest which can then be followed up using simulations to further investigate and understand them. Parameters that are difficult to change experimentally, such as laser wavelength or capillary length and gas pressure profile, can be studied first using simulations and then once optimisations have been found they can be exploited experimentally. Simulations can be used to better understand observations of interest and the physics driving them, as well as parameter spaces and hypotheses being explored through them to discover optimisations to HHG. In this way this model can be used to improve HHG.

In Chapter 6 it was consistently found that the Yb-laser systems outperformed the other systems. These Yb-fibre systems have much higher repetition rates than the other laser

systems, meaning they would create high HH fluxes for the same pulse energies. Additionally, they also have higher pulse energies that would result in higher cutoffs. This helps to explain the higher performance of these systems compared to the others and can be used to guide future laser system design. For instance, by using higher rep rates to achieve higher HH fluxes and larger laser pulse intensities to achieve higher cutoffs. These effects however do not explain the full difference in performance, which would likely also have a strong dependence on phase-matching, dispersion, and other laser dynamics. Further investigating why the Yb-fibre systems outperform the others, and the laser dynamics that are involved, would be very interesting as understanding why could help guide future improvements to high harmonic generation as well as to laser system design and choice when choosing between different laser systems for HHG experiments.

The computational model developed has a wide range of simulation parameters that can be changed within it that would likely drastically alter the resulting laser conditions and HHG. Exploring these therefore also has the potential to improve the HHG. For instance, throughout this work here the same core diameter of 150 μm has been used. Changing the core diameter and keeping the laser spot width at the optimum width to couple into the fundamental capillary mode would result in the atoms at the start of the capillary experiencing different peak laser intensities. For simple capillaries, reducing the core diameter increases the propagation losses of the laser. However, new hollow-core fibres and antiresonant fibres experience much lower laser propagation losses [117] and so investigating the resulting HHG for these fibres, with reduced core diameters, would be beneficial too. Alongside this, it would also change the number of atoms present within the capillary too due to the changed diameter but constant gas pressure. The result would be that larger diameter capillaries would experience smaller initial peak laser intensities whilst containing more HH-generating atoms and smaller diameter capillaries would experience larger initial peak laser intensities but less atoms. Each scenario would result in different laser pulse propagation along the capillary and due to this and the differences in the number of atoms, these could result in very different HHG.

Another route of investigation using the model developed here could be to investigate different driving wavelengths, with the aim being to gain further understanding of the capillary-based laser propagation and resulting HHG. In Chapter 5 the integrated harmonic energy at the end of the capillary for different wavelengths was investigated to study how the high harmonic generation depends on the driving wavelength. This could be expanded by investigating specific harmonics to understand how each one depends on the driving wavelength, and by investigating how the harmonic dependence depends on the driving wavelength throughout the capillary rather than just at the end, both for an integrated harmonic energy range and for individual harmonics. Additional driving wavelengths can also be investigated too, both at shorter and

longer wavelengths than used in Chapter 5 and also at additional wavelengths to increase the resolution and accuracy of the dependence determination. Within Chapter 6 six different laser systems were investigated, with there being only four different driving wavelengths between them. Using the model developed here, other specific laser systems and driving wavelengths could also be investigated to expand this and see how their laser profiles and resulting HHG compare to the six laser systems here, using the same analysis as performed in Chapter 6. This would give insight into how other real-world laser systems perform in regards to HHG, how different laser systems and driving wavelengths affect capillary-based HHG optimisations, and can be used to help guide laser system design for future HHG experiments.

Also shown in Chapter 6 was that the length of the capillary and the gas pressure profile significantly affect the HHG. Improvements to the harmonic generation could then be found by further investigating these areas. Following the methodology of Chapter 6, systematic studies into capillary length for given laser systems could be performed to pinpoint capillary lengths that result in increased HHG. Alongside this, the model that has been developed here could be improved by changes to enable it to model different gas pressure profiles for capillaries of arbitrary lengths and gas inlet positions. This could then be used on its own to perform systematic studies of HHG changes and improvements for different gas pressure profiles and inlet positions, and also with the other studies of different length capillaries such that approximate capillary lengths and gas pressure profiles corresponding to HHG improvements can be quickly found so that more realistic gas pressure profiles can then be used to further study and refine the results and understanding.

This model could also be used to investigate different geometries too. Whilst the model has been developed for capillary geometries, and as such utilises assumptions that are specifically true for the capillary geometry, others could be modelled using it too. For instance, the model could be used to also simulate gas jets by assuming that a gas jet can be approximated by a very short capillary that is much wider than the driving laser pulse, as this would then be a realistic gas jet interaction length and also negate interactions of laser pulse and capillary wall. This would then allow for direct comparisons between the two geometries. Other geometries could be modelled too using this, such as hollow-core fibres capillaries that have different capillary wall losses to the capillary already modelled here. The HHG from all these could then be compared amongst each other to better understand how different geometries affect it.

The model developed could be improved in a number of ways. One such way would be its computational speed. There are many potential ways to do this though two of these could be to move away from dynamic arrays and resizing of arrays within the computer code, and also profiling the code to determine which functions take the longest to run and which are called the most, so that if there are functions that take a relatively long time to run and are called frequently they can then be found and potentially

specifically optimised. The accuracy of the model could also be improved too. So far the atom model is the 1D single active electron model. This could be changed to include multiple active electrons or instead to move to a 3D model [83], for example. The 1D soft Coulomb model is also used though other 1D potentials exist too [106]. Others could therefore be supported within the code so that a user could be able to select their desired one. Additionally, a way for incorporating an arbitrary atomic potential could also be included. These other atom potentials would then allow for potentially more accurate and complex atom models than the current 1D model. Work could also be done to make the computer model more user friendly too. For instance, an easier way to set up and run the individual parts of a full capillary simulation, or the outputting data and results to a standard output such as HDF5.

Another interesting extension to the model developed here would be to link the HHG to the driving laser pulse such that the HHG drives the nonlinear polarisation of the propagating laser pulse, giving unprecedented insight into the plasma dynamics and strong physics effects. Whilst this would need some alterations to the code to both allow it and to improve the computational speed due to this likely being computationally expensive, the unprecedented modelling of HHG-driven plasma dynamics and strong field effects would be of great interest.

References

[1] Artemis laser at the central facility, u.k. (website). https://www.clf.stfc.ac.uk/Pages/Artemis.aspx.

[2] CXRO. http://henke.lbl.gov/optical_constants/. Accessed: 2019-06-16.

[3] Diamond - frequenctly asked questions (website). https://www.diamond.ac.uk/Home/About/FAQs/General.html, . Accessed: 2019-06-11.

[4] Diamond - opening (website). https://www.diamond.ac.uk/Home/News/LatestNews/October2007.html, . Accessed: 2019-06-11.

[5] Doxygen. https://www.doxygen.nl/index.html.

[6] The nobel prize in physics 2018 (website). https://www.nobelprize.org/prizes/physics/2018/press-release/. Accessed: 2019-06-11.

[7] European xfel - facts and figures (website). https://www.xfel.eu/facility/overview/facts_amp_figures/index_eng.html, . Accessed: 2019-06-11.

[8] European xfel - inauguration (website). https://www.xfel.eu/news_and_events/news/index_eng.html?openDirectAnchor=1323&two_columns=0, . Accessed: 2019-06-11.

[9] E. Abbe. Beiträge zur theorie des mikroskops und der mikroskopischen wahrnehmung. *Archiv für mikroskopische Anatomie*, 9, 1873.

[10] B. Agarwal. *X-Ray Spectroscopy: An Introduction*. Springer-Verlag Berlin Heidelberg, 1991.

[11] Hiroshi Akima. A new method of interpolation and smooth curve fitting based on local procedures. *J. ACM*, 17(4):589–602, 1970.

[12] P. N. Anderson. XNLO. https://github.com/patrickanderson1/XNLO, 2015. Accessed: 2016.

[13] P. N. Anderson. *High-order harmonic generation with self-compressed femtosecond pulses*. Ph.D. thesis, University of Southampton, Optoelectronic Research Centre, 2015.

[14] P. N. Anderson, P. Horak, J. G. Frey, and W. S. Brocklesby. High-energy laser-pulse self-compression in short gas-filled fibres. *Phys. Rev. A*, 89:013819, 2014.

[15] D. Attwood. *Soft X-Rays and Extreme Ultraviolet Radiation: Principles and Applications*. Cambridge University Press, 1999.

[16] P. Bader, S. Blanes, and F. Casas. Solving the Schrödinger eigenvalue problem by the imaginary time propagation techniques using splitting methods with complex coefficients. *J. Chem. Phys.*, 139, 2013.

[17] R. A. Bartels, A. Paul, H. Green, H. C. Kapteyn, M. M. Murnane, S. Backus, I. P. Christov, Y. Liu, D. Attwood, and C. Jacobsen. Generation of spatially coherent light at extreme ultraviolet wavelengths. *Science*, 297:376–378, 2002.

[18] M. Bass, P. A. Franken, A. E. Hill, C. W. Peters, and G. Weinreich. Optical mixing. *Phys. Rev. Lett.*, 8, 1962.

[19] A. Bideau-Mehu, Y. Guern, R. Abjean, and A. Johannin-Gilles. Measurement of refractive indices of neon, argon, krypton and xenon in the 253.7–140.4 nm wavelength range. dispersion relations and estimated oscillator strengths of the resonance lines. *J. Quant. Spectrosc. Rad. Transfer*, 25:395–402, 1981.

[20] N. Bloembergen and P. S. Pershan. Light waves at the boundary of nonlinear media. *Phys. Rev.*, 128, 1962.

[21] M. Born and E. Wolf. *Principles of Optics*. Pergamon Press Ltd., Oxford, 3rd edition, 1965.

[22] R. W. Boyd. *Nonlinear Optics*. Elsevier Science, 3rd edition, 2008.

[23] D. C. Burnham and D. L. Weinberg. Observations of simultaneity in parametric production of optical photon pairs. *Phys. Rev. Lett.*, 25, 1970.

[24] T. J. Butcher, P. N. Anderson, R. T. Chapman, P. Horak, J. G. Frey, and W. S. Brocklesby. Bright extreme-ultraviolet high-order-harmonic radiation from optimized pulse compression in short hollow waveguides. *Phys. Rev. A*, 87:043822, 2013.

[25] R. T. Chapman, T. J. Butcher, P. Horak, F. Poletti, J. G. Frey, and W. S. Brocklesby. Modal effects on pump-pulse propagation in an Ar-filled capillary. *Opt. Express*, 18:13279, 2010.

[26] E. Constant, D. Garzella, P. Breger, E. Mével, C. Dorrer, C. Le Blanc, and F. Salin. Optimizing high harmonic generation in absorbing gases: model and experiment. *Phys. Rev. Lett.*, 83(8):1668–1671, 1999.

[27] P. B. Corkum. Plasma perspective on strong field multiphoton ionization. *Phys. Rev. Lett.*, 71:1994–1997, 1993.

[28] A. Couairon, E. Brambilla, T. Corti, D. Majus, O. J. Ramirez-Góngora, and M. Kolesik. Practitioners guide to laser pulse propagation models and simulation. *Eur. Phys. J. Special Topics*, 199, 2011.

[29] C. Courtois, A. Couairon, B. Cros, J. R. Marques, and G. Matthieussent. Propagation of intense ultrashort laser pulses in a plasma filled capillary tube: Simulations and experiments. *Physics of Plasmas*, 8(7):3445–3456, 2001.

[30] E. Cumberbatch. Self-focusing in non-linear optics. *J. Inst. Maths Applics.*, 6, 1970.

[31] Leonardo Dagum and Ramesh Menon. Openmp: An industry-standard api for shared-memory programming. *IEEE Comput. Sci. Eng.*, 5(1):46–55, 1998. ISSN 1070-9924.

[32] F. de Groot. Multiplet effects in x-ray spectroscopy. *Coordination Chemistry Reviews*, 249:31–63, 2005.

[33] P. L. DeVries and J. Hasbun. *A first course in computational physics*. Jones and Barlett, Sudbury, second edition, 2011.

[34] J. H. Ebery, Q. Su, and J. Javanainen. High-order harmonic production in multiphoton ionization. *J. Opt. Soc. Am. B*, 6:1289–1298, 1989.

[35] J. H. Ebery, Q. Su, and J. Javanainen. Nonlinear light scattering accompanying multiphoton ionization. *Phys. Rev. Lett.*, 62:881–884, 1989.

[36] J. H. Ebery, Q. Su, J. Javanainen, K. C. Kulander, B. W. Shore, and L. Roso-Franco. High-order harmonic generation during multiphoton ionization of gases. *J. Mod. Opt.*, 36:829–855, 1989.

[37] E. L. Falcão-Filho, V. M. Gkortsas, A. Gordon, and F. X. Kärtner. Analytic scaling analysis of high harmonic generation conversion efficiency. *Opt. Express*, 17: 11217–11229, 2009.

[38] E. Fehlberg. Low-order classical runge-kutta formulas with stepsize control and their application to some heat transfer problems. 1969.

[39] M. Ferray, A. L'Huillier, X. F. Li, L. A. Lompre, G. Mainfray, and C. Manus. Multiple-harmonic conversion of 1064 nm radiation in rare gases. *J. Phys. B: At. Mol. Opt. Phys.*, 21, 1988.

[40] P. A. Franken, A. E. Hill, C. W. Peters, and G. Weinreich. Generation of optical harmonics. *Phys. Rev. Lett.*, 7, 1961.

[41] M. V. Frolov, N. L. Manakov, and A. F. Starace. Wavelength scaling of high-harmonic yield: Threshold phenomena and bound state symmetry dependence. *Phys. Rev. Lett.*, 100:173001, 2008.

[42] M. V. Frolov, N. L. Manakov, W. Xiong, L. Peng, J. Burgdörfer, and A. F. Starace. Scaling laws for high-order-harmonic generation with midinfrared laser pulses. *Phys. Rev. A*, 92:023409, 2015.

[43] C. A. Froud, E. T. F. Rogers, D. C. Hanna, W. S. Brocklesby, M. Praeger, A. M. de Paula, and J. J. Baumberg. Soft-x-ray wavelength shift induced by ionization effects in a capillary. *Opt. Lett.*, 31:374–376, 2006.

[44] C. A. Froud, R. T. Chapman, E. T. F. Rogers, M. Praeger, B. Mills, J. Grant-Jacob, T. J. Butcher, S. L. Stebbings, A. M. de Paula, J. G. Frey, and W. S. Brocklesby. Spatially resolved Ar^* and Ar^{+^*} imaging as a diagnostic for capillary-based high harmonic generation. *J. Opt. A: Pure Appl. Opt.*, 11:054011, 2009.

[45] M. B. Gaarde and K. J. Schafer. Quantum path distributions for high-order harmonics in rare gas atoms. *Phys. Rev. A*, 65:031406, 2002.

[46] M. B. Gaarde and K. J. Schafer. Theory of attosecond pulse generation. *Springer Series in Optical Sciences*, 177:11–31, 2003.

[47] M. B. Gaarde and K. J. Schafer. Macroscopic aspects of attosecond pulse generation. *J. Phys. B: At. Mol. Opt. Phys.*, 41:132001, 2008.

[48] Edgar Gabriel, Graham E. Fagg, George Bosilca, Thara Angskun, Jack J. Dongarra, Jeffrey M. Squyres, Vishal Sahay, Prabhanjan Kambadur, Brian Barrett, Andrew Lumsdaine, Ralph H. Castain, David J. Daniel, Richard L. Graham, and Timothy S. Woodall. Open MPI: Goals, concept, and design of a next generation MPI implementation. In *Proceedings, 11th European PVM/MPI Users' Group Meeting*, pages 97–104, Budapest, Hungary, 2004.

[49] E. A. Gibson, A. Paul, N. Wagner, R. Tobey, S. Backus, I. P. Christov, M. M. Murnane, and H. C. Kapteyn. High-order harmonic generation up to 250 eV from highly ionized argon. *Phys. Rev. Lett.*, 92:033001, 2004.

[50] J. A. Giordmaine. Mixing of light beams in crystals. *Phys. Rev. Lett.*, 8, 1962.

[51] Gaël Guennebaud, Benoît Jacob, et al. Eigen v3. http://eigen.tuxfamily.org, 2010.

[52] S. Guha and J. Falk. The effects of focusing in the three-frequency parametric upconverter. *J. Appl. Phys.*, 51, 1980.

[53] M. Guizar-Sicairos and J. C. Gutiérrez-Vega. Computation of quasi-discrete Hankel transforms of integer order for propagating optical wave fields. *J. Opt. Soc. Am. A*, 21:53–58, 2004.

[54] L. Hareli, L. Lobachinsky, G. Shoulga, Y. Eliezer, L. Michaeli, and A. Bahabad. On-the-fly control of high-harmonic generation using a structured pump beam. *Phys. Rev. Lett.*, 120, 2018.

[55] B. L. Henke, E. M. Gullikson, and J. C. Davis. X-ray interactions: photoabsorption, scattering, transmission, and reflection at E=50-30000 eV, Z=1-92. *Atomic Data and Nuclear Data Tables*, 54:181–342, 1993.

[56] J. Higuet, H. Ruf, N. Thiré, R. Cireasa, E. Constant, E. Cormier, D. Descamps, E. Mével, S. Petit, B. Pons, Y. Mairesse, and B. Fabre. High-order harmonic spectroscopy of the cooper minimum in argon: Experimental and theoretical study. *Phys. Rev. A*, 83:053401, 2011.

[57] C. G. Durfee III, A. R. Rundquit, S. Backus, and C. Herne. Phase matching of high-order harmonics in hollow waveguides. *Phys. Rev. Lett.*, 83(11):2187–2190, 1999.

[58] Intel. Math Kernel Library. `https://software.intel.com/oneapi/onemkl`, 2010.

[59] K. L. Ishikawa, K. Schiessl, E. Persson, and J. Burgdörfer. Fine-scale oscillations in the wavelength and intensity dependence of high-order harmonic generation: Connection with channel closings. *Phys. Rev. A*, 79:033411, 2009.

[60] C. Jin, A. Le, and C. D. Lin. Medium propagation effects in high-order harmonic generation of Ar and N_2. *Phys. Rev. A*, 83:023411, 2011.

[61] C. Jin, K. Hong, and C. D. Lin. Macroscopic scaling of high-order harmonics generated by two-color optimized waveforms in a hollow waveguide. *Phys. Rev. A*, 96:013422, 2017.

[62] A. S. Johnson, T. Avni, E. W. Larsen, D. R. Austin, and J. P. Marangos. Attosecond soft x-ray high harmonic generation. *Phil. Trans. R. Soc. A*, 377:20170468, 2019.

[63] L. V. Keldysh. Ionization in the field of a strong electromagnetic wave. *Soviet Physics JETP*, 20(5), 1965.

[64] D. N. Klyshko, A. N. Penin, and B. F. Polkovnikov. Parametric luminesence and light scattering by polaritons. *JETP Lett*, 11, 1970.

[65] M. Kolsik and J. V. Moloney. Nonlinear optical pulse propagation simulation: From Maxwell's to unidirectional equations. *Phys. Rev. E*, 70, 2004.

[66] J. L. Krause, K. J. Schafer, and K. C. Kulander. High-order harmonic generation from atoms and ions in the high intensity regime. *Phys. Rev. Lett.*, 68(24), 1992.

[67] M. Lewenstein, Ph. Balcou, M. Yu. Ivanov, A. L'Huillier, and P. B. Corkum. Theory of high-harmonic generation by low frequency laser fields. *Phys. Rev. A*, 49 (3):2117–2132, 1994.

[68] A. L'Huillier and Ph. Balcou. High-order harmonic generation in rare gases with a 1-ps 1053-nm laser. *Phys. Rev. Lett.*, 70(6), 1993.

[69] A. L'Hullier and P. Balcou. Calculations of high-order harmonic-generation in xenon at 1064 nm. *Phys. Rev. A*, 46(5), 1992.

[70] Gebhardt M, Heuermann T, Klas R, Liu C, Kirsche A, Lenski M, Wang Z, Gaida C, Antonio-Lopez J E, Schülzgen A, Amezcua-Correa R, Rothhardt J, and Limpert J. Bright, high-repetition-rate water window soft x-ray source enabled by nonlinear pulse self-compression in an antiresonant hollow-core fibre. *Light Sci. Appl.*, 10 (36), 2021.

[71] T. H. Maiman. Stimulated optical radiation in ruby. *Nature*, 187, 1960.

[72] P. D. Maker, R. W. Terhune, M. Nisenoff, and C. M. Savage. Effects of dispersion and focusing on the production of optical harmonics. *Phys. Rev. Lett.*, 8, 1962.

[73] E. A. J. Marcatili and R. A. Schmeltzer. Hollow metallic and dielectric waveguides for long distance optical transmission and lasers. *The Bell System Technical Journal*, 43(4):1783–1809, 1964.

[74] A. McPherson, G. Gibson, H. Jra, U. Johann, T. S. Luk, L. A. McIntyre, K. Boyer, and C. K. Rhodes. Studies of multiphoton production of vacuum-ultraviolet radiation in the rare gases. *J. Opt. Soc. Am B*, 4:595–601, 1987.

[75] J. Miao, P. Charalambous, J. Kirz, and D. Sayre. Extending the methodology of x-ray crystallography to allow imaging of micrometre-sized non-crystalline specimens. *Nature*, 400(6742):342–344, 1999.

[76] J. Miao, P. Charalambous, J. Kirz, and D. Sayre. Extending the methodology of x-ray crystallography to allow imaging of micrometre-sized non-crystalline specimens. *Nature*, 40, 1999.

[77] J. Miao, R. L. Sandberg, and C. Song. Coherent x-ray diffraction imaging. *IEEE Journal of Selected Topics in Quantum Electronics*, 18, 2012.

[78] J. Miao, T. Ishikawa, I. Robinson, and M. M. Murnane. Beyond crystallography: Diffractive imagine using coherent x-ray light sources. *Science*, 348, 2015.

[79] Microsoft. Windows Subsystem for Linux. `https://docs.microsoft.com/en-us/windows/wsl/`.

[80] Michael Müller, Marco Kienel, Arno Klenke, Thomas Gottschall, Evgeny Shestaev, Marco Plötner, Jens Limpert, and Andreas Tünnermann. 1 kw 1 mj eight-channel ultrafast fiber laser. *Opt. Lett.*, 41(15):3439–3442, 2016.

[81] R. K. Nubling and J. A. Harrington. Launch conditions and mode coupling in hollow-glass waveguides. *Optical Engineering*, 37(9):2454–2458, 1998.

[82] D. Papp and A. Andreev. A proposed 100khz repetition rate femtosecond laser plasma hard x-ray source at the eli-alps facility. In *2015 IEEE International Conference on Plasma Sciences (ICOPS)*, pages 1–1, 2015.

[83] Serguei Patchkovskii and H.G. Muller. Simple, accurate, and efficient implementation of 1-electron atomic time-dependent schrödinger equation in spherical coordinates. *Computer Physics Communications*, 199:153–169, 2016.

[84] W. Paulif. *Wave Mechanics*. Dover Publications Inc., 2003.

[85] V. S. Popov. Tunnel and multiphoton ionization of atoms and ions in a strong laser field(Keldysh theory). *Physics-Uspekhi*, 47(9):855–885, 2004.

[86] M. Praeger, A. M. De Paula, C. A. Froud, E. T. F. Rogers, S. L. Stebbings, W. S. Brocklesby, J. J. Baumberg, D. C. Hanna, and J. G. Frey. Spatially resolved soft x-ray spectrometry from single-imagine diffraction. *Nature Physics*, 3, 2007.

[87] R. C. Prince, R. R. Frontiera, and E. O. Potma. Stimulated raman scattering: From bult to nano. *Chem. Rev.*, 117, 2017.

[88] S. C. Rae, X. Chen, and K. Burnett. Saturation of harmonic generation in one- and three-dimensional atoms. *Phys. Rev. A*, 50:1946–1949, 1994.

[89] V. C. Reed and K. Burnett. Ionization of atoms in intense laser pulses using the Kramers-Henneberger transformation. *Phys. Rev. A*, 42:3152–3155, 1990.

[90] V. C. Reed and K. Burnett. Role of resonances and quantum-mechanical interference in the generation of above-threshold-ionization spectra. *Phys. Rev. A*, 43: 6217–6226, 1991.

[91] V. C. Reed and K. Burnett. Loss of harmonic generation in intense laser fields. *Phys. Rev. A*, 46:424–429, 1992.

[92] E. T. F. Rogers. *Modelling of capillary high harmonic generation*. Ph.D. thesis, University of Southampton, Optoelectronic Research Centre, 2008.

[93] E. T. F. Rogers, S. L. Stebbings, A. M. de Paula, C. A. Froud, M. Praeger, B. Mills, J. Grant-Jacob, W. S. Brocklesby, and J. G. Frey. Spatiotemporal phase-matching in capillary high-harmonic generation. *J. Opt. Soc. Am. B*, 29, 2012.

[94] A. Rundquist, C. G. Durfee III, Z. Chang, C. Herne, S. Backus, M. M. Murnane, and H. C. Kapteyn. Phase-matched generation of coherent soft x-rays. *Science*, 280:1412–1415, 1998.

[95] R. L. Sandberg, A. Paul, D. A. Raymondson, Hädrich S., D. M. Gaudiosi, J. Holtsnider, R. I. Tobey, O. Cohen, M. M. Murnane, H. C. Kapteyn, C. Song, J. Miao, Y. Liu, and F. Salmassi. Lensless diffractive imaging using tabletop coherent high-harmonic soft-x-ray beams. *Phys. Rev. Lett.*, 99:098103, 2007.

[96] A. Sanpera and L. Roso-Franco. Short-time multiphoton detachment in a one-dimensional model with very-short-range potential. *Phys. Rev. A*, 41:6515–6518, 1990.

[97] A. Sanpera and L. Roso-Franco. Resonant and nonresonant effects in the multiphoton detachment of a one-dimensional model ion with a short-range potential. *J. Opt. Soc. Am. B*, 8:1568–1575, 1991.

[98] A. Sanpera, Q. Su, and L. Roso-Franco. Ionization suppression in a very-short-range potential. *Phys. Rev. A*, 47:2312–2318, 1993.

[99] K. J. Schafer, B. Yang, L. F. DiMauro, and K. C. Kulander. Above threshold ionization beyond the high harmonic cutoff. *Phys. Rev. Lett.*, 70, 1993.

[100] K. Schiessl, K. L. Ishikawa, E. Persson, and J. Burgdörfer. Quantum path interference in the wavelength dependence of high-harmonic generation. *Phys. Rev. Lett.*, 99:253903, 2007.

[101] K. Schiessl, K. L. Ishikawa, E. Persson, and J. Burgdörfer. Wavelength dependence of high-harmonic generation from ultrashort pulses. *J. Mod. Opt.*, 55:2617–2630, 2008.

[102] M. Schnurer, Z. Cheng, M. Hentschel, G. Tempea, P. Kalman, T. Brabec, and F. Krausz. Absorption-limited generation of coherent ultrashort soft-x-ray pulses. *Phys. Rev. Lett.*, 83(4), 1999.

[103] S. M. Senior. UXH. `https://github.com/samuelsenior/UXH`, 2021.

[104] A. D. Shiner, C. Trallero-Herrero, N. Kajumba, H. C. Bandulet, D. Comtois, F. Légaré, M. Giguère, J. C. Kieffer, P. B. Corkum, and D. M. Villeneuve. Wavelength scaling of high harmonic generation efficiency. *Phys. Rev. Lett.*, 103:073902, 2009.

[105] A. E. Siegman. *Lasers*. University Science Books, 1986.

[106] A. A. Silaev, M. Y. Ryabikin, and N. V. Vvedenskii. Strong-field phenomena caused by ultrashort laser pulses: Effective one- and two-dimensional quantum-mechanical descriptions. *Phys. Rev. A*, 82:033416, 2010.

[107] S. L. Stebbings, E. T. F. Rogers, A. M. de Paula, M. Praeger, C. A. Froud, B. Mills, D. C. Hanna, J. J. Baumberg, W. S. Brocklesby, and J. G Frey. Molecular variation of capillary-produced soft x-ray high harmonics. *J. Phys. B: At. Mol. Opt. Phys.*, 41, 2008.

[108] S. L. Stebbings, J. G. Frey, and W. S. Brocklesbury. An attosecond soft x-ray nanoprobe: New technology for molecular imaging,. In M. Grishin, editor, *Advances in Solid State Lasers*. InTech, 2010.

[109] G. J. Stein, P. D. Keathley, P. Krogen, H. Liang, J. P. Siqueira, C. Chang, C. Lai, K. Hong, G. M. Laurent, and F. X. Kärtner. Water-window soft x-ray high-harmonic generation up to the nitrogen K-edge driven by a kHz, 2.1 μm OPCPA source. *J. Phys. B: At. Mol. Opt. Phys.*, 49, 2016.

[110] D. Strickland and G. Mourou. Compression of amplified chirped optical pulses. *Opt. Commun.*, 56, 1985.

[111] J. Tate, T. Auguste, H. G. Muller, P. Salières, P. Agostini, and L. F. DiMauro. Scaling of wave-packet dynamics in an intense midinfrared field. *Phys. Rev. Lett.*, 98: 013901, 2007.

[112] V. Tosa, H. T. Kim, I. J. Kim, and C. H. Nam. High-order harmonic generation by chirped and self-guides femptosecond laser pulses. I. Spatial and spectral analysis. *Phys. Rev. A*, 71:063807, 2005.

[113] G. van de Sand and J. M. Rost. Irregular orbits generate higher harmonics. *Phys. Rev. Lett.*, 83:524–527, 1999.

[114] I. Velchev, W. Hogervorst, and W. Ubachs. Precision VUV spectroscopy of ArI at 105 nm. *J. Phys. B: At. Mol. Opt. Phys.*, 32, 1999.

[115] N. L. Wagner, E. A. Gibson, T. Popmintchev, I. P. Christov, M. M. Murmane, and H. C. Kapteyn. Self-compression of ultrashort pulses through ionization-induced spatiotemporal reshaping. *Phys. Rev. Lett.*, 93:173902, 2004.

[116] P. Wessels, B. Ruff, T. Kroker, A. K. Kazansky, N. M. Kabachnik, K. Senstock, M. Drescher, and J. Simonet. Absolute strong-field ionization probabilities of ultracold rubidium atoms. *Communications Physics*, 1, 2018.

[117] N. V. Wheeler, T. D. Bradley, J. R. Hayes, M. A. Gouveia, S. Liang, Y. Chen, S. R. Sandoghchi, S. M. Abokhamis Mousavi, F. Poletti, M. N. Petrovich, and D. J. Richardson. Low-loss kagome hollow-core fibers operating from the near- to the mid-ir. *Opt. Lett.*, 42:2571–2574, 2017.

[118] Hans Jakob Wörner, Hiromichi Niikura, Julien B. Bertrand, P. B. Corkum, and D. M. Villeneuve. Observation of electronic structure minima in high-harmonic generation. *Phys. Rev. Lett.*, 102:103901, 2009.

[119] M. Zepf, B. Dromey, M. Landreman, P. Foster, and S. M. Hooker. Bright quasi-phase-matched soft-x-ray harmonic radiation from argon ions. *Phys. Rev. Lett.*, 99, 2007.